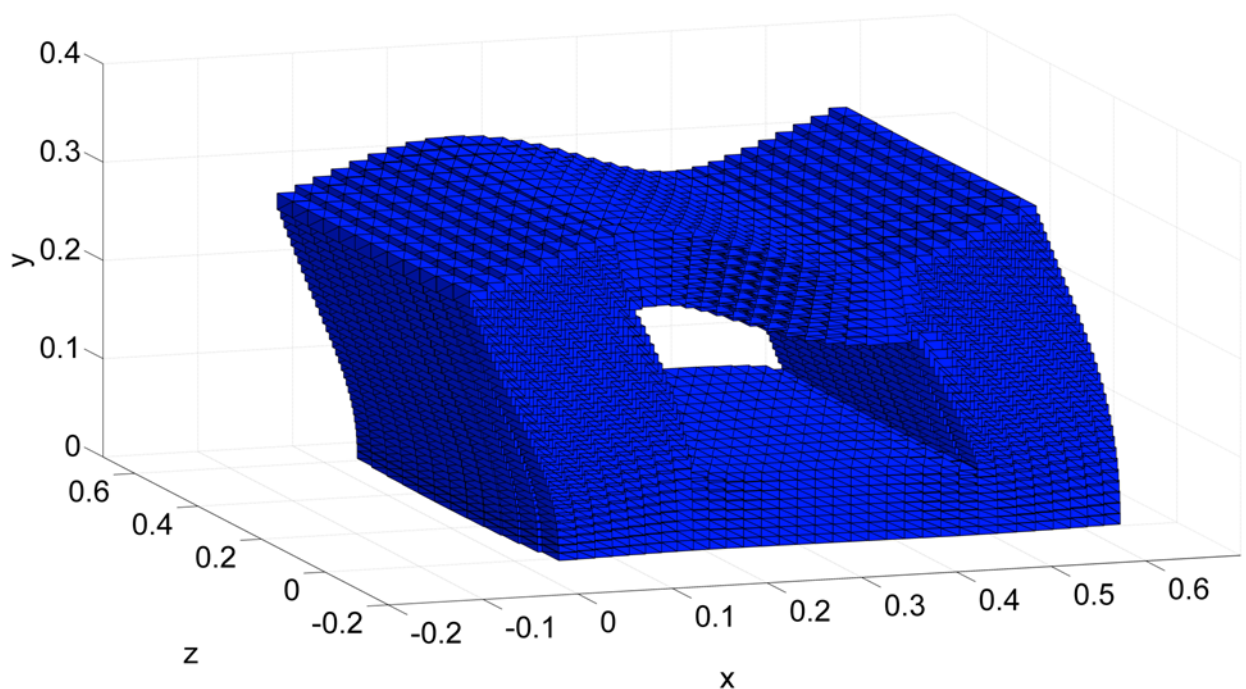


Controller-structure optimization using parameter-dependent modal reduced state-space models

C. van der Marel

Master of Science Thesis



Controller-structure optimization using parameter-dependent modal reduced state-space models

MASTER OF SCIENCE THESIS

For the degree of Master of Science in Control Engineering at Delft
University of Technology

C. van der Marel

December 8, 2014

Faculty of Mechanical, Maritime and Materials Engineering (3mE) · Delft University of
Technology

Abstract

Although it is still common in the field of motion control systems to first design the structure and then the controller, integrated design approaches are becoming more popular. The problem of finding optimal parameters for a parameterized structure and controller by solving an optimization problem will be referred to as *controller-structure optimization* (CSO). These types of problems are often characterized as multi-objective and non-convex and therefore hard to solve. Especially if the parameterized structure is modelled in a finite-element (FE) environment.

This MSc thesis report presents a design approach for solving a CSO problem by using an approximate model of the parameterized structure in the form of a *parameter-dependent state-space* (PDSS) model. The PDSS model is obtained by taking a few samples of the original structure. Each of these samples represents a *linear time-invariant* (LTI) modal reduced state-space model. The main emphasis of this MSc thesis is to investigate whether this approach is able to approximate the solution of the original (comprehensive) CSO problem in an efficient way.

Table of Contents

Preface	v
Acknowledgments	vii
1 Introduction	1
1-1 Motivation	1
1-2 Problem Statement	2
1-3 Structure of MSc thesis	3
2 Design approach	5
2-1 Parameterizing the structure	5
2-2 Parameterizing the controller	6
2-3 Generating a set of local models in modal form	6
2-4 Deriving a PDSS model	7
2-5 Formulating and solving a CSO problem	8
2-6 Showcase example: double mass-spring-damper system	9
3 Local models in modal state-space form	13
3-1 Choosing a coherent state-space representation	13
3-2 Modal state-space form	14
3-3 Ordering modeshapes	16
3-4 Showcase example: double mass-spring-damper system	18
4 Parameter-dependent state-space (PDSS) modelling	23
4-1 PDSS model structure	23
4-2 Fixing elements in state-space matrices	24
4-3 Linear Least Squares Approach	25
4-4 Validation of PDSS model	26
4-5 Showcase example: double mass-spring-damper system	29

5	Controller-structure optimization (CSO)	35
5-1	Optimization criteria	35
5-2	Integrated optimization	37
5-3	Nested optimization	38
5-4	Showcase example: double mass-spring-damper system	40
6	CSO for a single-axis motion system	45
6-1	Introduction	45
6-2	Restrictions of parameterized structure	47
6-3	Dynamic behaviour of the parameterized structure	48
6-4	Constructing a PDSS model	53
6-5	Results of CSO problem	54
6-6	Effect of different measurement position	58
6-7	Mode switching	62
7	Conclusions and recommendations	65
A	Modelling a block with a hole in 2D with the finite element methods	69
B	Deriving element matrices for a bilinear rectangle Q4	75
C	Check properties of stiffness and mass matrices	81
D	Free vibration problem	83

Preface

One of the main reasons why I signed up for the study Mechanical Engineering with the specialization track control engineering, has to do with the question:

How and why does it work ?

This particular question encouraged me to do a study at the Technical University of Delft. Especially designing and controlling complex systems is one of my favourite subjects. At the end of the second year, students with the specialization track control engineering had to follow the course 'Integration project'. One of the goals of this course was to apply control theory on a practical system. In my case, I had to design a PID controller for a double-pendulum system. Although the mechanical structure of such a system is relatively simple, it turned out to be very difficult to find 'optimal' control parameters for such a system. Most students used a trial and error approach. I tried this as well but I could not find proper parameters for the PID controller. To make things worse, other students did succeed in this task. Finally, as last resort, I tried to apply non-linear optimization algorithms in order to find feasible parameters. At some point late in the evening, my computer gave me some results. The next morning I went to the double-pendulum set-up and entered the control parameters into the computer. Surprisingly, it worked very well! At that moment I realised the power of using optimization algorithms for designing complex systems. This is indirectly also the reason why I chose a MSc assignment with the subject 'Integral Controller-Structure Optimization'. The initial idea was that I would carry out my MSc thesis at the company ASML. Unfortunately, this was not possible.

During my literature survey I found out that my assignment was closely related with topology optimization. This includes understanding the fundamentals of *finite element* (FE) modelling combined with advanced optimization techniques. Although these techniques are very interesting, my main background is control engineering. Fortunately, the Phd thesis from Paijmans [2007] brought me to the idea of using a kind of *linear parameter varying* (LPV) model in order to describe the dynamics of a parameterized structure. In this way, it was possible to combine the field of mechanical engineering and control engineering.

Acknowledgments

The master thesis report is the final piece of work that a student at the Delft University of Technology, department of Delft Center for Systems and Control (DCSC), has to make.

I would also like to thank dr.ir. Jan-Willem van Wingerden, dr.ir. Matthijs Langelaar and dr.ir. Gijs van der Veen for their feedback during our progress meetings.

This MSc thesis is supervised by:

dr.ir. Jan-Willem van Wingerden (DCSC)

dr.ir. Matthijs Langelaar (PME)

dr.ir. Gijs van der Veen (PME)

Delft, University of Technology
December 8, 2014

C. van der Marel

List of abbreviations

CSO	Controller-Structure Optimization
DOFs	Degrees of Freedom
EA	Evolutionary Algorithms
EOM	Equations of Motion
FE	Finite Element
GM	Gain Margin
ICs	Integrated Circuits
LPV	Linear Parameter Varying
LTI	Linear Time-Invariant
MAC	Modal Assurance Criterion
MOR	Model Order Reduction
MSE	Mean Square Error
PDSS	Parameter-dependent state-space
PM	Phase Margin
SISO	Single Input Single Output
SVD	Singular Value Decomposition
VAF	Percent Variance Accounted For

Chapter 1

Introduction

1-1 Motivation

Modern high-precision controlled motion systems need to be fast and accurate. An example of such a system is a wafer scanner (see figure 1-1). This machine produces *integrated circuits* (ICs) on a silicon wafer. An important component of the wafer scanner is the wafer stage. This component is a scanning positioning system with high performance requirements, i.e. scanning velocity > 0.5 [m/s], stepping velocity > 2 [m/s], acceleration > 30 [m/s] with a metrology error < 0.5 [nm] over 20 seconds (Munnig Schmidt et al. [2011]). Improving the performance of such a system often implies that the structural and control properties should be optimized as much as possible.

The problem of finding optimal parameters for a controlled (parameterized) structure is often characterized as a multi-objective and non-convex problem (Ravichandran et al. [2006], van der Veen et al. [2014]). This type of problem will be referred to as *controller-structure optimization* (CSO). In many practical cases, a sequential design approach is used in order to fulfil this task. Such a conventional approach implies a strategy where in the first stage the structure is optimized with respect to the mechanical objectives (e.g. maximizing first eigenfrequency, reducing maximum stress levels etc.). After this stage, the controller is designed with respect to the control objectives (e.g. maximizing bandwidth, reducing disturbance and noise responses etc.). If the closed-loop requirements are not achieved, an iterative process of the two design stages takes place until satisfactory results are obtained. The outcome of this process determines both the open-loop dynamics of the structure $G(s)$ (i.e. plant) and the closed-loop dynamics $G_{cl}(s)$. Notice that some of these objectives are in conflict with each other, like minimizing the mass and maximizing stiffness. However, a coupling between the mechanical and the control part of the system might exist (Fathy et al. [2001]) which makes it harder to assume that an optimal design can be obtained by decomposing the original design problem and combining each individual optimized sub-designs.

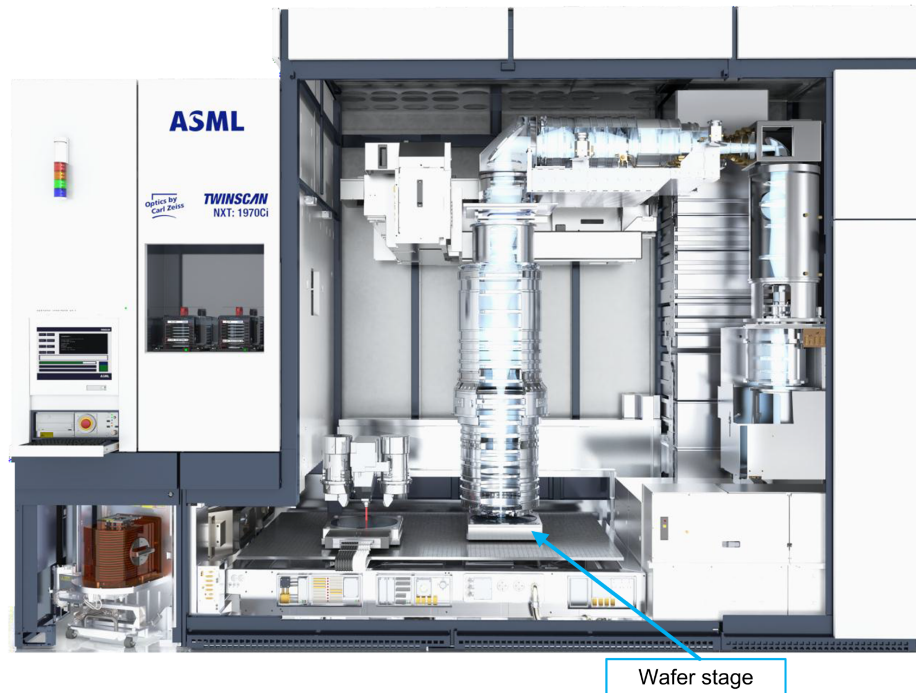


Figure 1-1: Main components in the wafer scanner NXT:1970Ci. This machine is able to produce 250 wafers per hour at improved litho performance with less than 2 [nm] overlay. (reference: website ASML, public presentation Q2 2013)

According to Fathy et al. [2001], there are four different strategies for solving CSO problems. They can be solved either sequentially, iteratively, using a nested (or bi-level) strategy or simultaneously. Recent papers from Vandyshev et al. [2012] and van der Veen et al. [2014] tried to optimize the closed-loop performance of a simplified motion control system using different design approaches. Vandyshev et al. [2012] used a sequential and nested design approach while van der Veen et al. [2014] used a sequential and integrated design approach. The closed-loop performance of the systems obtained from the nested and integrated design approaches were slightly better compared to the sequential design approach. Therefore, it is interesting to do further investigation into the field of integrated design.

1-2 Problem Statement

In the case of Vandyshev et al. [2012], first the concept of topology optimization in order to find an overall optimal shape for the controlled-structure. This result was used to formulate a parameterized structure. In the second step, the concept of shape optimization was applied in order to maximize the first eigenfrequency. Finally, a nested design approach was used to optimize the closed-loop performance by optimizing the parameters of the fixed-structure controller and the parameterized structure. The controller was defined by a transfer function and the structure was modelled in a *finite element* (FE) package. One of the main disadvantages of the approach presented by Vandyshev et al. [2012] is the use of FE models in a nested optimization environment. First, this approach implies that for every function

evaluation the eigenmodes and eigenfrequencies of the parameterized structure needs to be recomputed. For highly detailed models (i.e. many *degrees of freedom* (DOFs), e.g. cover of this MSc thesis), this takes considerable amount of time. Especially in a nested or integrated optimization environment, it is not unusual that the optimization algorithm requires multiple function evaluations before an acceptable solution is found. Therefore, this approach can be expensive and time consuming. Second, a fixed FE grid of the parameterized structure puts a restriction on the resolution. In other words, a small change of the structural parameters should be recognisable in the FE model. However, if the FE model has a fixed coarse grid, this change cannot always be modelled. Therefore, in this MSc thesis a different approach based on an approximation of the parameterized structure in the form of a *parameter-dependent state-space* (PDSS) model will be investigated. This approach was proposed by van der Marel [2014].

The main assumption behind this approximated model is that small changes in the configuration of a structure will have little effect on the dynamic behaviour of the system. If this is true, then it might be possible to approximate a parameterized structure by a set of reduced-order models derived from different configurations of the original system. A *parameter-dependent state-space* (PDSS) model will be derived by interpolating these reduced *linear time-invariant* (LTI) models. This PDSS model will be used to synthesise controllers. One of the advantages of this approach is that there are no resolution restrictions on the parameters for the PDSS model as long as they stay within the pre-described bounds. A second advantage is that the PDSS model is smaller in size compared to the original FE model. This should simplify the synthesis of controllers and reduce the time to perform simulations. A third advantage is that there is no need to recompute the eigenmodes and eigenfrequencies during the optimization process.

The main emphasis of this MSc thesis is to test the potential of this approach for solving CSO problems with a parametrized structure and a fixed-structure controller. Due to the multi-objective nature of these problems, the first goal will be to find the Pareto optimality between maximizing the bandwidth and minimizing the mass. The second goal will be to apply an integrated optimization approach. To do this, a proper optimization problem needs to be formulated. The obtained results can serve as initial guess for the comprehensive CSO problem. Note that this MSc thesis will be restricted to *single-input single-output* (SISO) systems. To test this design approach, problems like modelling well-conditioned accurate PDSS systems and formulating a proper optimization problem needs to be solved. Furthermore, indicators need to be defined in order to quantify how good the PDSS model approximates the original model (e.g. FE model).

1-3 Structure of MSc thesis

This MSc thesis is organised as follows. Chapter 2 starts with a brief description of the design approach which will be used to solve CSO problems. At the end of this chapter, a simple example of a CSO problem will be introduced. The purpose of this example is to clarify the different steps of the design approach that are involved. The techniques described in the chapters 3 to 5 will be applied to this showcase example. Chapter 3 presents more details about the conditions of the local LTI models that are obtained by taking samples of the original parameterized structure. Moreover, arguments for using a modal representation

will be given. In addition, some extra restrictions on the eigenmodes and eigenfrequencies are introduced in order to improve the conditions for interpolating these local LTI models. Chapter 4 continues with the subject of PDSS modelling. More information about defining a structure and determining the unknown coefficients of a PDSS model can be found in this chapter. Chapter 5 is devoted to the subject of formulating a proper optimization problem for a CSO problem. In addition, information about the optimization methods that are applied in this MSc thesis is given. Chapter 6 introduces a more difficult CSO problem involving a simplified single-axis motion system. The structure in this case study is modelled with FE methods and has a single actuator and a single measurement position. The techniques described in the chapters 2 to 5 are applied to this case study. Finally, the conclusion of this MSc thesis is given chapter 7.

Design approach

This chapter starts with explaining more details about the proposed design approach described in section 1-2. This design approach includes the following steps:

1. Parameterizing the structure
2. Parameterizing the controller
3. Generating a set of local models in modal form
4. Deriving a PDSS model
5. Formulating and solving a CSO problem

Each of these steps will be briefly described in the sections 2-1 to 2-5. The last section of this chapter, section 2-6, introduces a showcase example of a CSO problem that will be used in the chapters 3 to 5.

2-1 Parameterizing the structure

The first step in the design approach is to parameterize the structure. This means that it should be possible to characterize the structure by a few parameters, like length, width, depth, etc. The values of some of these parameters will be considered unknown and variable, while others are known and fixed. These unknown parameters will be referred to as the design variables \mathbf{x}_p of the structure. Note that subscript p refers to the word ‘plant’ which in turn refers to the dynamics of the structure. In step five of the approach, an attempt will be made to find ‘optimal’ values for these design variables by solving an optimization problem. In some manner this looks a lot like a sizing or shape optimization problem (Bendsøe and Sigmund [2002]) with the only difference that in this MSc thesis the criteria are based on the closed-loop dynamics, which includes the plant and controller. Therefore, actuator and measurement positions need to be assigned. Note that this MSc thesis will be restricted to controlled-structures with a *single-input-single-output* (SISO) configuration.

2-2 Parameterizing the controller

In many practical cases, motion systems are controlled by low-order (i.e. first to fourth order) fixed-structure controllers, like PID (van der Marel [2014]). This is because in general it is not practical or desirable to implement high-order controllers. Moreover, it is difficult to tune them. Therefore, in this MSc thesis a fixed-structure controller will be used to control the position of the structure. This controller is represented by the following transfer function.

$$C(s) = \underbrace{Kp}_{\text{proportional gain}} \left(\underbrace{\frac{\left(\frac{3}{\omega_c}\right)s + 1}{\left(\frac{1}{3\omega_c}\right)s + 1}}_{\text{phase lead filter}} \underbrace{\frac{1}{\left(\frac{1}{5\omega_c}\right)s + 1}}_{\text{roll-off}} \right) \quad (2-1)$$

The real valued parameters $\{Kp, \omega_c\}$ represent the design variables \mathbf{x}_c of the controller given by equation (2-1). Note that these parameters are strictly positive. Moreover, notice that the structure of this controller is essentially a lead compensator with a roll-off. It gives maximum phase around the desired bandwidth ω_c . Figure 2-1 shows a bode plot of the controller given by equation (2-1) with $\omega_c = 1$ and $Kp = 1$.

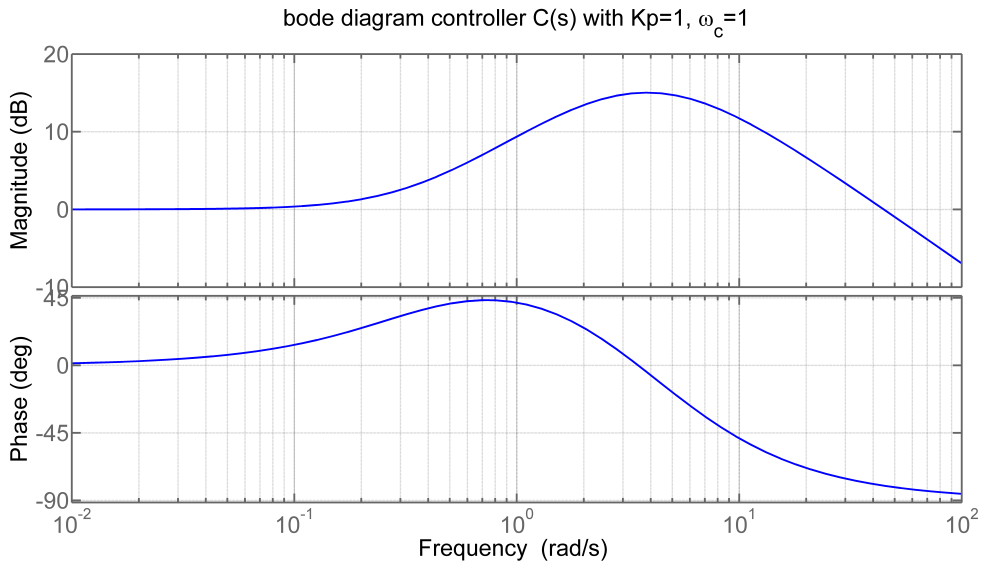


Figure 2-1: Bode plot of the controller $C(s)$ (equation (2-1)) with $\omega_c = 1$ and $Kp = 1$.

2-3 Generating a set of local models in modal form

The purpose of the third step in the design approach is to collect enough information from the original parameterized structure such that a reduced order approximate model can be derived. This approximated model will be represented in the form of a *parameter-dependent state-space* (PDSS) model. Therefore, the information from the original structure refers to a

set of local *linear time-invariant* (LTI) state-space models. They are obtained by taking N different samples from the physical structure or from mathematical models of it (e.g. FE). Each sample is characterized by a distinct choice of the values of the structural design variables \mathbf{x}_p . In the context of this MSc Thesis, the term \mathbf{x}_p will also be called *scheduling parameter* \mathbf{p} :

$$\mathbf{p} = \mathbf{x}_p \quad (2-2)$$

Furthermore, notice that it is undesirable to have a high value for N since it usually involves finding the modes of a FE model. This action is typically time-consuming and expensive. According to De Caigny et al. [2011], the number of samples should be chosen as small as possible but should be high enough such that the influence of \mathbf{p} on the system dynamics is captured. However, note that most literature related to this subject try to derive a *linear parameter varying* (LPV) model instead of a PDSS model. In many cases, an LPV model describes the dynamics of a physical system as function of certain operating points (e.g. Groot Wassink et al. [2005]). Notice that the PDSS model is different because it tries to predict the dynamics of frozen parameterized structures as accurate as possible. There is no time-varying aspect involved for the PDSS model in the context of this MSc thesis. However, this aspect cannot be neglected when an LPV model is derived for a physical system.

In step four of the design approach, a PDSS model is derived by applying *direct matrix interpolation* techniques on the local models. This often comes down to solving a (linear) least squares or non-linear optimization problem. However, the representation of the local models could have influence on how well the PDSS model approximates the dynamics of the parameterized structure. It is recommended by most literature related to model interpolation, like Pajmans [2007] and De Caigny et al. [2011], to use local models in a **coherent** representation before interpolating them. Sometimes other words like **consistent** or **invariant** are used instead. In this MSc thesis, the local models are represented in the *modal form*. From each sample of the mathematical model (e.g. FE), four structural modes are extracted. These modes are then used to construct an LTI state-space model in modal form. In order to improve the condition of the system matrices for interpolation purposes, additional techniques and restrictions will be used. These techniques and restrictions are described in chapter 3.

2-4 Deriving a PDSS model

The design approach is only useful if the accuracy of the PDSS model, which means how well the dynamics of the PDSS model approximates that of the original structure, is good enough. The mathematical formulation of the PDSS model that will be used in this MSc thesis is represented by the following expression:

$$\begin{aligned} \dot{\mathbf{x}} &= A(\mathbf{p})\mathbf{x} + B(\mathbf{p})\mathbf{u} \\ \mathbf{y} &= C(\mathbf{p})\mathbf{x} \end{aligned} \quad (2-3)$$

where \mathbf{x} is the state vector and $A(\mathbf{p}), B(\mathbf{p}), C(\mathbf{p})$ are the system matrices. The model in 2-3 is obtained by fitting data from a set of local LTI models onto a fixed-structure PDSS model with unknown parameters. Recall from the previous section that these unknown parameters are typically determined by solving a (linear) least-squares or non-linear optimization problem.

Notice that this means that the accuracy of the solution of this optimization problem has influence on the accuracy of the PDSS model. The obtained optimization solution typically depends on the chosen optimization algorithm and the settings that are being used, like the number of maximum iterations, the number of random initial conditions, termination settings etc. Another aspect that has influence on the accuracy of the PDSS model is the exact structure of the model (2-3). In this MSc thesis, a polynomial function is formulated for each varying element in the system matrices. However, this polynomial function might not be able to approximate the behaviour of each element in these matrices.

2-5 Formulating and solving a CSO problem

The abbreviation *controller-structure optimization* (CSO) already indicates that there are three main items, the controller, the structure and some criteria for optimization purposes. The third item, criteria for optimization purposes, can be defined from the requirements and specifications with respect to the controlled-structure. Recall from the introduction that CSO problems are often classified as multi-objective. For these types of problems, literature (van den Boom and de Schutter [2010], Papalambros and Wilde [2000]) refers to the concept of Pareto optimality. Therefore, the solution of a CSO problem does not necessary have to be a unique set of values for the design variables \mathbf{x}^* , but it can also be a graph which gives insight into conflicting objectives. In many cases, a trade-off has to be made in order to find a unique solution for the CSO problem. In this MSc thesis, the objective is to maximize the bandwidth ω_b and to minimize the mass m of the structure. The first target will be to approximate the Pareto optimality curve between these two properties. The second target will be to test various optimization approaches (e.g. nested, integrated). This is done by constructing a weighted sum of the objectives:

$$\min_{\mathbf{x}_d} \frac{\bar{\omega}_b}{\omega_b} + \alpha \frac{m}{\bar{m}} \quad (2-4)$$

Note that the design variables \mathbf{x}_d are composed of:

$$\mathbf{x}_d = \begin{cases} \mathbf{x}_p & \text{design variables of the structure} \in \mathbb{R}^{n_p} \\ \mathbf{x}_c & \text{design variables of the controller} \in \mathbb{R}^{n_c} \end{cases} \quad (2-5)$$

The objective given by equation (2-4) is subjected to the constraints

$$\|W_p S\|_\infty < 1 \quad (2-6)$$

$$\underline{\mathbf{x}}_d \leq \mathbf{x}_d \leq \bar{\mathbf{x}}_d \quad (2-7)$$

where $W_p(s)$ is a weight on the *sensitivity function* $S(s)$ and the over-bar and under-bar refer to respectively minimum and maximum values. The weight $W_p(s)$ is given by the following equation:

$$W_p(s) = \frac{\frac{s}{M} + \omega_b}{s + A\omega_b} \quad (2-8)$$

with $A = 0.001$ and $M = 2$ (see section 5-1). Note that the function $\frac{1}{|W_p|}$ represents an upper bound on the magnitude of $S(s)$. Moreover, the value of ω_b will be determined by solving

the optimization problem defined by the objective in equation (2-4) and the constraint (2-7). Section 5-1 explains why the sensitivity function S is used in this constraint.

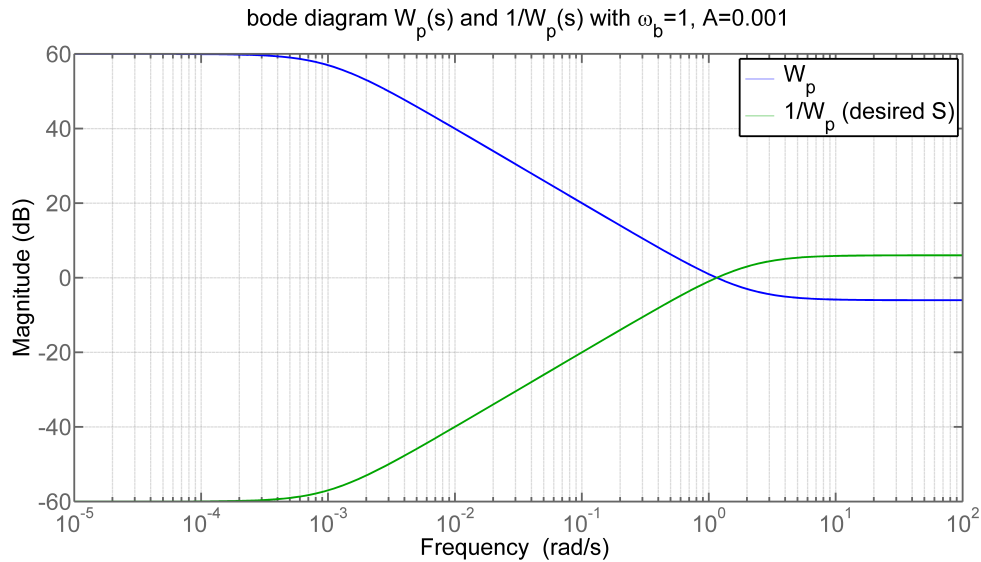


Figure 2-2: Bode plot of the weight $W_p(s)$ (equation (2-8)) and the upper bound $\frac{1}{|W_p|}$ with $\omega_c = 1$ and $A = 0.001$

2-6 Showcase example: double mass-spring-damper system

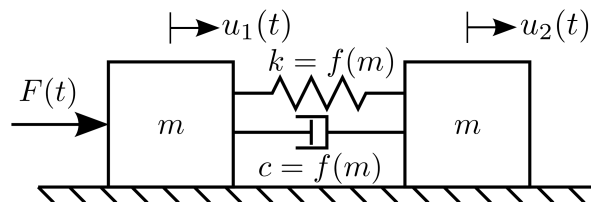


Figure 2-3: Mass-spring-damper system with a stiffness and damping coefficient which depends on the mass m

In order to clarify the various steps of the design approach, a simple academic example of a CSO problem will be used. The model that will be examined is a double-mass-spring-damper system (see figure 2-3). The mass on the left is connected to an actuator which exerts a force $F(t)$ on it. This force is determined by the controller described by equation (2-1). The position of the mass on the right is measured by a sensor. Both masses will be associated with the term m since they are equal in value. Moreover, the mass m is considered to be a structural design parameter ($\mathbf{x}_p = m$). The dynamics of this system can be described by a set of linear differential equations:

$$m\ddot{u}_1 + c(\dot{u}_1 - \dot{u}_2) + k(u_1 - u_2) = F \quad (2-9)$$

$$m\ddot{u}_2 + c(\dot{u}_2 - \dot{u}_1) + k(u_2 - u_1) = 0 \quad (2-10)$$

The transfer function between the force $F(s)$ and the position of the second mass $U_2(s)$ is:

$$G(s) = \frac{X_2(s)}{U_2(s)} = \frac{1}{2m} \frac{\frac{c}{k}s + 1}{s^2 \left(\left(\frac{s}{\omega_1} \right)^2 + 2\zeta \left(\frac{s}{\omega_1} \right) + 1 \right)} \quad (2-11)$$

with the definition for ω_1 :

$$\omega_1 = \sqrt{\frac{2k}{m}} \quad (2-12)$$

and for ζ :

$$\zeta = c \sqrt{\frac{1}{2mk}} \quad (2-13)$$

Equation (2-11) shows that for low frequencies the bode plot should have a slope of -40 [dB/dec] due to the double integrator. At a frequency of ω_1 , a damped resonance should occur with a damping ratio of ζ . Just after this first resonance peak, the slope should be approximately -80 [dB/dec]. At a frequency of $\omega_2 = \frac{k}{c}$ the numerator of $G(s)$ becomes more dominant which results in a slope of -60 [dB/dec] at high frequencies.

If the optimization criteria in section 2-5 with $\alpha = 0$ is applied to a general CSO problem, the change is relatively large so that the optimization algorithm will converge to an answer where the stiffness k is at its maximum and the mass m is at its minimum. This trivial answer implies that the first eigenfrequency ω_1 of the structure is maximized (see equation (2-12)). From control perspective, a high bandwidth ω_b can be achieved if the first eigenfrequency ω_1 of the open-loop system is high as well. The reason for this relation lies in the fact that at the first resonance frequency ω_1 , the phase of the open-loop system typically drops which has negative consequences for the stability of the closed-loop system. In order to avoid this trivial solution, the values for the stiffness k and damping c are related to the mass m (see left plots in figure 2-4). This relation is given by:

$$k = f_0 + f_1(m - a) + \frac{f_2}{2}(m - a)^2 \quad (2-14)$$

with $f_0 = 900$, $f_1 = 700$, $f_2 = -2000$ and $a = 1$. Note that the relation (2-14) is purely academic. The right plots in figure 2-4 and figure 2-5 show the effect of different mass values on the open-loop system dynamics $G(s)$. The idea behind this example is that the maximum bandwidth ω_b^* should be equal to the maximum eigenfrequency of the first flexible mode ω_1^* in the case that $\alpha = 0$ (see equation (2-4)). One of the main reasons for this assumption comes from the fact that the controller in equation (2-1) is not able to compensate for the phase loss caused by the eigenfrequency ω_1^* . Therefore, the optimal parameters are thus already known:

$$\begin{aligned} m_{opt} &\approx 0.894 \text{ [kg]} \\ k_{opt} &\approx 815 \text{ [N/m]} \\ \omega_{1,opt} &\approx 42.7 \text{ [rad/s]} \end{aligned} \quad (2-15)$$

In this way, it is possible to apply the proposed design approach and to verify the optimization results. Moreover, analysis can be done on how efficient the optimization algorithm works and

how good the PDSS model approximates the analytical system. The bounds on the values of the design variables $\mathbf{x} = \{m, Kp, \omega_c\}$ are in this example:

$$\begin{aligned} m &\in [0.35, 1.4] \\ Kp &\in [0, \infty] \\ \omega_c &\in [0, \infty] \end{aligned} \quad (2-16)$$

Figure 2-6 shows a part of the stability region for the design parameters $m \in [0.35, 1.4]$, $Kp \in [0, 100]$, $\omega_c \in [0, 25]$. The blue region indicates a stable closed-loop system $G_{cl}(s)$ and the empty region in the 3D-plot indicates an unstable closed-loop system $G_{cl}(s)$.

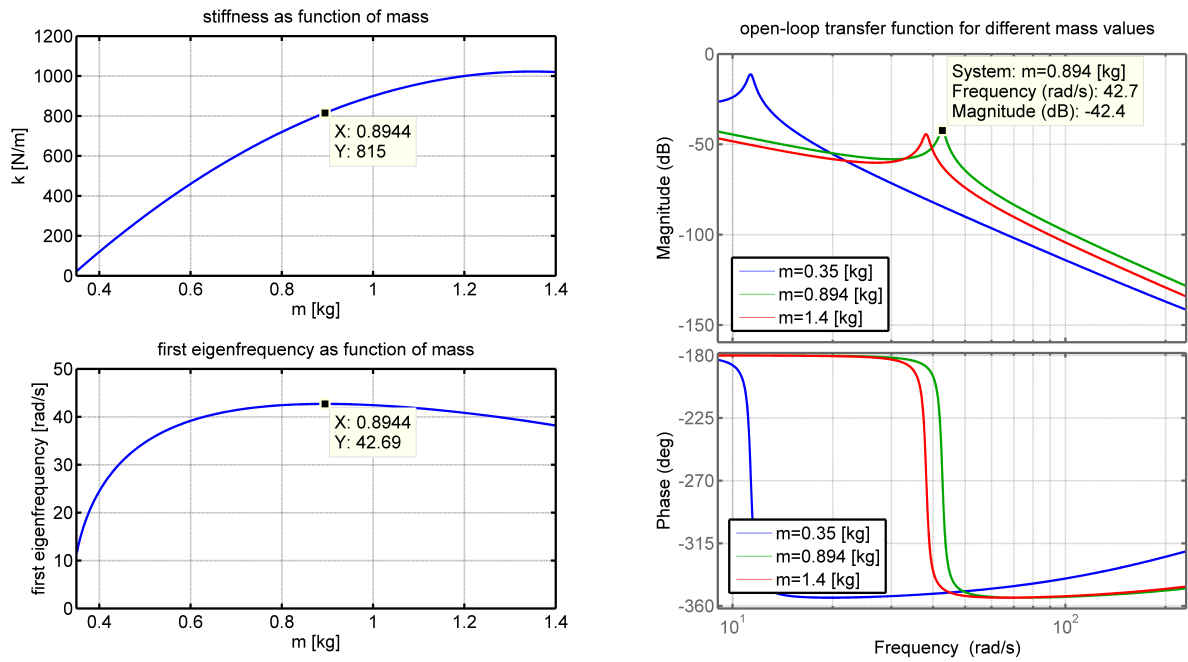


Figure 2-4: Relation between the stiffness k as function of mass m (upper left plot). First eigenfrequency ω_1 as function of mass m (lower left plot). Open-loop bode plots for three mass values (upper and lower right plots).

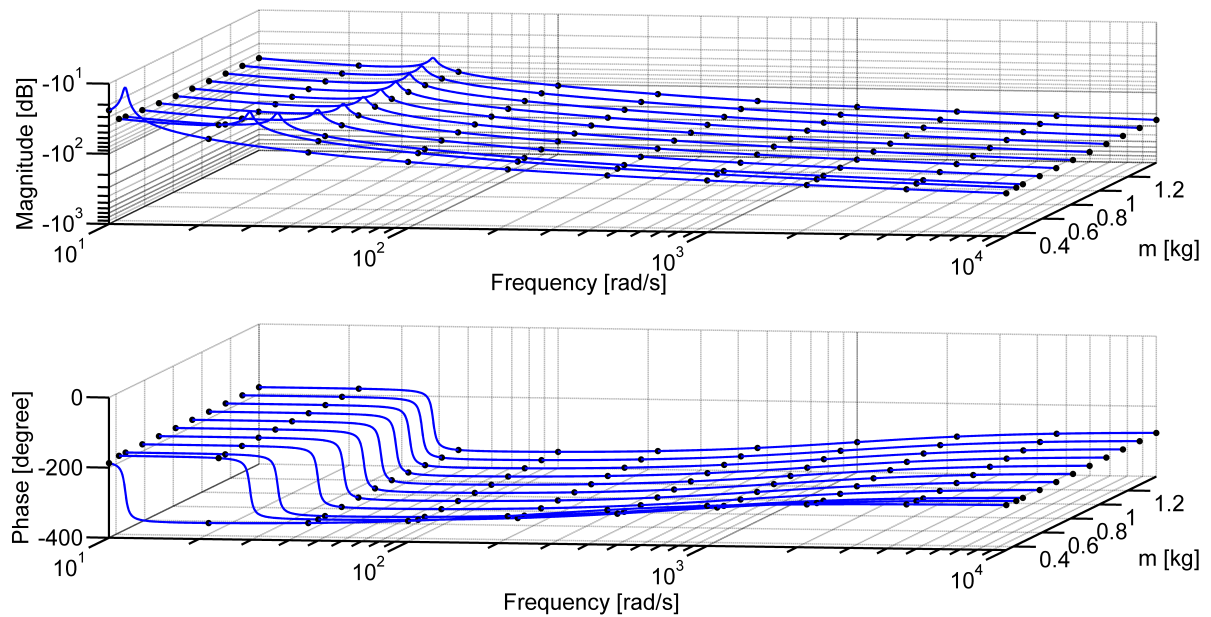


Figure 2-5: Bode diagrams for eleven different mass values.

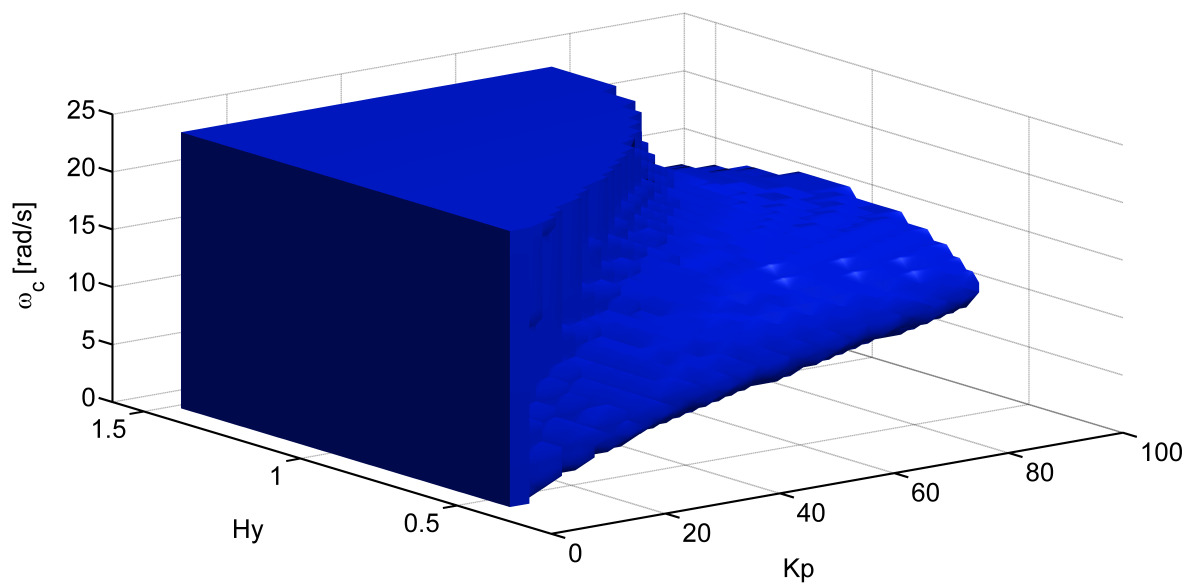


Figure 2-6: Stability region for various combinations of K_p , ω_c and m . The blue region indicates a stable closed-loop system G_{cl} and the remaining white space indicates an unstable closed-loop system.

Local models in modal state-space form

One of the most important aspects in order to obtain an accurate PDSS model is to make sure that all local LTI models have the same coherent basis (same order and same physical meaning of the states [Roos, 2012]). This chapter starts with the dilemma of choosing a suitable coherent state-space representation. Moreover, it presents arguments for choosing the modal state-space form. Section 3-2 describes the process from having a model of a structure (e.g. FE) to a set of coherent local reduced-order LTI models. Section 3-3 introduces some extra methods for improving the condition of the system matrices when mode switching occurs. Finally, this chapter finishes with applying the presented techniques on the reference example described in section 3-4.

3-1 Choosing a coherent state-space representation

Two main representations of plant models can be distinguished from literature:

1. plant model in transfer function form (e.g. Pajmans [2007])
2. plant model in state-space form (e.g. Steinbuch et al. [2003])

Pajmans [2007] used local plant models in transfer function form as basis for interpolating poles and zeros. One of the advantages of this approach is that it gives better insight in what happens between sampling points. Moreover, this method provides the ability to impose stable poles for the derived PDSS model. The disadvantages of this approach are related to the three restrictions on the local LTI models. First, the models must be single-input-single-output *SISO*. Second, each model must have the same number of real poles, complex poles, real zeros and complex zeros. Third, the N different samples should be sufficiently close in order to recognise migration of poles and zeros. The last two disadvantages also apply for

plant models in state-space form. However, this thesis will not investigate plant models in transfer function form any further due to the SISO restriction.

Most of the literature related to the topic of model interpolation use plant models in state-space form. In many cases, the elements of the system matrices are interpolated with respect to the scheduling parameter \mathbf{p} . One of the advantages of this *direct matrix interpolation* approach is that there are several operations under system similarity possible in order to improve the condition of the local LTI models for interpolating their state-space elements. It is for example possible to transform state-space matrices into different forms e.g. balanced state-space form (Lovera and Mercère [2007]), rescaled companion form (Ferrerres [2011]), modal form (Roos [2012]), control canonical form (Steinbuch et al. [2003]). Unfortunately, the latter form, the control canonical form, is not always applicable because it often leads to an ill-conditioned system. The second advantage is that it does not necessarily restrict the PDSS system and local LTI models to be SISO. One of the disadvantages of direct matrix interpolation is that in some cases the PDSS model is obtained by only focusing on how accurate the elements of the system matrices of the PDSS model match with the elements of the local models. In that case, the properties of the PDSS system, such as stability and open-loop dynamics, are neglected in some sense.

In this MSc thesis, direct matrix interpolation of modal truncated state-space models in modal state-space form will be used. The choice for the modal state-space form is based on several reasons. First, in the mechanical community it is common practice to use modes for constructing state-space systems or to analyse the structure. Another favourable property of the modal state-space form is that it has few varying elements in the system matrices. This is recommended by Steinbuch et al. [2003] because it reduces the problem of determining the unknown variables in (2-3). In addition to the previous arguments, recall that the derived PDSS model will be used for determining the optimal control and structural parameters. In this context, it is somewhat exaggerated to derive large-scale high-order models while the control performance will probably be limited by the first few eigenmodes of the system with respect to the eigenfrequencies.

3-2 Modal state-space form

In many cases the dynamics of a mechanical structure is described by linear *ordinary differential equations* (ODEs) in the form:

$$\mathbf{M}\ddot{\mathbf{q}}(t) + \mathbf{D}\dot{\mathbf{q}}(t) + \mathbf{K}\mathbf{q}(t) = \mathbf{L}\mathbf{f}(t) \quad (3-1)$$

with the real, symmetric and positive definite *mass matrix* $\mathbf{M} \in \mathbb{R}^{n \times n}$. This matrix describes the inertia forces of the system. Furthermore, the *damping matrix* $\mathbf{D} \in \mathbb{R}^{n \times n}$ contains information about the amount of energy that is dissipated by the structure and the *stiffness matrix* $\mathbf{K} \in \mathbb{R}^{n \times n}$ describes the elastic forces. The stiffness matrix is real and symmetric. Moreover, if there is no rigid body motion or internal mechanism this matrix is also positive definite, if not, it is positive semi-definite. External forces are described with the force vector $\mathbf{f} \in \mathbb{R}^{m \times 1}$. The vector $\mathbf{q} \in \mathbb{R}^{n \times 1}$ represents the *degrees of freedom* (DOFs) of the structure. Moreover, the dots on the \mathbf{q} specify the number of derivatives with respect to time (e.g. $\dot{\mathbf{q}} = \frac{d}{dt}\mathbf{q}$). The matrix $\mathbf{L} \in \mathbb{R}^{n \times m}$ is a boolean matrix selecting the actuated DOFs. Note

that the equations in (3-1) assume that the relation between force and displacement is linear and that the deformations are relatively small. Appendix A and B illustrate by means of a reference FE model, how the matrices \mathbf{M} and \mathbf{K} can be derived.

For a simple mechanical structure with few DOFs (e.g. double-mass-spring-damper system example), the matrices $\{\mathbf{M}, \mathbf{D}, \mathbf{K}\}$ in 3-1 can directly be used for simulation, analysis or controller synthesis purposes. However, this is not the case for structures defined in an FE environment with typically hundreds or thousands of DOFs. This is because it becomes computationally demanding and time-consuming to perform these tasks. Therefore, in the remainder of this section, reduced-order models will be used instead of the full system (3-1). A survey on *model order reduction* (MOR) methods for large-scale systems is given by Antoulas et al. [2001]. However, in this MSc thesis, modal truncation will be used because it is relatively easy to obtain a modal reduced state-space model. The first step of this method is assuming that the answer of resulting ODEs in (3-1) can be approximated by:

$$\mathbf{q}(t) = \tilde{\mathbf{V}}\eta(t) \quad (3-2)$$

where $\tilde{\mathbf{V}} \in \mathbb{R}^{n \times k}$ is a matrix containing a selection of eigenmodes ϕ_r of the original system in (3-1). Note that sometimes the term *modeshape* is used instead of eigenmode. The corresponding eigenfrequencies ω_r will be stored on the diagonal of the matrix $\tilde{\mathbf{U}} \in \mathbb{R}^{k \times k}$. The term $\eta(t)$ represents a set of modal coordinates. Notice that each element in $\eta(t)$ is multiplied with one of the eigenmodes ϕ_r . In some sense this means the elements in $\eta(t)$ determine how much each eigenmode ϕ_r participates in DOFs $\mathbf{q}(t)$ of the structure. The ODEs of (3-1) can be written in *modal form* by pre-multiplying with $\tilde{\mathbf{V}}^T$ and substitution of equation (3-2):

$$\underbrace{\tilde{\mathbf{V}}^T \mathbf{M} \tilde{\mathbf{V}}}_{:=\tilde{\mathbf{M}}} \ddot{\eta}(t) + \underbrace{\tilde{\mathbf{V}}^T \mathbf{D} \tilde{\mathbf{V}}}_{:=\tilde{\mathbf{D}}} \dot{\eta}(t) + \underbrace{\tilde{\mathbf{V}}^T \mathbf{K} \tilde{\mathbf{V}}}_{:=\tilde{\mathbf{K}}} \eta(t) = \underbrace{\tilde{\mathbf{V}}^T \mathbf{L} \mathbf{f}(t)}_{:=\tilde{\mathbf{F}}} \quad (3-3)$$

The size of the resulting square matrices are $\tilde{\mathbf{M}} \in \mathbb{R}^{k \times k}$, $\tilde{\mathbf{D}} \in \mathbb{R}^{k \times k}$ and $\tilde{\mathbf{K}} \in \mathbb{R}^{k \times k}$. Equation (3-3) can be rewritten in the state-space form:

$$\begin{bmatrix} \dot{\eta}(t) \\ \ddot{\eta}(t) \end{bmatrix} = \begin{bmatrix} \mathbf{0} & \mathbf{I} \\ -\tilde{\mathbf{M}}^{-1}\tilde{\mathbf{K}} & -\tilde{\mathbf{M}}^{-1}\tilde{\mathbf{D}} \end{bmatrix} \begin{bmatrix} \eta(t) \\ \dot{\eta}(t) \end{bmatrix} + \begin{bmatrix} \mathbf{0} \\ \tilde{\mathbf{M}}^{-1}\tilde{\mathbf{F}} \end{bmatrix} \mathbf{f}(t) \quad (3-4)$$

The set of ODEs in (3-4) will be referred to as the *modal state space form*. The damping matrix \mathbf{D} in (3-1) is typically constructed by combining the \mathbf{M} and \mathbf{K} matrices or by putting a damping coefficient on each eigenfrequency ω_r . In this MSc thesis, the matrix $-\tilde{\mathbf{M}}^{-1}\tilde{\mathbf{D}}$ is replaced by:

$$-\tilde{\mathbf{M}}^{-1}\tilde{\mathbf{D}} = -2\zeta \text{diag}(\omega_r) \quad (3-5)$$

with $\zeta = 0.005$. The value for ζ is small which indicates little damping of the structure [Munnig Schmidt et al., 2011]. The system (3-4) can be rewritten into the state-space form:

$$\begin{aligned} \dot{\mathbf{x}}(t) &= \mathbf{A}\mathbf{x}(t) + \mathbf{B}\mathbf{u}(t) \\ \mathbf{y}(t) &= \mathbf{C}\mathbf{x}(t) \end{aligned} \quad (3-6)$$

Notice that there is no direct term (\mathbf{D} -matrix) present in the general state-space description given by (3-6). If there was a direct term, the system (3-6) would imply that an input signal

$\mathbf{u}(t)$ would directly be measured at the output $\mathbf{y}(t)$. In other words, the system (3-6) would not be strictly proper which does not occur for physical systems.

In order to define the \mathbf{C} matrix, let $\mathbf{S}_q \in \mathbb{R}^{n \times p}$ be a selection matrix for the original DOFs vector \mathbf{q} and let $\mathbf{S}_{\dot{q}} \in \mathbb{R}^{n \times p}$ be a selection matrix for the derivatives of $\dot{\mathbf{q}}$. These matrices define the measurement points with respect to $[\mathbf{q}\dot{\mathbf{q}}]^T$. Note that the value of p determines the amount of measurement points that is available. Now the matrix \mathbf{C} becomes:

$$\mathbf{C} = \begin{bmatrix} \mathbf{S}_q^T \tilde{\mathbf{V}} & \mathbf{S}_{\dot{q}}^T \tilde{\mathbf{V}} \end{bmatrix} \quad (3-7)$$

The numerical condition and the representation of the modal state-space matrices in (3-4) and (3-7) can be improved. First, notice that the term $-\tilde{\mathbf{M}}^{-1}\tilde{\mathbf{K}}$ is essentially a diagonal matrix with the *Rayleigh quotient* on the diagonal. The Rayleigh quotient is defined as:

$$\frac{\gamma_r}{\mu_r} = \frac{\phi_r^T \mathbf{K} \phi_r}{\phi_r^T \mathbf{M} \phi_r} = \omega_r^2 \quad (3-8)$$

Recall from linear algebra that an eigenvector ϕ of a matrix \mathbf{A} has the following property:

$$\mathbf{A}\phi = \lambda\phi \quad (3-9)$$

This implies that an eigenvector only describes the direction of a mode. It is thus allowed to multiply an eigenvector with any real constant (e.g. 5 or -1 .) In context of this MSc thesis, this property could cause non-smooth behavior in elements of the system matrices because there are no restriction on the scaling factor of each individual mode ϕ_r . Therefore, in this MSc thesis, the modal mass μ_r will be by definition equal to one, $\mu_r := 1$. Moreover, the sign of the first element of the eigenmode ϕ_r is by definition positive for all local LTI models.

3-3 Ordering modeshapes

In section 6-3 the phenomenon of 'mode switching' will be introduced which will later on be further investigated in section 6-7. Mode switching can occur during a change in the configuration of a structure. Assume for example that a parameterized structure which has a modeshape ϕ_1 with corresponding eigenfrequency ω_1 and a modeshape ϕ_2 with corresponding eigenfrequency ω_2 . Moreover, assume that for this structure $\omega_1 < \omega_2$. Now it can occur that by changing the parameters of the structure a little bit, the relation $\omega_1 < \omega_2$ changes into $\omega_2 < \omega_1$. This phenomenon could lead to discontinuous (i.e. non-smooth) behaviour in the elements of the system matrices \mathbf{A} , \mathbf{B} and \mathbf{C} . For interpolating purposes, discontinuous behaviour of the elements is very unwanted because it is difficult to describe this non-smoothness by a mathematical function (e.g. polynomial, affine etc.). Notice that this discontinuous behaviour in the entries of the system matrices is directly related to the construction of $\tilde{\mathbf{V}}$ and $\tilde{\mathbf{U}}$. This can be observed by the equations (3-4) and (3-7). Therefore, section 3-2 already introduced two restrictions on the modes ϕ_r :

1. $\mu_r := 1$
2. $\text{sign}(\phi_r(1)) = 1$

However, nothing has yet been said about the ordering of the modeshapes in the matrix $\tilde{\mathbf{V}}$ and indirectly the ordering of the eigenfrequencies in $\tilde{\mathbf{U}}$. Note that $\tilde{\mathbf{V}}$ and $\tilde{\mathbf{U}}$ has the following structure:

$$\tilde{\mathbf{V}} = [\phi_1 \quad \cdots \quad \phi_k] \quad (3-10)$$

$$\tilde{\mathbf{U}} = \text{diag}(\omega_r) = \begin{bmatrix} \omega_1 & & \\ & \ddots & \\ & & \omega_k \end{bmatrix} \quad (3-11)$$

In this MSc thesis, two types of ordering will be compared. The first type places the modes ϕ_r in order of increasing eigenfrequency ω_r , thus $\omega_1 < \omega_2 < \cdots < \omega_m$. The second type orders the modes ϕ_r according to their *modeshapes*. According to Roos [2012], two strategies can be adopted for this purpose:

1. Use an indicator for the similarity between two eigenvectors ϕ_1 and ϕ_2 . This can for example be done by $\cos^2(\sigma) = \frac{(\phi_1^T \phi_2)^2}{|\phi_1|^2 |\phi_2|^2}$ where σ represents the angle between the two eigenvectors.
2. Comparing the distances between the eigenvalues of different reduced order models. This can also be done by their trajectories in the complex plane.

Note that the first item in the list is sometimes associated with the name *Modal Assurance Criterion* (MAC) [Pastor et al., 2012]. It results in a scalar with a value between zero and one. In the context of this MSc thesis, a value close to one indicates that ϕ_1 and ϕ_2 describe the same modeshape while a value of zero indicates that ϕ_1 and ϕ_2 describe different modeshapes. Another more crude approach in order to determine if two modes have the same modeshape is given by the following equation:

$$r_\phi = \sum ||\phi_1| - |\phi_2|| \quad (3-12)$$

The indicator r_ϕ is basically a residual value which is calculated by taking the absolute difference of the two modes. Note that equation (3-12) requires that the modeshapes ϕ_1 and ϕ_2 satisfy the above mentioned restrictions.

In this MSc thesis, ordering on basis of modeshapes starts with computing multiple modes for a single configuration. These modes will be used as reference for other configurations of the parameterized structure. The second step is to select those DOFs that characterize the modeshape without being significantly influenced by a change in the structure. These DOFs will be called ϕ_{ch} . In practice it comes down to comparing the ϕ_{ch} of the mode ϕ_r of a computed configuration with all the ϕ_{ch} of the reference modes.

3-4 Showcase example: double mass-spring-damper system

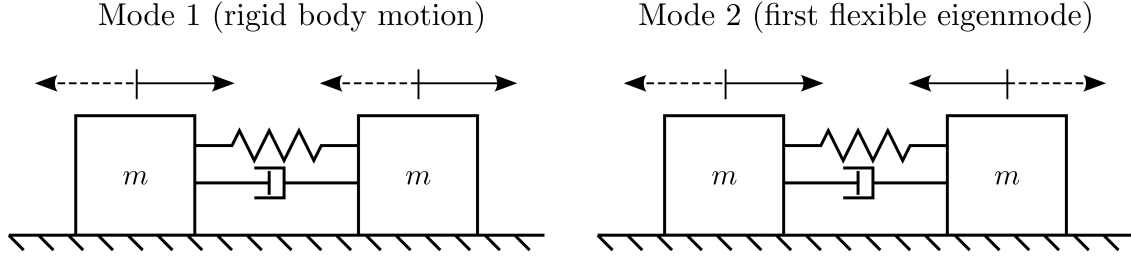


Figure 3-1: Modes of the example double-mass-spring-damper system

The differential equations of the double-mass-spring-damper system in (2-9) and (2-10) can be written into the form of equation (3-1):

$$\begin{bmatrix} m & 0 \\ 0 & m \end{bmatrix} \begin{bmatrix} \ddot{u}_1 \\ \ddot{u}_2 \end{bmatrix} + \begin{bmatrix} c & -c \\ -c & c \end{bmatrix} \begin{bmatrix} \dot{u}_1 \\ \dot{u}_2 \end{bmatrix} + \begin{bmatrix} k & -k \\ -k & k \end{bmatrix} \begin{bmatrix} u_1 \\ u_2 \end{bmatrix} = \begin{bmatrix} 1 \\ 0 \end{bmatrix} f(t) \quad (3-13)$$

Solving the *free vibration problem* described in appendix D for this example gives the following eigenfrequencies:

$$\begin{aligned} \omega_1 &= 0 \quad [rad/s] \\ \omega_2 &= \sqrt{\frac{2k}{m}} \quad [rad/s] \end{aligned}$$

Recall that the stiffness k and damping c depend on mass m . The corresponding modes are (see figure 3-1):

$$\begin{aligned} \eta_1 &= \begin{bmatrix} 1 \\ 1 \end{bmatrix} \\ \eta_2 &= \begin{bmatrix} 1 \\ -1 \end{bmatrix} \end{aligned} \quad (3-14)$$

Note that the technique of ordering modes described in section 3-3 cannot be used here because the eigenfrequency ω_1 , which corresponds to the rigid body mode (η_1 and ω_1), will not change in value and the eigenfrequency ω_2 will always be larger than zero due to the earlier prescribed bounds (2-16). The modal mass, damping and stiffness matrices can now be computed. This results in:

$$\begin{aligned} \tilde{\mathbf{M}} &= \begin{bmatrix} 2m & 0 \\ 0 & 2m \end{bmatrix} \\ \tilde{\mathbf{C}} &= \begin{bmatrix} 0 & 0 \\ 0 & 4c \end{bmatrix} \\ \tilde{\mathbf{K}} &= \begin{bmatrix} 0 & 0 \\ 0 & 4k \end{bmatrix} \end{aligned}$$

Finally, the general modal state-space representation can be constructed:

$$\begin{bmatrix} \dot{x}_1 \\ \dot{x}_2 \\ \dot{x}_3 \\ \dot{x}_4 \end{bmatrix} = \begin{bmatrix} 0 & 0 & 1 & 0 \\ 0 & 0 & 0 & 1 \\ \omega_1^2 & 0 & 0 & 0 \\ 0 & \omega_2^2 & 0 & \frac{-2c}{m} \end{bmatrix} \begin{bmatrix} x_1 \\ x_2 \\ x_3 \\ x_4 \end{bmatrix} + \begin{bmatrix} 0 \\ 0 \\ \frac{1}{2m} \\ \frac{1}{2m} \end{bmatrix} f(t)$$

$$y = \begin{bmatrix} 1 & -1 & 0 & 0 \end{bmatrix} \begin{bmatrix} x_1 \\ x_2 \\ x_3 \\ x_4 \end{bmatrix} \quad (3-15)$$

For this example, four sample points for the mass m are initially computed from the system 3-15.

1. $m = 0.35$ [kg]
2. $m = 0.70$ [kg]
3. $m = 1.05$ [kg]
4. $m = 1.40$ [kg]

Notice that an equally spaced sampling grid is used. From this information the behaviour of the elements in the system matrices can be illustrated. This is shown by the figures 3-2 to 3-4. The modal state-space form described in equation (3-4) is clearly visible in these figures.

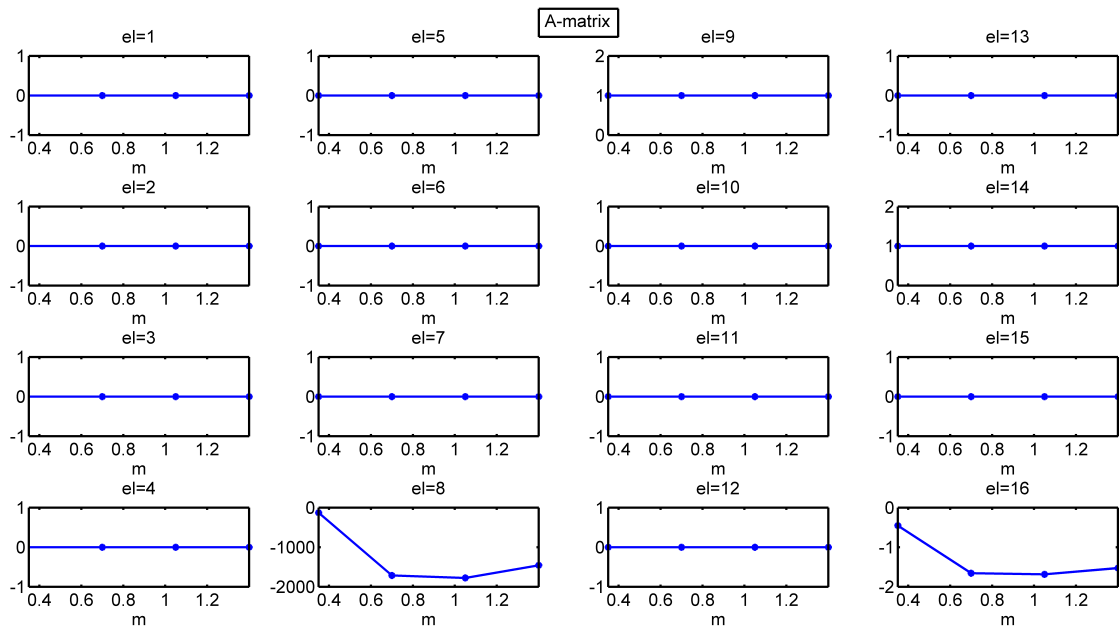


Figure 3-2: Element behavior of the A-matrix based on four samples of the original system.

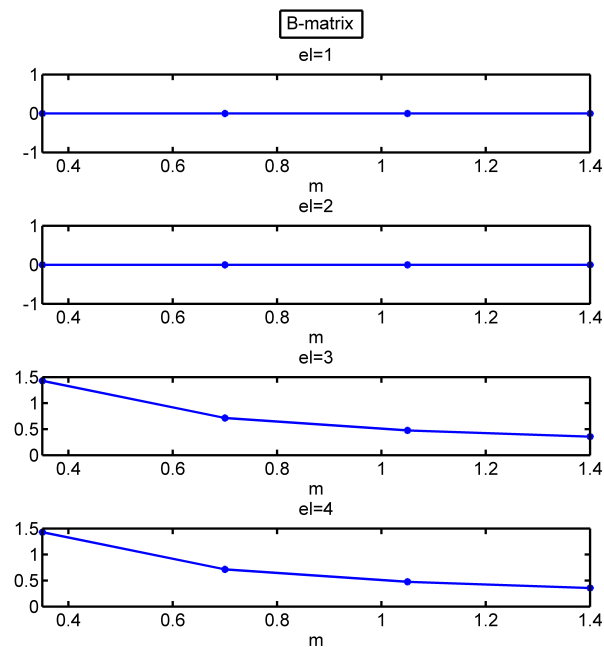


Figure 3-3: Element behavior of the B-matrix based on four samples of the original system.

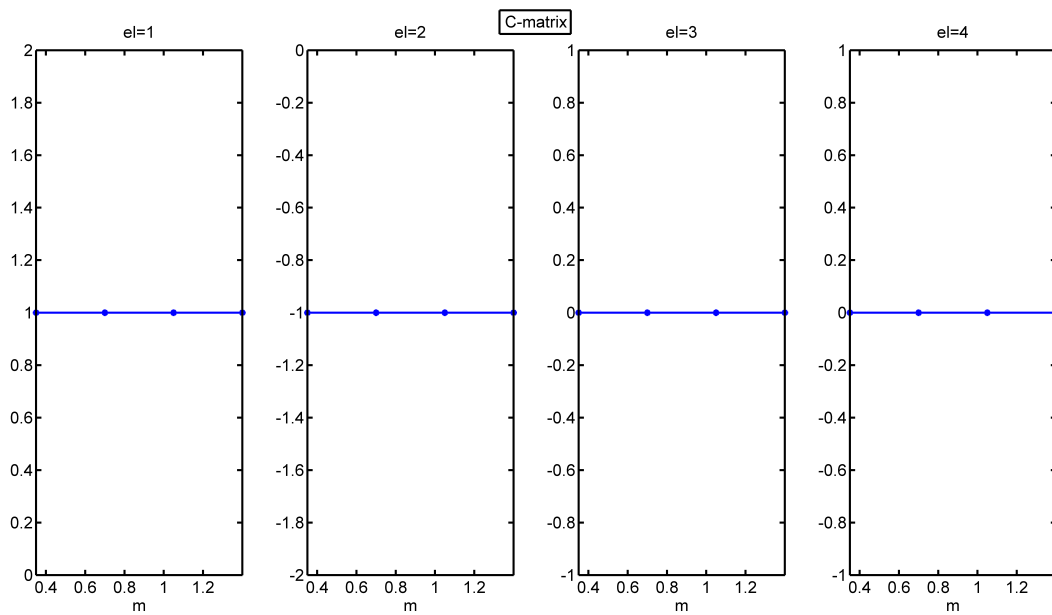


Figure 3-4: Element behavior of the C-matrix based on four samples of the original system.

Parameter-dependent state-space (PDSS) modelling

This chapter treats the subject of deriving an approximate model for a mechanical structure in the form of a PDSS model. Section 4-1 starts with an exact definition of the PDSS model which will be used in this MSc thesis. However, the problem of deriving a PDSS model can be simplified in some cases by interpolating certain varying elements of the system matrices instead of interpolating the entire matrices. Therefore, varying and non-varying entries in the coherent system matrices need to be determined. This topic is discussed in section 4-2. Section 4-3 describes how to determine the unknown coefficients of the PDSS model by solving a linear least squares problem. Section 4-4 defines several indicators for quantifying the accuracy of the obtained PDSS model. Finally, in section 4-5, the techniques described in this chapter are applied to the showcase example presented earlier in section 2-6.

4-1 PDSS model structure

The PDSS model of equation (2-3) can also be represented by the following augmented matrix $\mathbf{P}(\mathbf{p})$:

$$\mathbf{P}(\mathbf{p}) = \begin{pmatrix} \mathbf{A}(\mathbf{p}) & \mathbf{B}(\mathbf{p}) \\ \mathbf{C}(\mathbf{p}) & \mathbf{0} \end{pmatrix} \quad (4-1)$$

Notice that the PDSS model $\mathbf{P}(\mathbf{p})$ is still somewhat general. Consider for example the term $\mathbf{A}(\mathbf{p})$. This term states that the system matrix \mathbf{A} is a function of the scheduling parameter $\mathbf{p} \in \mathbb{R}^{n_p}$ (recall equation (2-2)). However, it does not exactly specify how this dependency is formulated. It could be linear, non-linear, affine, polynomial, rational or something else. For example Paijmans [2007] used an affine and polynomial dependency for describing the dynamics of an Flex-cell pick-and-place machine. A rational relation was used by Vizer and Mercère [2014] for describing a translational two-mass-spring system. In fact, according to Ferreres [2011] it remains an open issue how to choose this dependency.

In this MSc thesis, the PDSS model $\mathbf{P}(\mathbf{p})$ will be described by:

$$\mathbf{P}(\mathbf{p}) = \sum_{j=1}^{j_{max}} \mathbf{f}_j(\mathbf{p})\mathbf{P}_j \quad (4-2)$$

where $\mathbf{f}_j(\mathbf{p})$ represents a polynomial function of \mathbf{p} and \mathbf{P}_j are the unknown matrices that need to be determined. The structure of the PDSS model in (4-2) is inspired from Ferreres [2011]. The formulation of $\mathbf{f}_j(\mathbf{p})$ will be given by:

$$\mathbf{f}(\mathbf{p}) = \left\{ \prod_{i=1}^{n_p} p_i^l \right\} \quad l \in \{0, \dots, mo\} \quad (4-3)$$

where mo represents the maximum polynomial order. Due to the relation 4-3, the maximum number of unknown matrices j_{max} is determined by the equation:

$$j_{max} = (mo + 1)^{n_p} \quad (4-4)$$

Take for example a scheduling parameter with two parameters, width w and height h :

$$\mathbf{p} = \{w, h\} \quad (4-5)$$

and let the maximum order mo of the polynomial be two. In that case the polynomial function becomes:

$$\mathbf{f}(\mathbf{p}) = \{w^0h^0 \quad w^1h^0 \quad w^2h^0 \quad w^0h^1 \quad w^1h^1 \quad w^2h^1 \quad w^0h^2 \quad w^1h^2 \quad w^2h^2\} \quad (4-6)$$

Substitution of 4-6 in equation (4-2) gives:

$$\mathbf{P}(\mathbf{p}) = w^0h^0 \left[\begin{array}{c|c} \mathbf{A}_0 & \mathbf{B}_0 \\ \mathbf{C}_0 & \mathbf{0} \end{array} \right] + w^1h^0 \left[\begin{array}{c|c} \mathbf{A}_1 & \mathbf{B}_1 \\ \mathbf{C}_1 & \mathbf{0} \end{array} \right] + \dots + w^2h^2 \left[\begin{array}{c|c} \mathbf{A}_9 & \mathbf{B}_9 \\ \mathbf{C}_9 & \mathbf{0} \end{array} \right] \quad (4-7)$$

Notice that there are nine unknown matrices \mathbf{P}_j , $j_{max} = 9$, which is in agreement with equation (4-4).

4-2 Fixing elements in state-space matrices

Recall from the previous section that the j_{max} unknown matrices \mathbf{P}_j need to be determined before the PDSS model is completely defined. These matrices can be found by fitting the data from the local LTI models onto a fixed-structure PDSS model, which in this case is given by equation (4-2). However, sometimes it is possible to reduce this problem. This can be the case for PDSS models where the system matrices $\mathbf{A}(\mathbf{p})$, $\mathbf{B}(\mathbf{p})$, $\mathbf{C}(\mathbf{p})$ are restricted to a certain form (i.e. representation). The next step would be to distinguish elements in these system matrices that are **varying** and elements that are **not varying** as function of the \mathbf{p} . If such a distinction can be made, then it would be logical to reduce the original problem of interpolating the matrices \mathbf{P}_j to a problem of interpolating individual elements of these system matrices. The other elements that do not show any varying behaviour as function of \mathbf{p} will be held fixed.

Now the question arises how to determine which elements should be fixed and which elements should vary. There are at least two options thinkable. The first one assumes that the representation of the PDSS system is known *a priori*. This implies that every *frozen PDSS* model (i.e. state-space system description for a single \mathbf{p}) has the same representation. From this representation, the entries of the varying and non-varying elements are therefore known. The second option is to determine the varying and non-varying elements by investigating the set of coherent local LTI models which are generated via sampling (recall section 2-3). In principle, the result for both methods should be the same.

In this MSc thesis, all the local LTI models and frozen PDSS models are represented in the modal state-space form (recall chapter 3). These local LTI models will be allocated by the augmented matrix \mathbf{Q}_k :

$$\mathbf{Q}_k = \begin{pmatrix} \mathbf{A} & \mathbf{B} \\ \mathbf{C} & \mathbf{0} \end{pmatrix} \quad \forall k \in 1 \dots N \quad (4-8)$$

where the index k is used to indicate a particular local LTI model. The entries of \mathbf{Q} will be investigated in order to distinguish the varying and non-varying elements (option two). This process starts with looping over all the entries in \mathbf{Q} . Let \mathbf{e}_n be denoted by a vector with element values that corresponds to the i th row and to the j th column in \mathbf{Q} . The subscript n represents an index which corresponds to the i th and j th position in \mathbf{Q} :

$$\mathbf{e}_n = \mathbf{Q}_k(i, j) \quad \forall k \in 1 \dots N \quad (4-9)$$

The values of \mathbf{e}_n are assembled from the N available local LTI models. For each \mathbf{e}_n , the following statistical indicators are calculated:

- mean $\bar{e}_n = \frac{1}{N} \sum_{k=1}^N \mathbf{e}_n(k)$
- standard deviation $\sigma(e_n) = \left(\frac{1}{N-1} \sum_{k=1}^N (e_n(k) - \bar{e}_n)^2 \right)^{\frac{1}{2}}$

In this MSc thesis, if $|\sigma(e_n)| < 10^{-4}$ is true, the element of index n will be held fixed. If not, the element of index n will be considered varying unless the value of this element is extremely small ($\bar{e}_n < 10^{-4}$). In that case, it will be held fixed with a value of zero. Note that these conditions are not unique because they depend on the magnitudes of the individual elements in \mathbf{Q}_k

4-3 Linear Least Squares Approach

The unknown values of the varying entries in \mathbf{P}_j need to be determined in order to complete the PDSS model in (4-2). This problem will be solved by minimizing the least-squares error for each varying element in $\mathbf{P}(\mathbf{p})$. Note that this least-squares approach is often used for

this purpose because it is relatively efficient (e.g. [De Caigny et al., 2011], [Ferrerres, 2011]). In general, the following equation holds for linear least squares problems:

$$\underbrace{\mathbf{r}}_{\text{residual}} = \underbrace{\mathbf{y}}_{\text{data}} - \underbrace{\hat{\mathbf{y}}}_{\text{fit}} \quad (4-10)$$

where \mathbf{r} is a vector which represents the residual error between the 'true' and model data. A perfect match is found when $\mathbf{r} = \mathbf{0}$. However, this is not always possible because the model is often not comprehensive enough. Therefore, the goal will be to minimize $|\mathbf{r}|$. Equation (4-10) can be rewritten in matrix form:

$$\mathbf{y} = \mathbf{X}\beta + \epsilon \quad (4-11)$$

where \mathbf{y} is a vector containing the values of the varying elements of the local LTI models. The vector β contains the unknown coefficients of the varying elements in \mathbf{P}_j . The matrix \mathbf{X} is constructed from the polynomial function $\mathbf{f}_j(\mathbf{p})$ and the known samples \mathbf{p} . The ϵ term represents the residual error vector. Due to the polynomial relation of the PDSS model described by equation (4-2), it is possible to solve the unknown coefficients related to a single varying entry independently. In order to illustrate how equation (4-11) looks like for a single varying entry, recall the small example earlier introduced in section 4-1 where $\mathbf{p}^{(k)}$ is defined by equation (4-5) for the k th local LTI model and with $mo = 2$. Now assume that there are four local LTI models available ($N = 4$) and that \mathbf{e}_1 contains the element values that corresponds to the varying entry positioned at the i th row and at the j th column in \mathbf{Q} . In that case, equation (4-11) looks like:

$$\begin{bmatrix} \mathbf{e}_1(1) \\ \vdots \\ \mathbf{e}_1(4) \end{bmatrix} = \begin{bmatrix} \mathbf{f}_1(\mathbf{p}^{(1)}) & \dots & \mathbf{f}_9(\mathbf{p}^{(1)}) \\ \vdots & \vdots & \vdots \\ \mathbf{f}_1(\mathbf{p}^{(4)}) & \dots & \mathbf{f}_9(\mathbf{p}^{(4)}) \end{bmatrix} \begin{bmatrix} \beta(1) \\ \vdots \\ \beta(9) \end{bmatrix} + \begin{bmatrix} \epsilon(1) \\ \vdots \\ \epsilon(4) \end{bmatrix} \quad (4-12)$$

In this MSc thesis the MATLAB command `mldivide` is used to solve the linear least squares problem. As final remark, note that the least squares problem can be *underdetermined* depending on the maximum order mo (see equation (4-3)) and the amount of local LTI models N . In the context of this MSc thesis, an underdetermined least squares problem is created when the following condition is true:

$$N < j_{max} \quad (4-13)$$

4-4 Validation of PDSS model

The previous sections in this chapter explained how to derive a PDSS model. In the context of this MSc thesis, it is also important to know how good the PDSS model approximates the original plant. If the PDSS model is not accurate, the results of the optimization process in step five of the proposed design approach probably become useless. Therefore, this section introduces some methods for indicating how well the PDSS model approximates the original plant.

In the field of system identification, several approaches are used to validate LPV models. Common methods are for example *Mean Square Error* (MSE) and *Percent Variance Accounted For* (VAF) [Verdult, 2002]. However, one of the main differences between an LPV model and a PDSS model is that an LPV model has to take time-varying behaviour of the scheduling parameter \mathbf{p} into account. This is not an issue for the PDSS model that will be used in this MSc thesis. Therefore, other indicators for validating the PDSS model will be used, namely:

- residual after least squares optimization
- error system
- gap metric

The first indicator refers to the residual error vector ϵ in equation (4-11). It is reasonable to assume that the 2-norm of this vector gives some indication about how good the elements of the PDSS system matches the elements of the local models.

$$E_r = |\epsilon|_2 \quad (4-14)$$

Note that the outcome of this indicator is very relative because it depends on the magnitude of the individual elements and the number of local LTI models N . Moreover, preservation of properties like stability, open-loop dynamics etc. are not taken into account by this indicator.

The second indicator is based on the difference between a local LTI model and a PDSS model for the same \mathbf{p} . Consider for example two LTI systems, one of them represents the original system $G_{true}(s)$ and the other system is an approximation $G_{pdss}(s)$. Since these systems are defined in the Laplace domain it is allowed to subtract them. The resulting transfer function will be defined as the error system $E(s)$.

$$E(s) = G_{true}(s) - G_{pdss}(s) \quad (4-15)$$

Note that only the magnitude of the frequency response of the error system $E(s)$ gives valuable information about how much $G_{pdss}(s)$ approximates $G_{true}(s)$. The block diagram in figure 4-1 tries to make this clear. Bosgra [2009-2010] used for example the same definition for the error transfer function $E(s)$ but now the original system $G_{true}(s)$ can be decomposed in two parts. Notice that in this case, $E(s)$ is equal to the transfer function $G_{oc}(s)$ which typically represents near-uncontrollable, near-unobservable negligible higher dynamics. Now it becomes clear that for a good approximation of G_{pdss} , the error transfer function $E(s) = G_{oc}(s)$ should have a low gain with respect to $G_{oc}(s)$. The phase of $E(s)$ does not have any significant meaning in the context of indicating the accuracy of the approximated model G_{pdss} .

The second indicator that will be used for validation purposes is described by the following equation:

$$E_{tot} = \frac{1}{M} \sum_{\omega_i=\omega_1}^{\omega_M} \max_{j \in \{1 \dots N_v\}} \left\{ \sigma \left(\frac{E(j\omega_i)}{G_{true}(j\omega_i)} \right) \right\}_j \quad \forall \omega_i \in \omega_1 \dots \omega_M \quad (4-16)$$

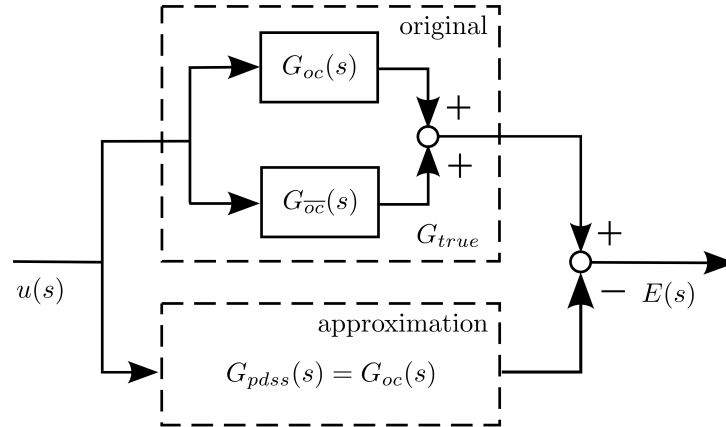


Figure 4-1: Block diagram of a particular error system $E(s)$ [Bosgra, 2009-2010]

Equation 4-16 loops through a (dense) grid of N_v generated samples of the original system. Note that N_v is typically much larger than N . For each sample, the singular values are computed and stored for the term $\left(\frac{E(j\omega)}{G_{true}(j\omega)}\right)$. The next step is to loop through a logarithmically spaced grid of frequencies ω_i of M points between ω_1 and ω_M . This range of frequencies should be of interest for control design. Then, the maximum singular value of $\left(\frac{E(j\omega_i)}{G_{true}(j\omega_i)}\right)$ for the frequency ω_i over all N_v models is determined. This is done for all ω_i frequencies and the determined values are added with each other. Finally, the result is multiplied with $\frac{1}{M}$ in order to reduce the effect of the value M on the outcome of E_{tot} . Note that the singular value response σ of a SISO system is identical to its Bode magnitude response.

The third and fourth indicators make use of the Vinnicombe gap metric δ_v . Given two systems, P_1 and P_2 , the δ_v -gap is computed by Vinnicombe [1993]:

$$\delta_v(P_1, P_2) := \begin{cases} \left\| (I + P_2 P_2^*)^{-\frac{1}{2}} (P_1 - P_2) (I + P_1 P_1^*)^{-\frac{1}{2}} \right\|_{\infty}, & \text{if } \text{Index}(P_1, P_2) = 0 \\ 1, & \text{otherwise} \end{cases} \quad (4-17)$$

where $P^* = P^T(-s)$, $\text{Index}(P_1, P_2) := \eta(P_1, P_2^*) - \text{deg}(P_2)$ and η represents the number of open RHP poles and deg denotes the McMillan degree. The Vinnicombe gap metric δ_v in equation (4-17) can be interpreted as a distance measure between two LTI models. Note that this δ_v is always between zero and one. A δ_v which is close to zero implies that P_1 and P_2 have similar dynamics. A δ_v close to one indicates that the dynamics of P_1 and P_2 are completely different. In the context of this MSc thesis, the Vinnicombe gap metric δ_v is computed for all N_v local LTI models and corresponding PDSS models. The third indicator is equal to the maximum of all N_v gap metrics. The fourth indicator takes the mean value of all N_v gap metrics

$$E_{\nu_{g\infty}} = \max_{i \in \{1 \dots N_v\}} \delta_i \quad (4-18)$$

$$E_{\nu_{g2}} = \frac{1}{N_v} \sum_{i=1}^{N_v} \delta_i \quad (4-19)$$

4-5 Showcase example: double mass-spring-damper system

Section 3-4 described how to generate a set of local LTI models in modal state-space form. The figures 3-2 to 3-4 illustrated the behaviour of the elements of the system matrices \mathbf{A} , \mathbf{B} , \mathbf{C} based on four equally distributed samples. Both these figures and the general representation of the modal state-space system given by (3-4) indicate that there are entries in \mathbf{Q} which contain varying elements and entries that contain non-varying elements with respect to \mathbf{p} . Let the numbering of these elements in a system matrix go from top to bottom and from left to right. It starts at the top-left position and it ends at the bottom-right position. The theory described in section 4-2 resulted in the MATLAB functions `prean_statistics_el.m` and `autofixel.m`. The first function determines statistical properties like \bar{e}_n and $\sigma(e_n)$. The second function determines the varying and non-varying entries in \mathbf{Q} . Moreover, it specifies the element values for the non-varying entries. For the double mass-spring-damper system described in section 2-6, the following varying elements are computed:

$$\begin{aligned} \mathbf{A} &: \begin{bmatrix} 8 & 16 \end{bmatrix} \\ \mathbf{B} &: \begin{bmatrix} 3 & 4 \end{bmatrix} \\ \mathbf{C} &: \begin{bmatrix} \] \end{bmatrix} \end{aligned} \quad (4-20)$$

The matrix given by (4-21) illustrate the fixed and varying elements for both the local LTI models \mathbf{Q} and the unknown matrices \mathbf{P} . The asterisk sign indicates a varying entry.

$$\mathbf{Q} = \mathbf{P} = \left[\begin{array}{cccc|c} 0 & 0 & 1 & 0 & 0 \\ 0 & 0 & 0 & 1 & 0 \\ 0 & 0 & 0 & 0 & * \\ 0 & * & 0 & * & * \\ \hline 1 & -1 & 0 & 0 & 0 \end{array} \right] \quad (4-21)$$

The next step is to construct a PDSS model. This is done by interpolating the varying elements in 4-21. Recall from section 3-4 that only four samples are generated ($N = 4$). This means according to equation (4-13) and (4-4) that the least squares problem will be underdetermined for $mo > 3$. The structure of the PDSS model is described in section 4-1 and the approach to determine the unknown matrices \mathbf{P}_j is described in section 4-3. Table 4-1 gives an indication about how accurate the obtained PDSS models are for different mo values. Notice that according to this table, the best PDSS models are obtained for a maximum polynomial order mo of three or more. An higher order than three is not better on all indicators. Therefore, in this showcase example, a PDSS model with an order of three will be used. Figure 4-2 illustrates the behaviour of the elements in the \mathbf{A} matrix for the 'true' local

LTI models and the 'approximated' PDSS model. A grid of $N_v = 500$ equally distributed points is used for this. Figure 4-3 does the same thing for the \mathbf{B} matrix. The plots in figure 4-4 illustrate how the error between the true system and the PDSS model behaves with respect to frequency and the chosen mass, respectively. Note that the left plot in figure 4-4 shows some non-smooth behaviour. This is a direct result of the limited amount of computed local LTI models. As N_v increases, the left plot in figure 4-4 becomes more smooth and the values for E_{tot} start to converge. The effect of N_v and M on the value of E_{tot} is shown in figure 4-5 for a PDSS model with a maximum polynomial order of three ($mo = 3$). Notice that for a fixed N_v , the influence of the M is relative small with respect to the E_{tot} . The right plot in figure shows the Vinnicombe gap metric δ_v as function of the mass m which is used to obtain the models $G_{true}(s)$ and $G_{pdss}(s)$. Moreover, it shows that error between the true model and the PDSS model is relatively large for low m values ($m < 0.5$ [kg]) and becomes less for high m values ($m > 0.5$ [kg]). Finally, the left plot in figure 4-6 shows the first eigenfrequency as function of the mass for the local LTI models (i.e. 'true system' see also figure 2-4) and for the PDSS model. Notice that the maximum eigenfrequency for the PDSS model is almost the same as for the local LTI models. The right plot in figure 4-6 shows the magnitude of the resonance peak as function of the eigenfrequency. In the context of this MSc thesis, a change in this magnitude could influence the outcome of the optimal design variables \mathbf{x}_d . However, the right plot in figure 4-6 indicates that the magnitude of the resonance peak for both the PDSS model and true system are almost equal.

<i>indicator</i>	<i>maximum polynomial order mo</i>				
	<i>1</i>	<i>2</i>	<i>3</i>	<i>4</i>	<i>5</i>
r_2	$9.86 \cdot 10^2$	$2.56 \cdot 10^2$	$1.72 \cdot 10^{-10}$	$2.05 \cdot 10^{-10}$	$7.78 \cdot 10^{-10}$
E_{tot}	8.04	3.18	1.71	2.06	0.96
$E_{\nu_{g\infty}}$	0.27	0.27	0.22	0.22	0.19
$E_{\nu_{g2}}$	0.09	0.05	0.02	0.02	0.04

Table 4-1: Accuracy of the PDSS model measured by the indicators 4-16, 4-17, 4-18 and 4-19. These indicators are generated using a dense grid of 500 points equally distributed points between \underline{m} and \bar{m} . Note that the least squares problem is underdetermined for $mo = 4$ and $mo = 5$ (see condition 4-13). Moreover, $\omega_1 = 10$ [rad/s], $\omega_M = 100$ [rad/s], $M = 500$.

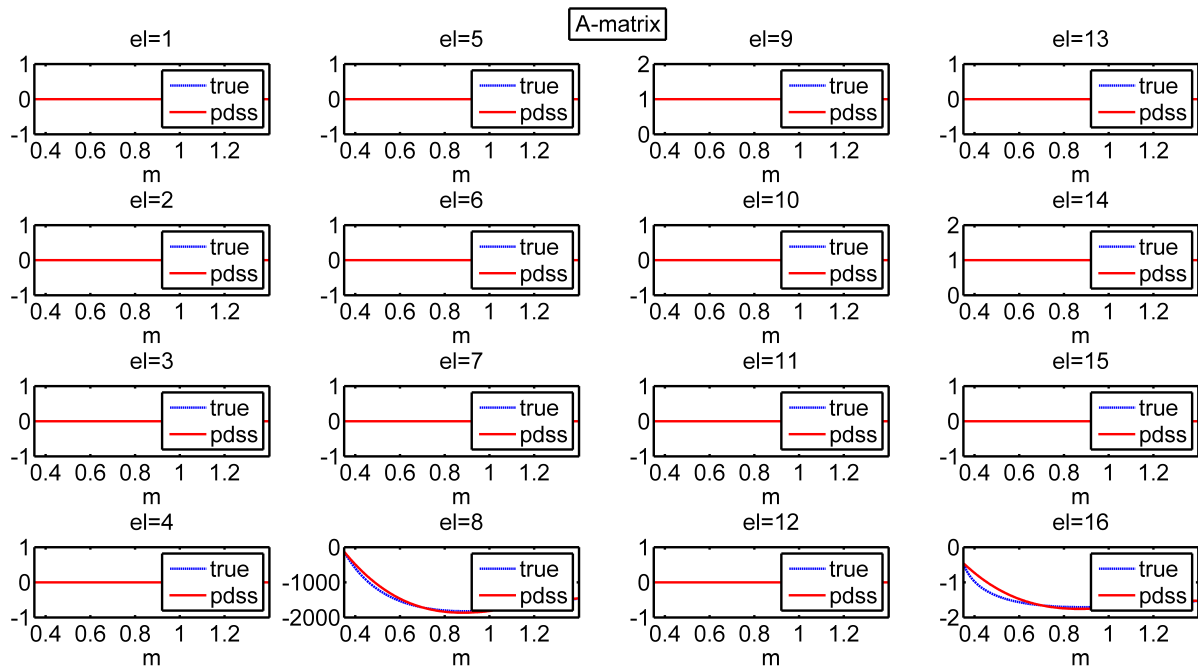


Figure 4-2: Behaviour of state-space elements in the \mathbf{A} matrix with respect to $\mathbf{p} = m$. A grid of 500 equally distributed points between 0.35 [kg] and 1.4 [kg] is used. The PDSS model has a maximum polynomial order of $mo = 3$.

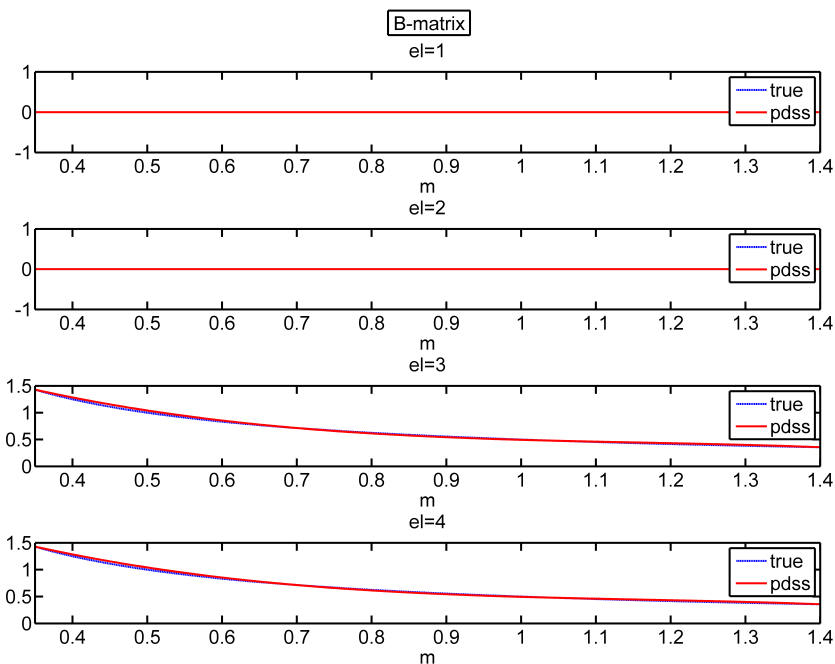


Figure 4-3: Behaviour of state-space elements in the \mathbf{B} matrix with respect to $\mathbf{p} = m$. A grid of 500 equally distributed points between 0.35 [kg] and 1.4 [kg] is used. The PDSS model has a maximum polynomial order of $mo = 3$.

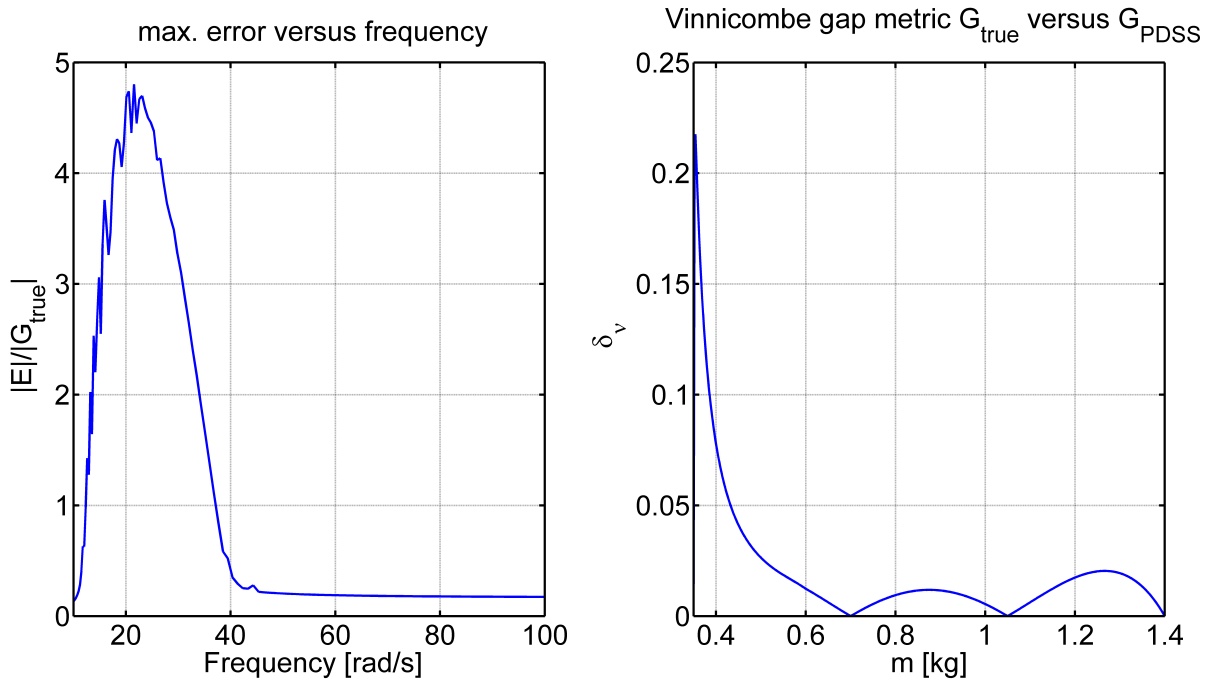


Figure 4-4: Plot of the term $\left(\frac{E(j\omega)}{G_{\text{true}}(j\omega)}\right)$ versus frequency ω . Moreover, $\omega_1 = 10$ [rad/s], $\omega_M = 100$ [rad/s], $M = 100$ and $m_0 = 3$ (left plot). Plot of the Vinnicombe metric δ versus the mass m (right plot).

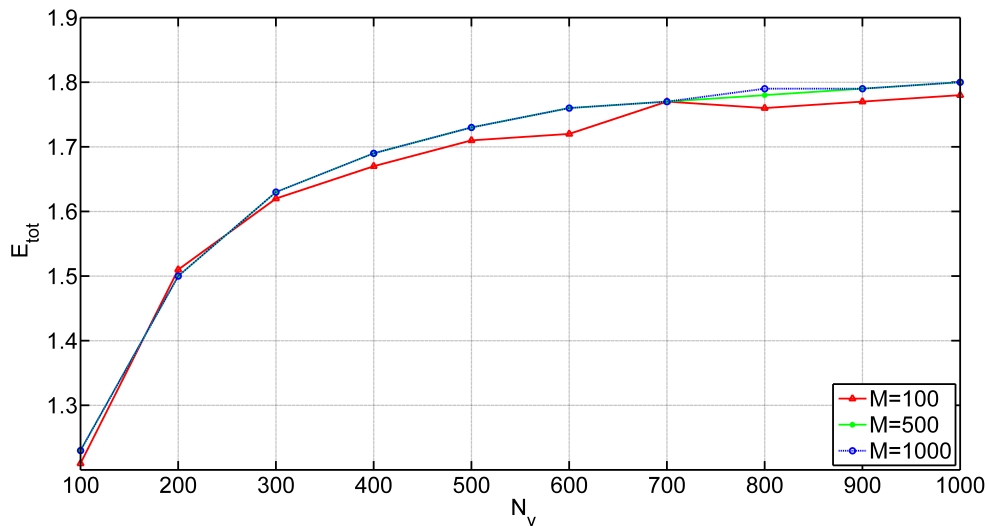


Figure 4-5: Plot which shows the effect of different M and N_v values on the indicator E_{tot} . Note that the PDSS model has a maximum polynomial order of three ($m_0 = 3$).

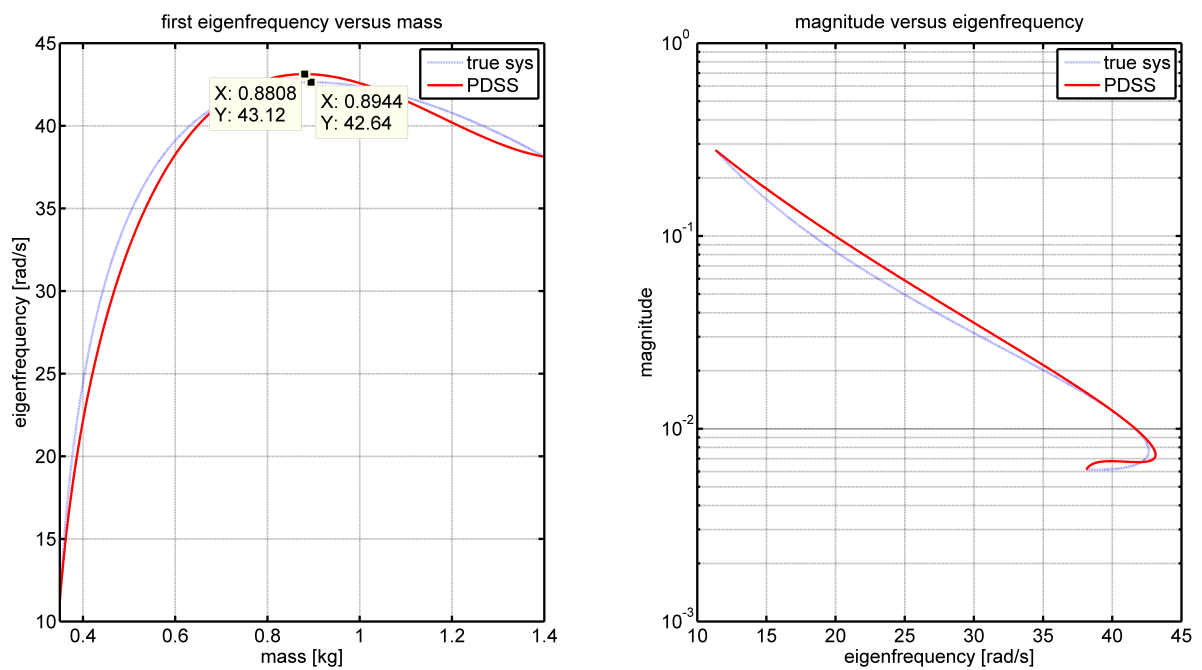


Figure 4-6: Plot of first resonance frequency of the double mass-spring-damper system with respect to the mass (left plot). Plot of the magnitude of the resonance frequency with respect to the eigenfrequency (right plot).

Controller-structure optimization (CSO)

Recall from section 2-5 that the objective of this MSc thesis is to maximize the bandwidth ω_b and to minimize the mass m of a controlled structure. This goal was mathematically formulated by an objective function (equation (2-4)) with a constraint on the sensitivity function S (equation (2-7)). Note that the words 'objective' and 'constraint' in the context of this chapter refer to these two equations. The first section of this chapter gives arguments why this type of optimization criteria are chosen. Section 5-2 presents an integrated optimization approach for finding the solution of a CSO problem. Section 5-3 presents a nested optimization approach for the same purpose. Finally, in section 5-4, these two approaches are applied to the showcase example that was introduced earlier in section 2-6.

5-1 Optimization criteria

The literature survey from van der Marel [2014] showed that an optimization problem can be specified in multiple domains, like the frequency domain, space domain, time domain etc. One of the goals of this MSc thesis is to minimize the amount of domains in the optimization criteria for solving a CSO problem. The reason for this is because objectives and/or constraints which are defined in different domains typically lead to a more complex problem. Solving this problem could result in time-consuming (co-)simulations. Moreover, it is easier to verify optimization results of a simple problem than for a complex problem.

The two main objectives in this MSc thesis, maximizing the bandwidth ω_b and minimizing the mass m , are related to the frequency and the space domain, respectively. However, it turned out to be hard to reduce the amount of domains to one. The reason for this is because it is difficult to extract the mass of a structure from only frequency domain information (e.g. state-space matrices, bode plots etc.). Still this property cannot be neglected because it is an

important objective from mechanical point of view. Fortunately, due to the proposed design approach in chapter 2, it is not too difficult to extract the mass of a structure because it is fully parameterized and described by a PDSS model. Therefore, the property mass m is clearly visible in the optimization criteria.

The second part of the optimization criteria is based on the transfer function between the reference signal r and the error signal e , also referred to as *sensitivity function* S . Skogestad and Postlethwaite [2005] showed that the sensitivity function is a very good indicator of closed-loop performance for both SISO and MIMO system. This property is for example used in \mathcal{H}_∞ (mixed) sensitivity controller design. In order to explain this briefly, let's start with a one degree of freedom feedback control structure (see figure 5-1). From the block diagram in

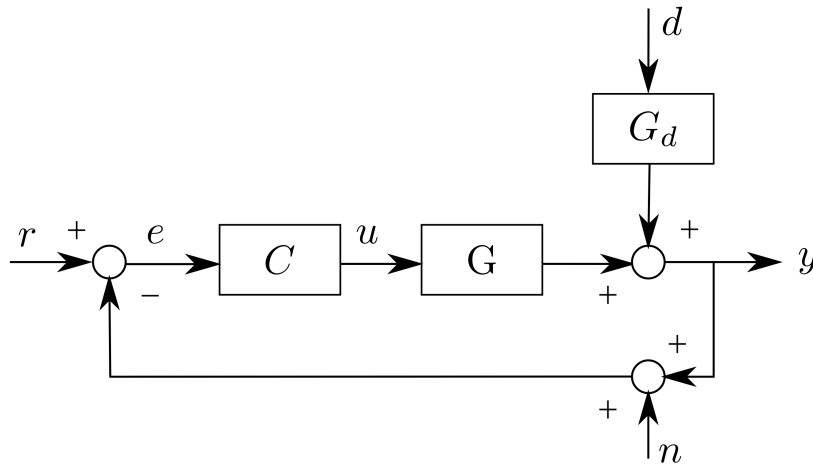


Figure 5-1: Figure copied from Skogestad and Postlethwaite [2005]. Block diagram of a one degree of freedom feedback control system where u is the input signal into the plant $G(s)$, d is the disturbance signal, e represents the error between the desired reference signal r and the measured output with noise y_m . The controller is indicated by the letter C .

figure 5-1 it is possible to derive the closed-loop response:

$$y = \underbrace{(I + GC)^{-1}GC}_{T} r + \underbrace{(I + GC)^{-1}G_d}_{S} d - \underbrace{(I + GC)^{-1}GC}_{T} n \quad (5-1)$$

where G is the *open-loop system*, C is the *controller*, S is the *sensitivity function* and T is the *complementary sensitivity function*. In the control community, different indicators are used to quantify the closed-loop performance and stability. An option would be to use **step response analysis** for characterizing the closed-loop response when there is a step in the reference input. The output can be characterized by its rise time, settling time, overshoot etc. Although these results are very easy to interpret, it considers a small class of signals and is therefore difficult to say something about stability and performance. A second option would be to use **frequency domain analysis**. Recall that in this MSc thesis the sensitivity function S will be used. Figure 5-2 shows how a typical sensitivity function looks like. The maximum peak of S will be defined as:

$$M_S = \|S\|_\infty = \max_{\omega} |S(j\omega)| \quad (5-2)$$

The *gain margin* (GM) and *phase margin* (PM), which are also stability measures, are closely related to M_S . According to Skogestad and Postlethwaite [2005], an $M_S < 2$ implies a $GM > 2$ and $PM > 30^\circ$ for a SISO system. This should provide a reasonable trade-off between performance and stability and will therefore be used as hard requirement in this MSc thesis. To incorporate the specification on the sensitivity function, section 2-5 introduced a

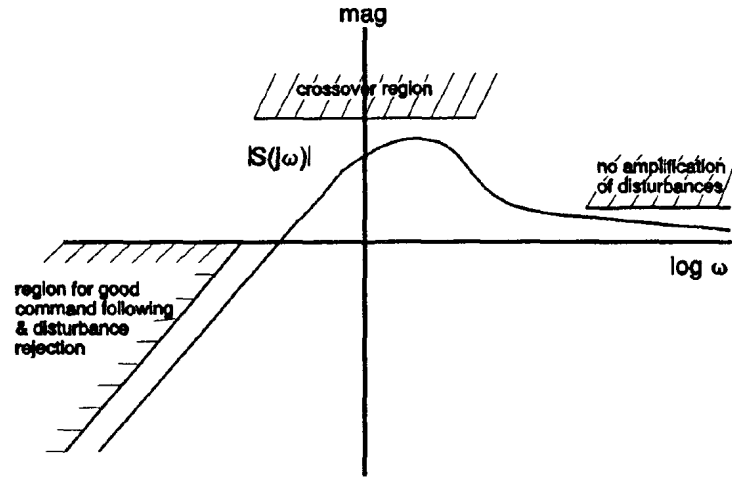


Figure 5-2: Typical sensitivity function (copied from Bibel and Stephen Malyevac [1992]).

weight W_p which will be used to 'shape' the sensitivity function. Recall that this weight W_p is given by equation (2-8). The upper bound on $|S|$ for a SISO system will be equal to the transfer function $\frac{1}{|W_p(s)|}$ which in this case can be written as:

$$\frac{1}{|W_p(s)|} = |A| \frac{\left| \frac{1}{A\omega_b} s + 1 \right|}{\left| \frac{1}{M\omega_b} s + 1 \right|} \quad (5-3)$$

From equation (5-3) it becomes clear that an upper bound of $M_S < 2$ corresponds to $M = 2$. The term A is typically close to zero. Notice that the bandwidth ω_b in the weight W_p is also present in the objective function. In general, maximizing ω_b yields a small rise time which is good in terms of performance. However, one of the side effects of a high bandwidth is that it could result in a system which is sensitive to noise. The following two sections will introduce two possible optimization approaches for solving a CSO problem. First, an integrated approach is presented which uses the MATLAB function `system` for finding the design variables \mathbf{x}_d and ω_b simultaneously. The second approach, nested optimization, maximizes the bandwidth ω_b using a kind of line search method. This typically results in multiple iterations. In each iteration, the design variables \mathbf{x}_d are optimized using the MATLAB function `hinfstruct`.

5-2 Integrated optimization

The literature survey from van der Marel [2014] showed that *evolutionary algorithms* (EA) are often applied for solving multi-objective non-convex CSO problems. Especially in the

field of structural design, many types of EA are available (Kicingier et al. [2005]). However, in the field of optimizing control parameters of fixed-structure controllers, other type of optimization algorithms are also common (e.g. D. Arzelier and Henrion [2011], Apkarian and Noll [2006]). In this MSc thesis, the MATLAB function `syntune` will be used for integral optimization and the MATLAB function `hinfstruct` will be used for a nested optimization approach. One of the reasons for this choice of optimization algorithm is that in context of this thesis, the amount of design variables is rather limited (e.g. 3 - 10) and the objectives and constraints defined earlier in section 2-5 are quite related to control engineering. This can be seen by the sensitivity function S which appears in the constraint $\|W_p S\|_\infty \geq 1$ and the corresponding bandwidth ω_b which is present in the objective function. Moreover, these optimization algorithms make smart use of generalized gradients and bundling techniques for efficiently computing the \mathcal{H}_∞ -norm [Bruinsma and Steinbuch, 1990].

For modelling purposes, the objectives and constraints described earlier in section 2-5 are translated into the block diagram shown by figure 5-3. All the blocks together form a *generalized state-space model* which in this case is denoted by $T0$ (dashed line). This $T0$ model has one input (r) and two outputs (z_1 and z_2). Moreover, it is built from multiple LTI models (e.g. G , C etc.) which includes the tunable design variables \mathbf{x}_d . Notice that the gain of the transfer function from r to z_1 contains information that is needed to verify whether the constraint $\|W_p S\|_\infty \geq 1$ is violated or not. The objective function is modelled by the static transfer function from r to z_2 . Therefore, the gain of this transfer function should be minimized as much as possible.

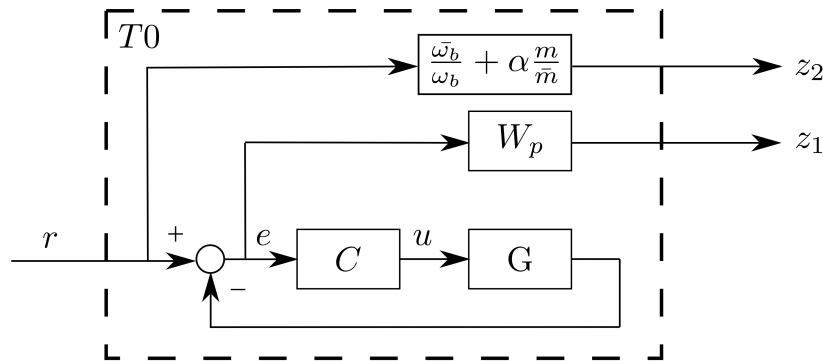


Figure 5-3: Block diagram of a generalized state-space model $T0$ which is used to solve a CSO problem. The gain from r to z_1 must be smaller than one (hard requirement) and the gain from r to z_2 should be minimized (soft requirement).

5-3 Nested optimization

In this section, a nested optimization approach is presented for solving a CSO problem. The results of this approach can later on be compared with the integrated approach from section 5-2 in terms of efficiency and accuracy.

The nested and integrated optimization approach will be quite similar in this MSc thesis because they both use the same type of optimization algorithm for optimizing the design variables \mathbf{x}_d . However, the difference between them is that in case of the nested approach, a kind of *line search* is used in order to maximize ω_b . In this case, the bandwidth ω_b will be held fixed while the design variables \mathbf{x}_d are optimized. If the constraint $\|W_p S\|_\infty < 1$ is not violated, ω_b will be increased and the initial conditions for \mathbf{x}_d are updated with respect to the optimization results. This procedure will continue until the change in ω_b becomes too small. In case of the integrated approach, the objective of maximizing ω_b is already present in the transfer function from r to z_2 (see figure 5-3). Moreover, Papalambros and Wilde [2000] indicated that a general local exploration procedure typically has two phases, a direction-finding phase and a line search along this direction. However, in this nested optimization approach, gradient information will not be computed in order to determine optimal directions and step sizes. Instead, the initial step size $s(0)$ will be iteratively reduced by a factor λ .

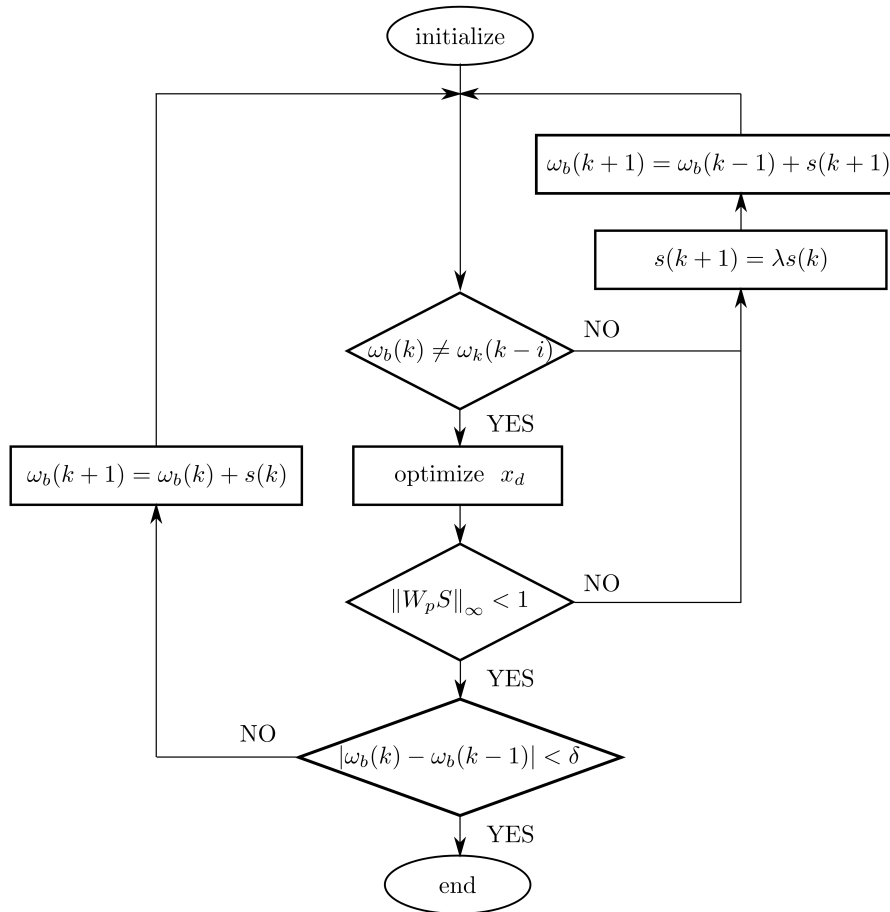


Figure 5-4: Flow diagram of nested optimization approach.

The flow diagram in figure 5-4 shows how this nested optimization approach exactly works. First, initial values for the design variables \mathbf{x}_d , a relatively large step $s(0)$ and a relatively low bandwidth $\omega_b(0)$ need to be prescribed. The initial bandwidth $\omega_b(0)$ should be low such that it should be easy to find a feasible solution. Second, a quick check is done whether the

active bandwidth $\omega_b(k)$ has not yet been examined in previous iterations. This is mathematically described by $\omega_b(k) \neq \omega_k(k - i)$ where the letter k represents the iteration number and $i \in \{1 \dots k - 1\}$. Third, the design variables \mathbf{x}_d are optimized by the MATLAB function `hinfstruct`. The scheme which is used for this purpose is the same as in figure 5-3 only without the transfer function from r to z_2 . Fourth, a check is done whether the constraint $\|W_p S\|_\infty < 1$ is violated or not. If this is not the case, then the new bandwidth $\omega_b(k + 1)$ is equal to the current bandwidth $\omega_b(k)$ plus the step $s(k)$. However, if $\|W_p S\|_\infty \geq 1$, a new step $s(k + 1)$ is calculated by taking the current step $s(k)$ and reducing it by a constant factor λ . The new bandwidth $\omega_b(k + 1)$ is equal to the previous bandwidth $\omega_b(k - 1)$ plus $s(k + 1)$. This process repeats itself until the change in bandwidth becomes less than some predefined threshold value δ .

The initial conditions in this nested approach could influence the amount of iteration that is needed for the algorithm to converge. Especially the selection of the constant parameter λ determines how the step $s(k)$ will be reduced during the nested optimization process. In this thesis, two types of λ values will be examined. The first is $\lambda = 0.5$ which is inspired by the *Dichotomous section method*. The second is:

$$\lambda = \frac{\sqrt{5} - 1}{2} \approx 0.618 \quad (5-4)$$

which is inspired by the *Golden section method*.

5-4 Showcase example: double mass-spring-damper system

The techniques described in this chapter are applied to the showcase example which was earlier introduced in section 2-6. The results of the various optimization methods is shown in table 5-1. Table 5-2 shows the settings that were used to obtain these results. Note that also a manual design of the controlled double mass-spring-damper system is made (see sixth column in table 5-1). This manual design is based on a step response analysis. The main target for the manual design was to create a smooth step response with low overshoot.

	<i>True model</i>	<i>PDSS model</i>	<i>Integrated optimization</i>	$\lambda = 0.5$	$\lambda \approx 0.618$	<i>manual design</i>
m^*	0.8944	0.8808	0.8894	0.8823	0.8786	0.8808
ω_b^*	4.1530	4.2110	4.2109	4.2031	4.2062	≈ 1.3
ω_c^*	9.0586	9.1877	9.1948	9.1881	9.1940	3
K_p^*	42.0825	43.6134	43.9482	43.6356	43.4201	4.3146
iterations	—	—	448	656	1086	—
PM (deg)	42.9	42.8	42.8	42.8	42.8	43.3
GM (dB)	10.8	10.3	10.3	10.3	10.3	17.8

Table 5-1: Table with optimization results. Parameters with an asterisk sign (*) are obtained via an optimization process. The settings for the optimization methods can be found in table 5-2.

The first column in table 5-1, 'True model', is created from the original plant G given by the state-space description in equation (3-15). In this model the mass m is fixed to the 'a priori' known optimum of $m^* = 0.894$ [kg]. The remaining control design variables \mathbf{x}_c are

	<i>True model</i>	<i>PDSS model</i>	<i>Integrated optimization</i>	$\lambda = 0.5$	$\lambda \approx 0.618$
random start	15	15	1	1	1
maximum iterations	1000	1000	100	100	100
δ [rad/s]	0.001	0.001	0.1	0.1	0.1
$\omega_b(0)$ [rad/s]	4.1	4.2	1	1	1
$s(0)$	0.001	0.001	–	5	5

Table 5-2: Settings for the optimization methods described by table 5-1.

determined by a kind of line search similar to the one described in section 5-3. However, in this case a fixed step of $s(k) = 0.001$ is used. Furthermore, the PM and GM of the loop transfer function $L = CG$ are calculated as well. Convergence was reached when the change in ω_b was not more than 0.001 [rad/s]. This procedure is also applied to the PDSS model instead of the 'True model'. In that case the known optimum is $m^* = 0.880$ [kg] and the results are shown by the second column.

Column three in table 5-1 corresponds to the integrated optimization method described in section 5-2. The columns four and five correspond to the nested optimization method described in section 5-3. Figure 5-5 and 5-6 show the intermediate progress of this nested optimization method as function of the iterations k . Notice that the nested optimization method with $\lambda = 0.5$ is more efficient in this showcase example than the one with $\lambda \approx 0.618$. This is probably a direct consequence of the chosen initial conditions (see table 5-2). Still, the numerical solutions in terms of the design variables $\mathbf{x}_d = \{m^*, \omega_b^*, \omega_c^*, K_p^*\}$ of the integrated and nested methods are very similar. If you compare these results with column two, than the integrated and nested optimization with $\lambda \approx 0.618$ are the most accurate ones. In terms of efficiency, the integrated method is by far the best although it remains relative due to the settings of the optimization algorithms.

For now the results of the integrated optimization method described in table 5-1 will be used to define the plant G and the controller C . First, analysis on the sensitivity functions will take place. This will be done based on the plots in figure 5-7. For this purpose, some notations are introduced here:

- $1/|W_p|$ = upper bound on S
- S_{pdss} = sensitivity function constructed from the plant G described by a PDSS model ($mo = 3$) and the controller C
- S_{true} = sensitivity function constructed from the plant G described by the 'true' model (see equation (3-15)) and the controller C
- S_{manual} = sensitivity function created via manual design
- $W_p S_{pdss}$ = transfer function obtained by multiplying the weight W_p with S_{pdss}
- $W_p S_{true}$ = transfer function obtained by multiplying the weight W_p with S_{true}

Figure 5-7 shows that S_{pdss} approximates S_{true} very well. The right plot in figure 5-7 indicates that the obtained parameters from the design approach via integrated optimization (column

three in table 5-1) will violate the constraint $\|W_p S\|_\infty < 1$ (blue line) if they are applied on the true system. Fortunately, this violation is very small. The step and disturbance response in figure 5-8 confirms that the effect on the closed-loop response is small while an approximated model in the form of a PDSS model with a maximum polynomial order of three $mo = 3$ is used instead. Unfortunately, high frequency signals are visible in both the step and disturbance response. This is not the case for the manual design although the bandwidth ω_b is much smaller in this case. The difference between these two designs in terms of their sensitivity function is shown in the left plot in figure 5-7. The maximum peak of S_{manual} is slightly lower than the maximum peak of S_{pdss} and S_{true} . An even more obvious difference is seen at higher frequencies because S_{manual} converges quickly to 0 [dB] while S_{pdss} and S_{true} show a resonance before it converges to 0 [dB]. Recall from figure 5-2 that the effect of a large magnitude at a high frequency in a sensitivity plot could indicate amplification of disturbances.

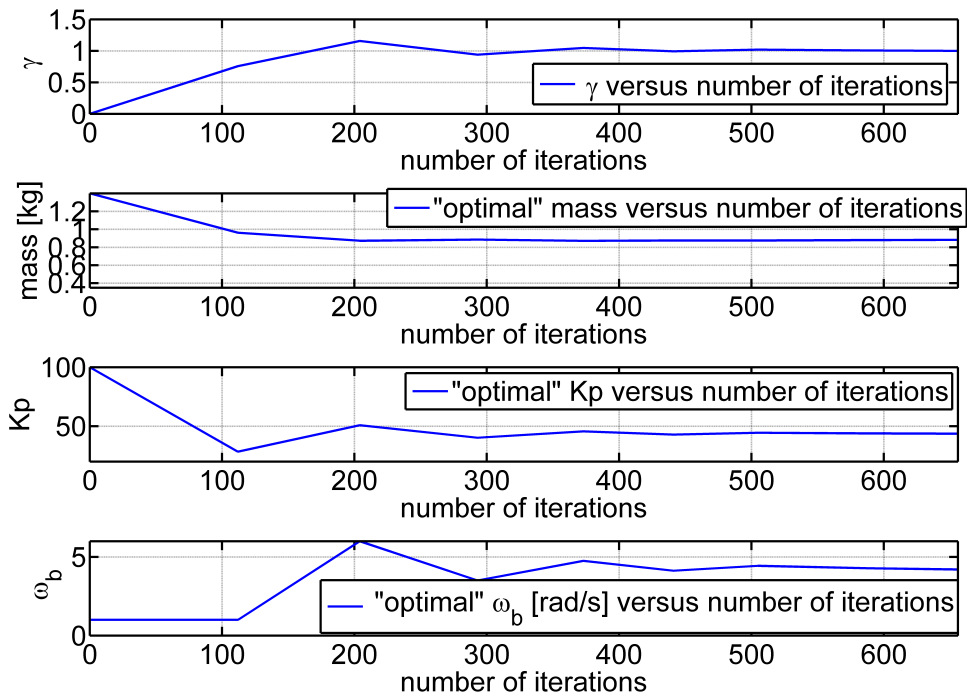


Figure 5-5: Intermediate results of the nested optimization run with $\lambda = 0.5$

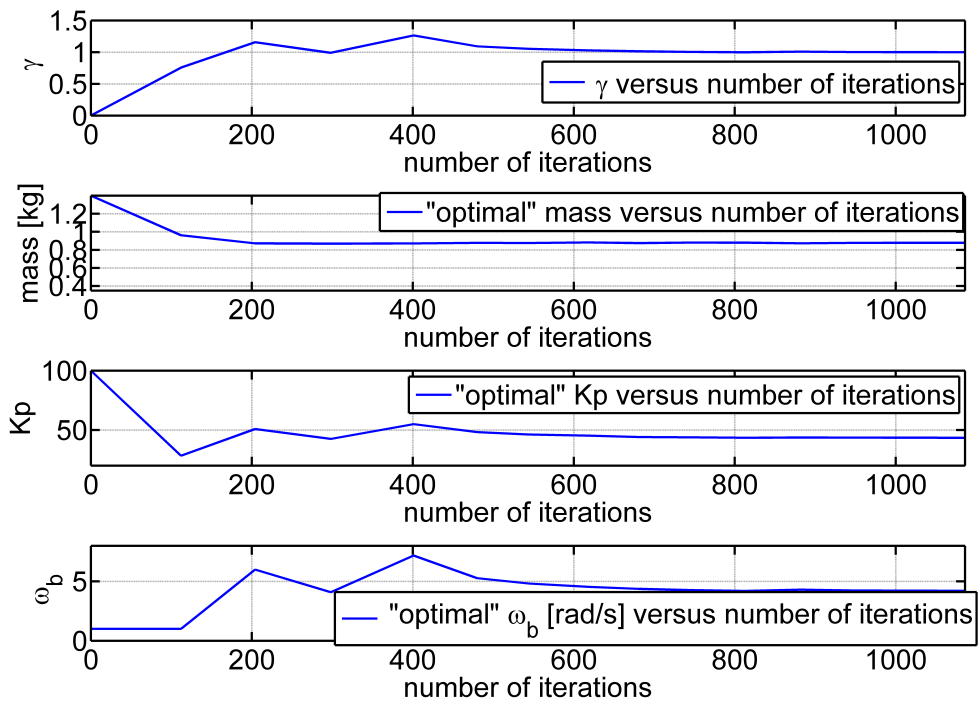


Figure 5-6: Intermediate results of the nested optimization run with $\lambda \approx 0.618$.

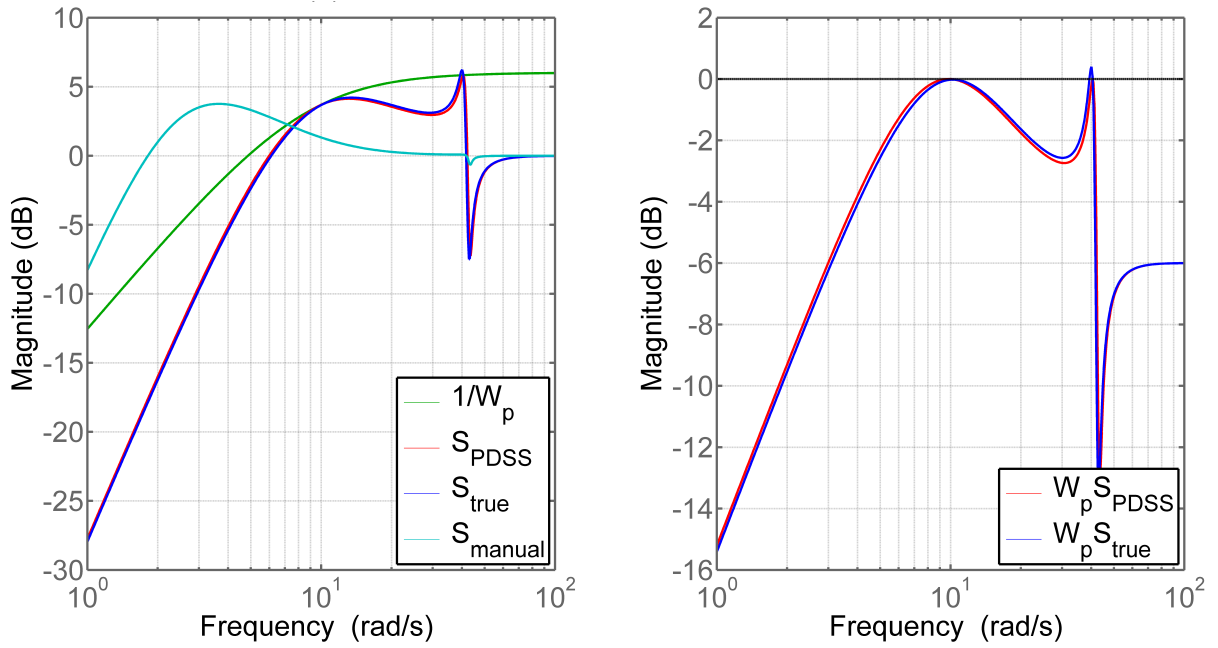


Figure 5-7: Multiple sensitivity functions and the upper bound $1/|W_p|$ in one plot (left plot). Weighted sensitivity functions $|W_p S_{pdss}|$ and $|W_p S_{true}|$. The parameters for the controller C are given in the third column in table 5-1 (right plot).

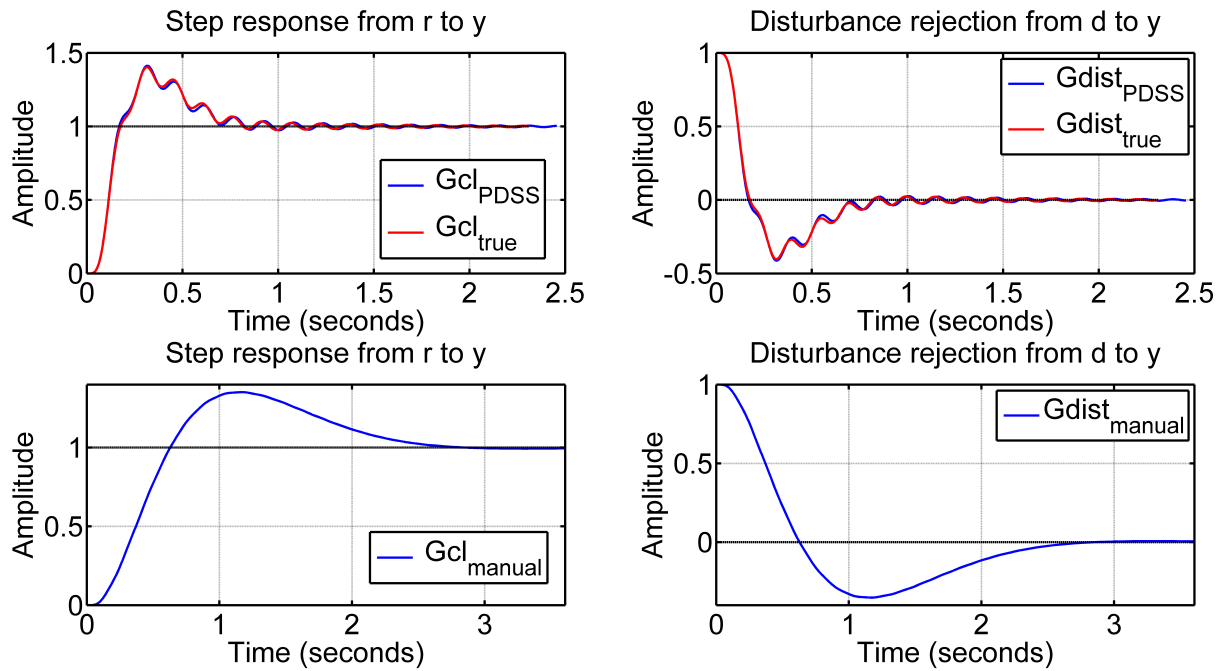


Figure 5-8: Step and disturbance responses of the manual and the integrated design.

CSO for a single-axis motion system

This chapter presents the final case study which will be used to test the design approach presented in chapter 2. First, an introduction about this case study is given in section 6-1. Second, some additional restrictions towards the FE model which is used in this case study are given in section 6-2. Section 6-3 analyses the open-loop dynamics of the controlled-parameterized structure. Some of the techniques that are used here can be found in chapter 3. Section 6-4 applies the methods described in chapter 4 in order to construct a PDSS model of a parameterized structure. This model is then used for optimization purposes which is the subject of section 6-5. The details about these optimization methods can be found in chapter 5. Section 6-6 investigates the effect of a different measurement position on the outcome of the design approach. Finally, some additional information about the phenomenon 'mode switching' is given in section 6-7. This information refers to a closer inspection of the behaviour of a mode switch which occurred during the analysis of the open-loop dynamics of the controlled-parameterized structure.

6-1 Introduction

Figure 6-1 shows the controlled parameterized structure that will be examined in this chapter. This structure is essentially a block with a hole in the middle but it could be a representative of a simplified single-axis motion system. It is modelled in a *two-dimensional (2D) finite element (FE)* environment. More information about the modelling process can be found in appendix A and B. The length of the block L_x is defined by nx nodes and the height L_y is defined by ny nodes. The hole is characterized by the parameters H_x and H_y which refers to the width and height of the hole, respectively. Table 6-1 shows all the constant settings that are used for this parameterized structure. Note that the units H_x and H_y are in percentages [%] of L_x and L_y , respectively. Figure 6-1 also shows a red dot on the left side of the structure and a green dot on the right side. The red dot represents the actuator position and the green dot represents the measurement position. In this chapter, the position of the actuator will

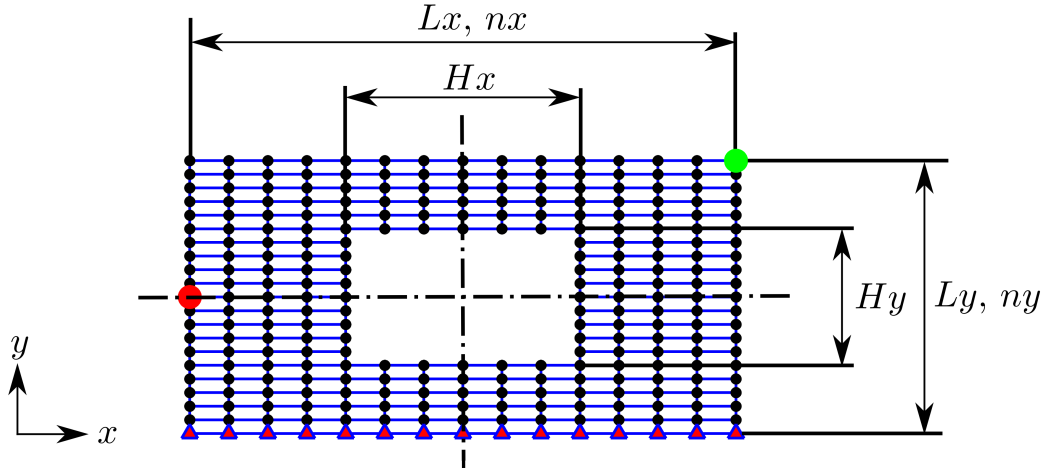


Figure 6-1: FE model of a controlled parameterized structure which represents a simplified single-axis motion system. The red dot represents the actuator position and the green dot represents the measurement position. The triangles indicate nodes that are only allowed to move frictionless in the x -direction.

always be in the middle on the left side of the structure. However, the current position of the measurement (top-right) will be used in the sections 6-1 to 6-5 and 6-7. In section 6-6, a different measurement position is chosen. The red triangles on the bottom of the structure indicate that these nodes are not able to move in the y -direction. Thus in this case, the nodes at the bottom are only allowed to move frictionless in the x -direction.

<i>property</i>	<i>symbol</i>	<i>values</i>	<i>units</i>
width block	L_x	0.6	[m]
height block	L_y	0.3	[m]
depth block	L_z	0.6	[m]
width hole	H_x	50	[%]
height hole	H_y	–	[%]
depth hole	H_z	100	[%]
density	ρ	7000	$[\frac{kg}{m^3}]$
Young's modulus	E	$210 \cdot 10^9$	$[\frac{N}{m^2}]$
Poisson's ratio	ν	0.33	[–]
damping	ζ	0.005	[–]

Table 6-1: Constant settings for the parameterized structures in figure 6-1 and 6-8.

In this case study, the parameter H_y will serve as structural design variable \mathbf{x}_p and as scheduling parameter \mathbf{p} . Since the control design variables are already defined (see section 2-2), the following condition holds for \mathbf{x}_d :

$$\mathbf{x}_d = \begin{cases} \mathbf{x}_p & = \{H_y\} \in \mathbb{R}^{n_p} \\ \mathbf{x}_c & = \{Kp, \omega_c\} \in \mathbb{R}^{n_c} \end{cases} \quad (6-1)$$

The bounds on the values of the design variables \mathbf{x}_d and the bandwidth ω_b are:

$$\begin{aligned} H_y &\in [5, 85] \\ Kp &\in [1 \cdot 10^8, 1 \cdot 10^{10}] \\ \omega_c &\in [2 \cdot 10^3, 5 \cdot 10^3] \\ \omega_b &\in [5 \cdot 10^2, 5 \cdot 10^3] \end{aligned} \quad (6-2)$$

The idea behind this case study is that if H_y is very small (e.g. ≈ 0 [%]), the parameterized structure in figure 6-1 becomes a solid block. In that case, the mass of the structure will be relatively high but it will most likely be very stiff as well. However, if the size of the hole H_y is very large (e.g. ≈ 100 [%]), the parameterized structure begins to look like a double mass-spring-damper system. In that case the mass of the structure will be relatively low and stiffness of will probably be lower than that of the solid block. One of the questions that arises is:

Does there exist a set of parameters \mathbf{x}_d^* for the optimization problem described earlier in section 2-5 with $\alpha = 0$ which results in a unique non-trivial solution ?

In other words, does there exist something like a unique non-trivial hole size H_y in this case. Note that the objective of minimizing the mass m of the structure is neglected. Another objective is to investigate the effect of α on the optimal mass m^* of the structure and to check if the integrated optimization approach described in section 5-2 is able to find this optimum.

6-2 Restrictions of parameterized structure

Recall from the previous section that the controlled parameterized structure is built in a 2D FE environment and that more information about the FE modelling can be found in appendix A and B. An FE model is obtained by discretizing a mathematical model and will therefore always have some error with respect to reality (see Cook et al. [2002]). Appendix B already introduced several assumptions based on the bilinear Q4 rectangle which is used in this MSc thesis:

1. deformations must be small
2. rotations must be small
3. material is homogeneous, linear and elastic

Still, for the controlled-structure in figure 6-1 choices with respect to the numerical values of nx and ny have to be made. Moreover, due to the fact that the structure is built from finite elements, restrictions with respect to nx , ny and the resolution (rs) of H_y need to be introduced. This is needed in order to avoid non-symmetry in the structure or specifications on the hole size which cannot be realised due to a too coarse grid.

The first requirement, symmetry in the structure, can be achieved by restricting nx and ny to odd values. Note that this implies an even number of elements in the x -direction (nx_{el}) and y -direction (ny_{el}). Due to this restriction it should always be possible to place the actuator and measurement position exactly in the middle with respect to the y -direction. A second requirement can be made with respect to the minimum value of ny . To see this, let's assume that there exists a minimum resolution rs in percentage for the hole size H_y . Notice that there is a relation between the number of elements in y -direction ny_{el} and the amount of possible holes n_h that can be defined:

$$\begin{aligned}
 2 \text{ elements} &\rightarrow 2 \text{ holes (0 [\%], 100 [\%])} \\
 4 \text{ elements} &\rightarrow 3 \text{ holes (0 [\%], 50 [\%], 100 [\%])} \\
 6 \text{ elements} &\rightarrow 4 \text{ holes (0 [\%], 33.3 [\%], 66.6 [\%], 100 [\%])} \\
 8 \text{ elements} &\rightarrow 5 \text{ holes (0 [\%], 25 [\%], 50 [\%], 75 [\%], 100 [\%])} \\
 \vdots &\rightarrow \vdots
 \end{aligned} \tag{6-3}$$

This sequence can be described by the following equations:

$$ny_{el} = 2(n_h - 1) \tag{6-4}$$

$$ny = ny_{el} + 1 \tag{6-5}$$

$$rs = \frac{100}{n_h - 1} \tag{6-6}$$

In this case study it is desirable to be able to specify the scheduling parameter H_y with a resolution of $rs = 0.5$ [%]. According to equation (6-6), the minimum amount of holes n_h should be 201. Substitution of n_y into equation (6-4) gives the minimum amount of elements ny_{el} in y -direction, namely 400 in this case. The minimum number of nodes in the y -direction is then 401. The only remaining uncertainty is the number of nodes in the x -direction nx . Although the focus in this MSc thesis is on the effect of H_y , an extreme low value for nx could cause *discretization errors*. However, making nx equal to ny might be a bit exaggerated. Therefore, the number of nodes in the x -direction nx will be equal to 201.

6-3 Dynamic behaviour of the parameterized structure

Section 6-1 and appendix A, B and D explained how to obtain a reduced-order modal state-space model of the parameterized FE model in figure 6-1. The modes of this structure form the basis for the system matrices **A**, **B**, **C** (see equation (3-6)). Note that if there were no restrictions on the DOFs of the structure, the total amount of available modes would be equal to nx times ny times two, which in this case is equal to 161202 available (eigen)modes. This would for example mean that the system matrix **A** has a size of 322404×322404 . Such a large system matrix will not be used because for controller synthesis only the first few eigenmodes are of importance. Therefore, the 'true system' dynamics in this case study refers to a modal state-space model which is constructed from eight modes. Figure 6-5 illustrates the first eight modes of the parameterized structure with $H_y = 5$ [%]. The modes are ordered according to increasing eigenfrequency ω_r . Notice that the first mode describes a *rigid body motion* while the other seven modes describe the flexibility of the structure. Therefore, the modes two to eight will be referred to as *flexible modes*.

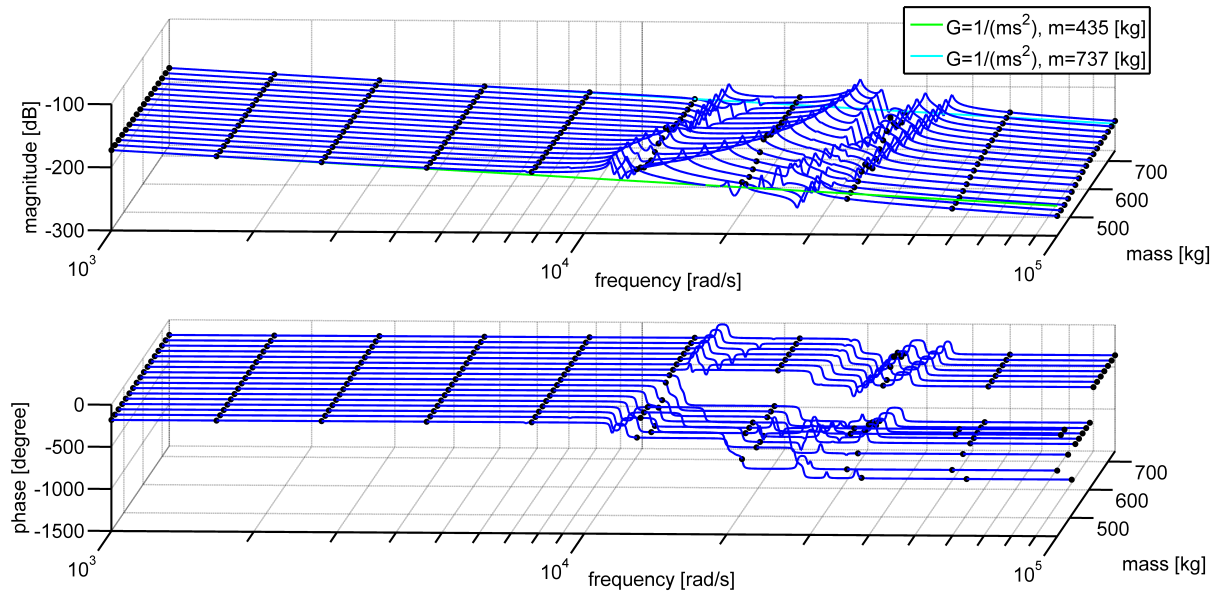


Figure 6-2: 3D plot of multiple open-loop bode diagrams of the parameterized structure shown in figure 6-1 for different hole sizes H_y . Each bode diagram is constructed from eight modes of the original FE model. The green and cyan lines correspond to the transfer function of a lumped mass system.

Another way to visualize a part of the dynamics of the controlled parameterized structure in figure 6-1 is to draw bode diagrams. In this case, a bode diagram shows the horizontal displacement and phase of the measurement position as function of a sinusoidal input signal $F(t)$ on the actuator. Since there are different values of the hole size H_y possible, multiple bode diagrams can be drawn. This is shown in figure 6-2. The resonance peaks that are visible in this three dimensional plot correspond to the modes of the structure. Notice that the position of these peaks, which is related to the eigenfrequency ω_r , vary as function of H_y . This behaviour could influence the closed-loop performance in terms of bandwidth ω_b . In order to be more precise about the behaviour of the eigenmodes and eigenfrequencies, figure 6-3 illustrates the first three eigenfrequencies as function of H_y . Notice in particular that some modes are interchanging with each other at certain frequencies. This happens at hole sizes H_y :

- $H_y = 27 [\%] \rightarrow 28 [\%]$ ($m \approx 654 [kg] \rightarrow 650 [kg]$) mode 4 \leftrightarrow mode 5
- $H_y = 35 [\%] \rightarrow 36 [\%]$ ($m \approx 624 [kg] \rightarrow 620 [kg]$) mode 2 \leftrightarrow mode 3
- $H_y = 70 [\%] \rightarrow 71 [\%]$ ($m \approx 491 [kg] \rightarrow 488 [kg]$) mode 3 \leftrightarrow mode 2

This phenomenon will be associated with the name 'mode switching'. The graphs shown in figure 6-3 are created by computing the eigenmodes and eigenfrequencies of the parameterized structure for every integer H_y value within the range of 5 [%] ($m \approx 737 [kg]$) and 85 [%] ($m \approx 435 [kg]$). The next step is to apply the techniques earlier described in section 3-3

in order to distinguish the different modeshapes. Moreover, the DOFs of the outer shape of the first six modes shown in figure 6-5 are used as reference shapes Φ_{ch0} . Unfortunately, the amount of visible modeshapes in figure 6-3 and the number of reference modeshapes Φ_{ch0} are limited because it was difficult to order multiple modes in the range of H_y values in practice. Here, the underlying problem was that the modeshapes changed as function of H_y . Figure 6-4 shows this effect for mode two. Notice that it is probably not feasible to obtain the outer shape of the structure with $H_y = 85$ [%] (see bottom-right plot in figure 6-4) by scaling the outer shape of the structure with $H_y = 5$ [%] (see top-left plot in figure 6-4). Nevertheless, by reducing the amount of reference modes to six and reducing the number of modes which are used to construct the modal state-space model to four, the technique given in section 3-3 with equation 3-12 was able to order the different modes in a proper manner.

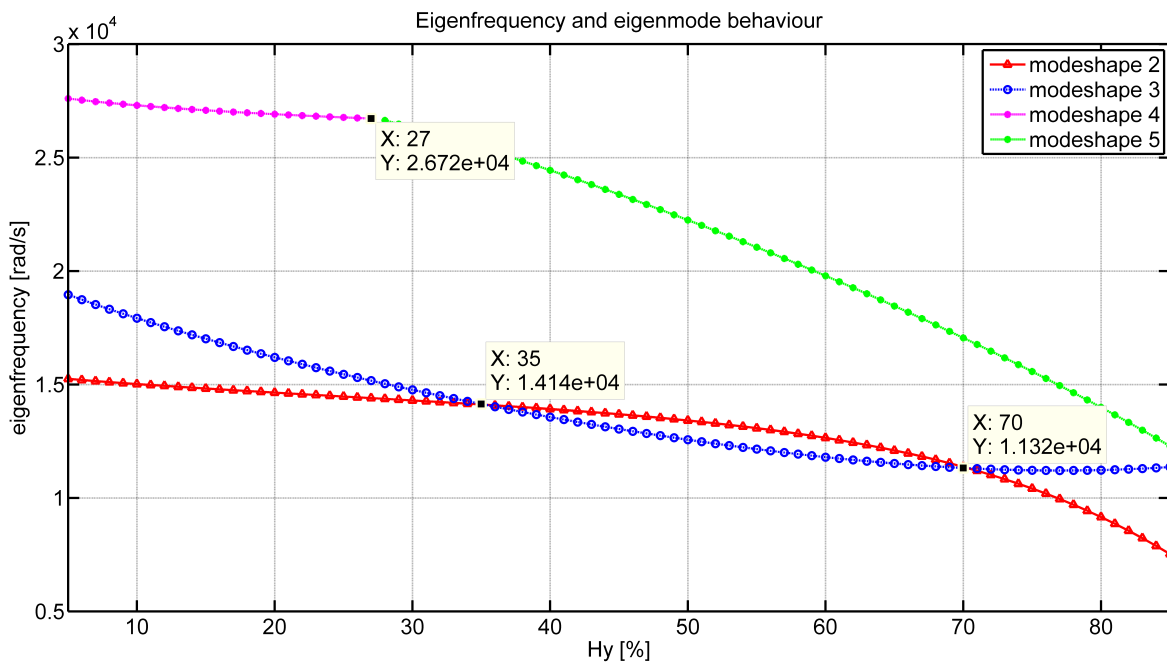


Figure 6-3: Behaviour of the modes as function H_y . Notice that mode switching occurs at the positions where the lines cross each other.

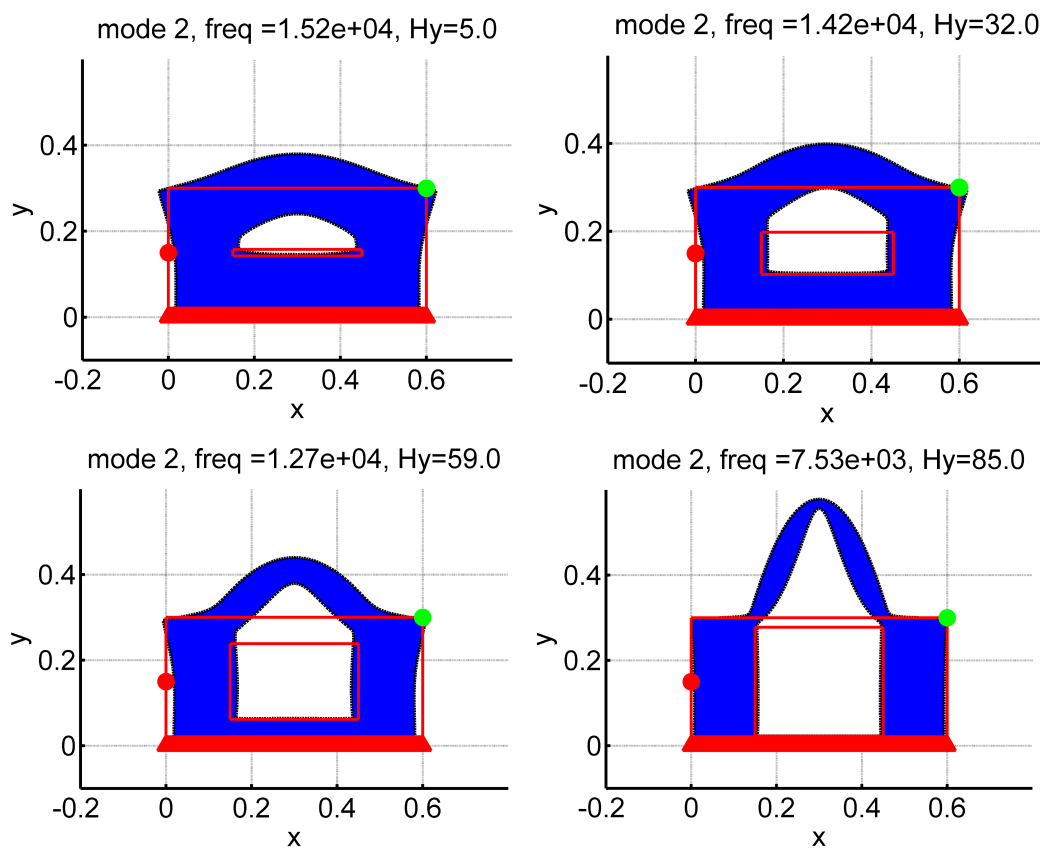


Figure 6-4: Four plots of mode two for the hole sizes $H_y = 5$ [%], $H_y = 32$ [%], $H_y = 59$ [%] and $H_y = 85$ [%]. Notice the change of the modeshape of mode two as H_y increases. The red lines in each plot indicate the shape of the original structure.

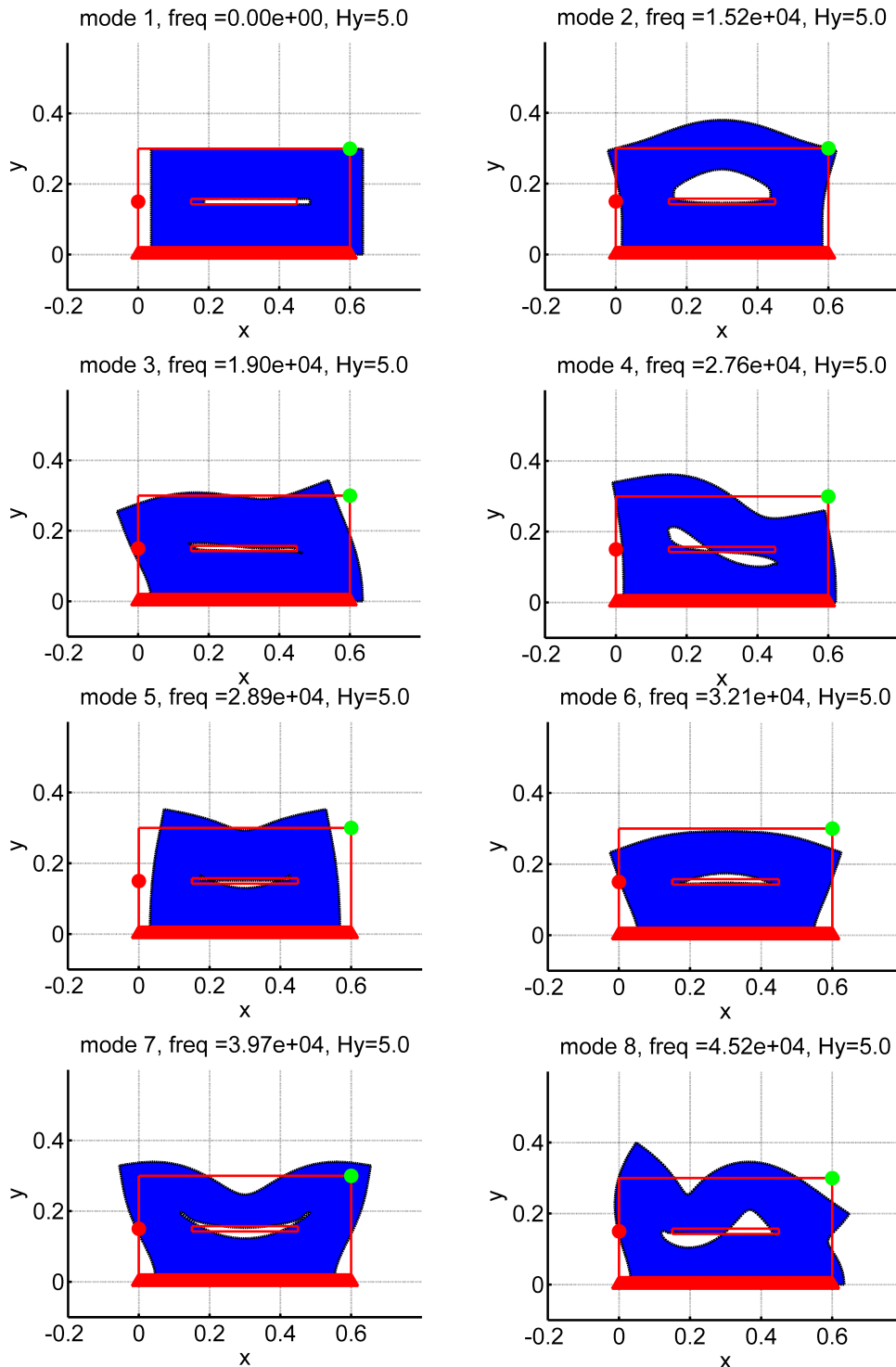


Figure 6-5: First eight modes of the parameterized structure. The hole size is $H_y = 5$ [%] and the outer shape of these modes are also used as reference modeshapes ϕ_{ch0} . The term 'freq' displayed in the title of each plot refers to the eigenfrequencies ω_r of the modes in [rad/s]. The red lines in each plot indicate the shape of the original structure.

6-4 Constructing a PDSS model

In the context of the proposed design approach, four samples at equally spaced distances are used for deriving a PDSS model:

1. $H_y = 5$ [%] ($m \approx 737$ [kg])
2. $H_y = 32$ [%] ($m \approx 635$ [kg])
3. $H_y = 59$ [%] ($m \approx 533$ [kg])
4. $H_y = 85$ [%] ($m \approx 435$ [kg])

In this case study the hole size H_y may vary between 5 [%] and 85 [%]. For each sample, a modal state-space model is constructed (see chapter 3) by taking four modes of the original FE model of the structure in figure 6-1. These modal state-space models can be written as an augmented matrix \mathbf{Q}_k (see section 4-2). The next step is to investigate whether there are entries in \mathbf{Q}_k that vary as function of the scheduling parameter \mathbf{p} . This is done by executing the MATLAB functions `prean_statistics_el.m` and `autofixel.m`. The fixed and varying elements for both the local LTI models \mathbf{Q}_k and the unknown matrices \mathbf{P}_j (see section 4-1) are given by the augmented matrix in 6-7. The asterisk sign indicates a varying entry. As suspected, the matrix \mathbf{Q} shows the same structure as that of a modal state-space model (see equation (3-4)).

$$\mathbf{Q} = \mathbf{P} = \left[\begin{array}{cccccccc|c} 0 & 0 & 0 & 0 & 1 & 0 & 0 & 0 & 0 \\ 0 & 0 & 0 & 0 & 0 & 1 & 0 & 0 & 0 \\ 0 & 0 & 0 & 0 & 0 & 0 & 1 & 0 & 0 \\ 0 & 0 & 0 & 0 & 0 & 0 & 0 & 1 & 0 \\ 0 & 0 & 0 & 0 & 0 & 0 & 0 & 0 & * \\ 0 & * & 0 & 0 & 0 & * & 0 & 0 & * \\ 0 & 0 & * & 0 & 0 & 0 & * & 0 & * \\ 0 & 0 & 0 & * & 0 & 0 & 0 & * & * \\ \hline * & * & * & * & 0 & 0 & 0 & 0 & 0 \end{array} \right] \quad (6-7)$$

Finally, an approximative model of the controlled-parameterized structure in the form of a PDSS model is derived by solving a least-squares problem (section 4-3). The accuracy of the PDSS models is shown by table 6-2 and table 6-3. The indicators that are used in these tables are based on a validation grid of 81 equally distributed points between $H_y = 5$ [%] and $H_y = 85$ [%] of the 'true system' (section 4-4). Note that table 6-2 is obtained from a PDSS model where the collection of eigenmodes $\tilde{\mathbf{V}}$ and eigenfrequencies $\tilde{\mathbf{U}}$ of each local LTI model is ordered according to increasing eigenfrequencies ω_r . In contrast to these validation results, table 6-3 uses a PDSS model where the collection of eigenmodes $\tilde{\mathbf{V}}$ and eigenfrequencies $\tilde{\mathbf{U}}$ of each local LTI models is ordered according to their modeshapes. Notice that both tables indicate that there is a significant improvement in terms of accuracy when the polynomial order mo of the PDSS system increases from two to three. Furthermore, according to both

tables, ordering modes in $\tilde{\mathbf{V}}$ has effect on the accuracy of the PDSS model. Especially the values for the indicator E_{tot} in these tables show quite some difference and indicate that the PDSS model where the modes are ordered according to their modeshapes (table 6-3) is better in terms of accuracy than the PDSS model where the modes are ordered according to their eigenfrequencies (table 6-2). Therefore, in the remainder of this chapter, only PDSS models where the collection of eigenmodes $\tilde{\mathbf{V}}$ and eigenfrequencies $\tilde{\mathbf{U}}$ are ordered according to their modeshape will be used. The next step is to choose a proper polynomial order mo based on the results in table 6-3. In this case study, an order of $mo = 3$ is chosen because it shows a significant increase in accuracy with respect to $mo = 2$ and the underlying least-squares problem is not underdetermined. Moreover, the orders $mo = 4$ and $mo = 5$ do not explicitly indicate better conditioned PDSS models for all indicators.

<i>indicator</i>	<i>maximum polynomial order mo</i>				
	<i>1</i>	<i>2</i>	<i>3</i>	<i>4</i>	<i>5</i>
r_2	$1.17 \cdot 10^8$	$4.74 \cdot 10^7$	$3.94 \cdot 10^{-6}$	$5.41 \cdot 10^{-6}$	$2.30 \cdot 10^{-5}$
E_{tot}	5.74	5.20	3.86	3.77	3.37
$E_{\nu_{g\infty}}$	$1.46 \cdot 10^{-2}$	$2.08 \cdot 10^{-3}$	$4.32 \cdot 10^{-4}$	$9.78 \cdot 10^{-3}$	$1.74 \cdot 10^{-2}$
$E_{\nu_{g2}}$	$8.70 \cdot 10^{-3}$	$1.21 \cdot 10^{-3}$	$1.70 \cdot 10^{-4}$	$4.59 \cdot 10^{-3}$	$7.34 \cdot 10^{-3}$

Table 6-2: Accuracy of PDSS model measured by the indicators 4-16, 4-17, 4-18 and 4-19. Note that the modes are ordered according to their eigenfrequencies ω_r in this case. Further note that the least squares problem is underdetermined for $mo = 4$ and $mo = 5$ (see condition 4-13). Moreover, $\omega_1 = 5 \cdot 10^3$ [rad/s], $\omega_M = 5 \cdot 10^4$ [rad/s], $M = 500$.

<i>indicator</i>	<i>maximum polynomial order mo</i>				
	<i>1</i>	<i>2</i>	<i>3</i>	<i>4</i>	<i>5</i>
r_2	$1.25 \cdot 10^8$	$4.56 \cdot 10^7$	$3.10 \cdot 10^{-6}$	$4.25 \cdot 10^{-6}$	$2.21 \cdot 10^{-5}$
E_{tot}	4.97	3.41	2.01	2.49	3.16
$E_{\nu_{g\infty}}$	$1.46 \cdot 10^{-2}$	$2.08 \cdot 10^{-3}$	$4.34 \cdot 10^{-4}$	$9.78 \cdot 10^{-3}$	$1.74 \cdot 10^{-2}$
$E_{\nu_{g2}}$	$8.70 \cdot 10^{-3}$	$1.21 \cdot 10^{-3}$	$1.71 \cdot 10^{-4}$	$4.59 \cdot 10^{-3}$	$7.34 \cdot 10^{-3}$

Table 6-3: Accuracy of PDSS model measured by the indicators 4-16, 4-17, 4-18 and 4-19. Note that the modes are ordered according to their modeshapes ϕ_{ch} in this case. Further note that the least squares problem is underdetermined for $mo = 4$ and $mo = 5$ (see condition 4-13). Moreover, $\omega_1 = 5 \cdot 10^3$ [rad/s], $\omega_M = 5 \cdot 10^4$ [rad/s], $M = 500$.

6-5 Results of CSO problem

Recall from the problem statement in chapter 1-2 that one of the objectives is to find Pareto optimality between maximizing bandwidth ω_b and minimizing the mass m . Figure 6-6 shows this relation for the controlled-parameterized structure in figure 6-1. This relationship is obtained by performing a nested optimization for each integer value of H_y within the prescribed bounds. This means that the design variables \mathbf{x}_d are in this case equal to the design variables of the controller, namely $\mathbf{x}_c = \{Kp, \omega_c\}$. Thus for each fixed H_y value, the nested optimization approach described in section 5-3 is applied in order to maximize ω_b and optimize \mathbf{x}_c .

Note that this method uses the MATLAB function `hinfstruct`. The settings that were used for this command are:

- $\lambda = 0.5$
- random start = 35
- maximum number of iterations = 1000
- $\delta = 1$ [rad/s]
- $\omega_b(0) = 600$ [rad/s]
- $s(0) = 200$ [rad/s]

The result of figure 6-6 is quite surprising because it shows a non-trivial optimal solution for the mass of the structure if $\alpha = 0$. According to the PDSS model shown in this figure, the optimal mass of the structure is $m^* \approx 624$ [kg] which corresponds with a hole size of $H_y = 35$ [%]. However, notice that around these optimal values a mode switching takes place (see figure 6-3). Section 6-7 gives more information about what causes this non-trivial solution if $\alpha = 0$. Another interesting result shown by figure 6-6 is the accuracy of the two PDSS models (red and black lines) with respect to the 'true model' model (blue line). The PDSS model which is based on local LTI models where the modes are ordered according to their modeshapes approximates the blue line of the 'true model' much better than the PDSS model which is based on local LTI models where the modes are ordered according to their eigenfrequencies. This result could have been expected because the tables 6-2 and 6-3 showed change in terms of model accuracy between them. One of the reasons that might explain this difference in accuracy has to do with the fact that the **B** and **C** matrix are constructed via $\tilde{\mathbf{V}}$. If $\tilde{\mathbf{V}}$ is not ordered according to their modeshapes, a sudden change in this matrix could indirectly cause an abrupt change in the elements of the **B** and **C**. Since interpolation of matrices prefer smooth behaviour of the elements of these matrices, mode switching could influence the accuracy of the PDSS model.

The next step is to investigate the different optimization methods described in chapter 5 on this case study. If the Pareto optimality curve in figure 6-6 approximates the real curve, the solution for the optimization problem described in section 2-5 can already be determined without using any optimization algorithm. To see this, recall that the objective function given by equation (2-4) is defined as:

$$\min_{\mathbf{x}_d} \frac{\bar{\omega}_b}{\omega_b} + \alpha \frac{m}{\bar{m}} \quad (6-8)$$

Notice that the Pareto curve in figure 6-6 implies a relation between the maximum achievable bandwidth ω_b^* and the corresponding mass m over the entire design space. In this case, the relation f between ω_b^* and m can be written as:

$$\omega_b^* = f(\mathbf{x}_d) = f(m, Kp, \omega_c) \quad (6-9)$$

Since this function is represented by figure 6-6, the objective values of equation (6-8) for a fixed α over the range of mass values can easily be computed. The minimum of these objective

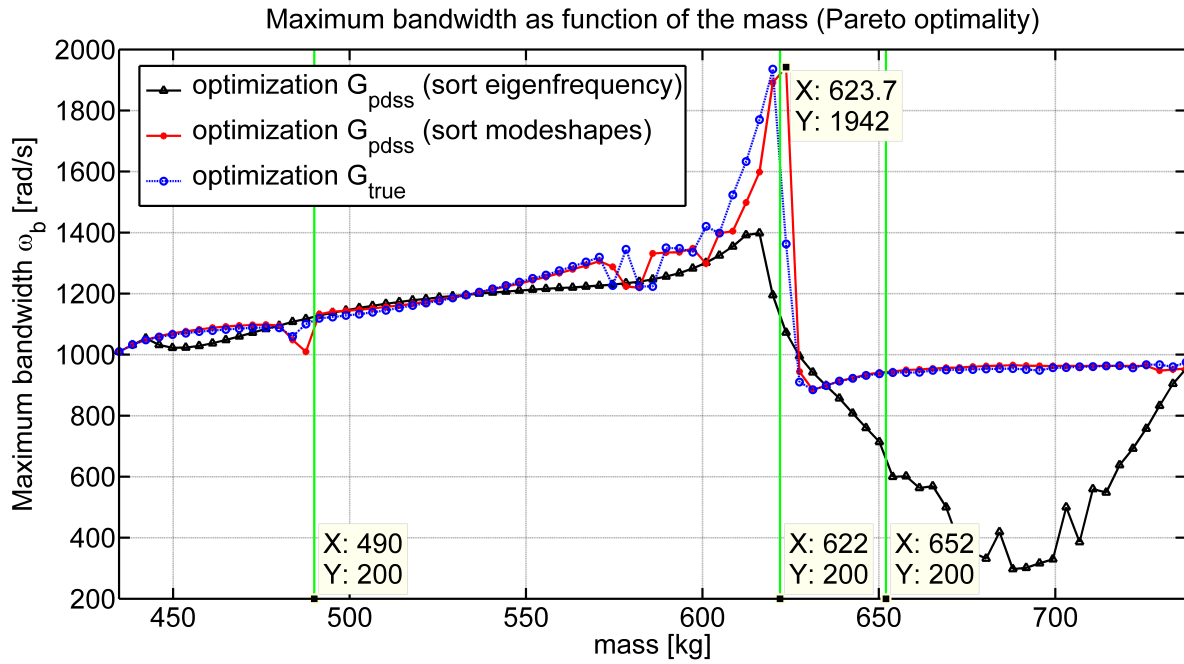


Figure 6-6: Pareto optimality between the objectives bandwidth ω_b and mass m for the controlled parameterized structure in figure 6-1. The vertical green lines indicate a mode switch.

values will correspond to the optimum of the objective function given by equation (6-8). Figure 6-7 shows the relation between a chosen value of α and the optimal mass m^* under the assumption that the Pareto curve in figure 6-6 approximates the true Pareto curve. It is generated by looping over a grid of α values. For each α value, the optimal m^* is determined as just described above. Moreover, figure 6-7 indicates that there are basically two optima, the first corresponds to $m_1^* \approx 623 [kg]$ ($H_y = 35[\%]$) and the second corresponds to $m_2^* \approx 435 [kg]$ ($H_y = 85[\%]$).

In order to investigate the accuracy and efficiency of the optimization methods presented in chapter 5, the optimization problem described in section 2-5 is applied on this case study with $\alpha = 0$. According to figure 6-7, the optimal mass should be $m_1^* \approx 623 [kg]$ ($H_y = 35[\%]$). The settings that are used to generate the optimization results in table 6-7 are shown in table 6-5. From these tables can be concluded that all methods converge towards the optimal mass. However, the integrated optimization approach was more efficient than the nested optimization approach. Again, note that this statement does not always have to be true since it depends on the settings of the optimization algorithm.

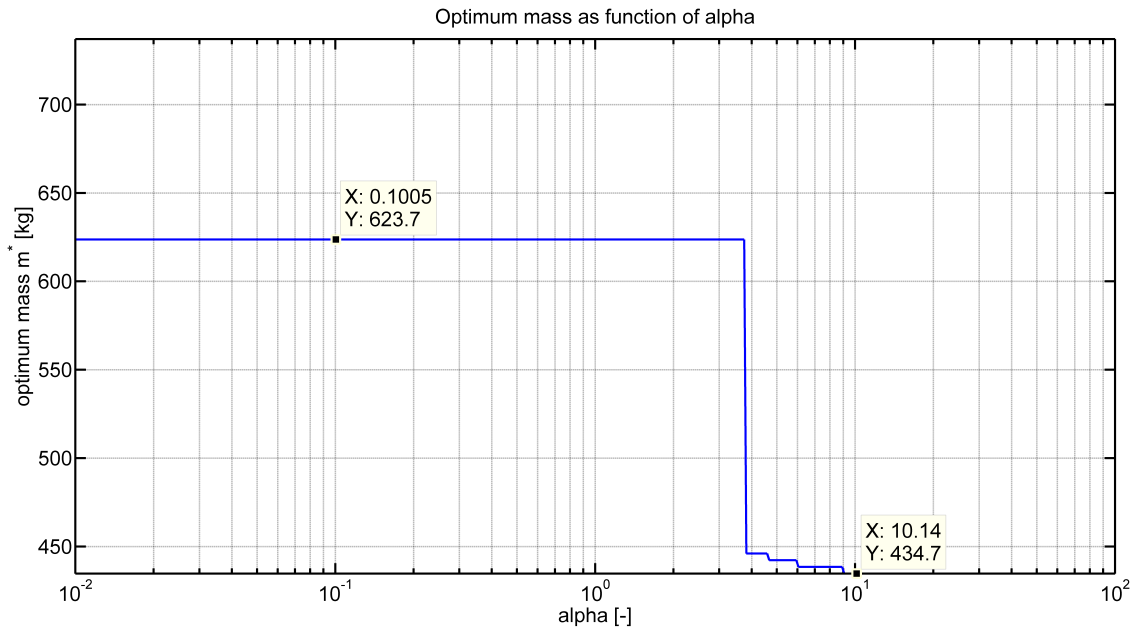


Figure 6-7: Plot which indicates the relation between the optimum mass m^* and the chosen weight constant α under the assumption that the Pareto optimality curve in figure 6-6 approximates the true curve.

	<i>Integrated optimization</i>	$\lambda = 0.5$	$\lambda \approx 0.618$
m^* [kg]	624	620	620
H_y^* [%]	35	36	36
ω_b^* [rad/s]	1928	1905	1905
ω_c^* [rad/s]	4243	4230	4229
K_p^*	$3.12 \cdot 10^9$	$3.01 \cdot 10^9$	$3.01 \cdot 10^9$
iterations	477	1920	2560
PM [deg]	43	43.1	43.1
GM [dB]	11.8	10.1	10.1

Table 6-4: Table with optimization results. A parameter with an asterisk sign (*) indicates that this parameter is optimized according to the settings described in table 6-5.

	<i>Integrated optimization</i>	$\lambda = 0.5$	$\lambda \approx 0.618$
random start	10	10	10
maximum iterations	10	10	10
δ [rad/s]	$1 \cdot 10^{-4}$	1	1
$\omega_b(0)$ [rad/s]	600	600	600
$s(0)$	—	200	200

Table 6-5: Settings of various optimization methods used to generate table 6-4. Note that δ in the integrated optimization case corresponds to the minimum tolerance of the soft requirement.

6-6 Effect of different measurement position

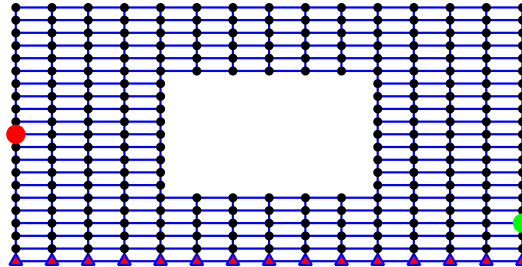


Figure 6-8: Same parameterized structure as in figure 6-1 but this time with a different measurement position, namely at a distance of 17 [%] (0.051 [m]) measured from the right bottom side.

Although the results in section 6-5 are fascinating, they are based on frequency response information between the actuator position and one measurement position. The purpose of this section is to investigate what the effect on the results of the CSO problem is when the measurement position is changed. Figure 6-8 shows the new measurement position which is placed at 17 [%] (0.051 [m]) distance measured from the right-bottom side. Note that this is the only change with respect to the controlled-parameterized structure described in the previous sections. The same methods and techniques that have been used in the case of figure 6-1 are now also applied to the case in figure 6-8. This resulted in the figures 6-9 to 6-11. Notice that the results are quite different with respect to the results in section 6-5. Especially the Pareto optimality curve in figure 6-10 indicates that there might be more optimal mass values m^* possible with respect to α . This assumption is confirmed by figure 6-11. One of the reasons for this change in results might be associated with the concept of *observability*. Notice that the dynamics of the controlled-structure are related to the dynamics of a single point on the structure. However, it is possible that in a certain mode there is no displacement of this measurement point while other points of the structure are moving. This is almost the case for mode two in figure 6-4 and 6-5. Notice also that the magnitude of the resonance peaks shown by the bode diagrams in the figures 6-2 and 6-9 are different. Moreover, the measurement position also affects the phase of the open-loop dynamics. Take for example mode three in figure 6-5 and notice that there will be a sign difference of the PM between a measurement at the top-right position (see figure 6-1) and at the bottom-right position (see figure 6-8). These effects of choosing a different measurement position could cause differences in the outcome of the design approach.

Table 6-6 shows the optimization results when the integrated method is applied for the controlled-structure in figure 6-8. This is done for different α values in order to indicate how the weight of the mass influences the optimization results. Further note that the structure is described by a PDSS model with order three ($mo = 3$). Notice that second column in table 6-6 ($\alpha = 0.4$) should have given a different optimal mass value m^* according to figure 6-11, namely $m^* \approx 623$ [kg]. Figure 6-12 shows why the integrated approach converged

to the other optimal solution $m^* \approx 491$ [kg]. Let obj be the value of:

$$obj = \frac{\bar{\omega}_b}{\omega_b} + \alpha \frac{m}{\bar{m}} \quad (6-10)$$

Equation (6-10) can be rewritten as:

$$\frac{\bar{\omega}_b}{\omega_b} = obj - \alpha \frac{m}{\bar{m}} \quad (6-11)$$

The contour lines for a constant objective value can be drawn with equation 6-11. Figure 6-12 shows that the black line is the contour line with the minimal objective value. However, not far from this black line is the blue line which crosses the red line at multiple points. Because the numerical values of the objective functions are so close to each other, the integrated optimization approach has more difficulty in finding this optimum.

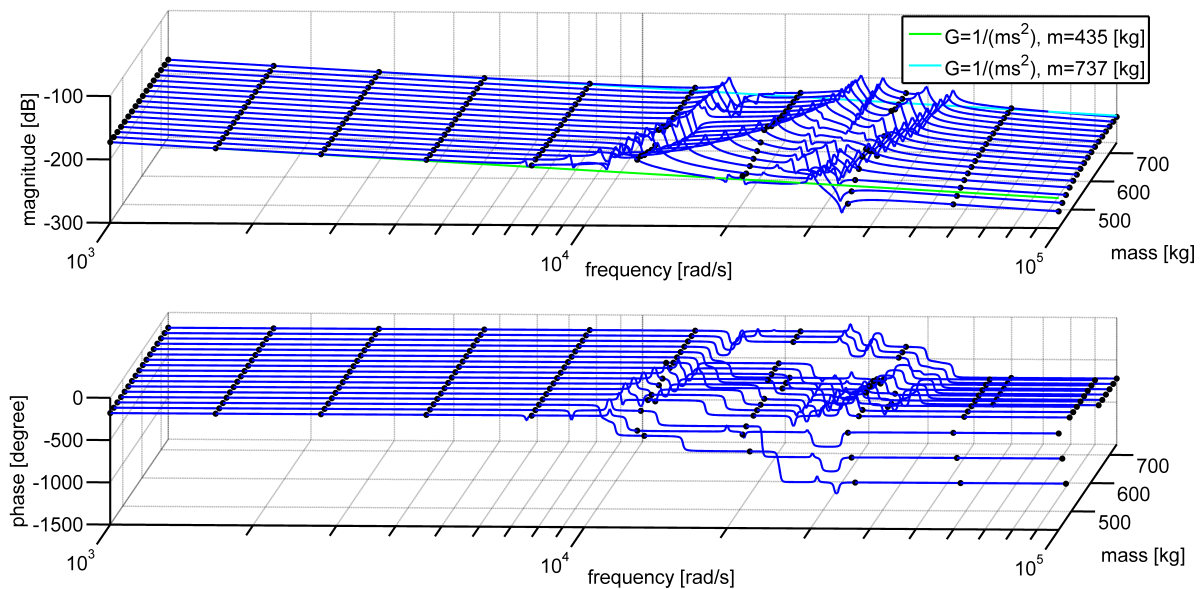


Figure 6-9: 3D plot of multiple open-loop bode diagrams of the parameterized structure shown in figure 6-8 for different hole sizes H_y . Each bode diagram is constructed from eight modes of the original FE model. Notice the difference with figure 6-2.

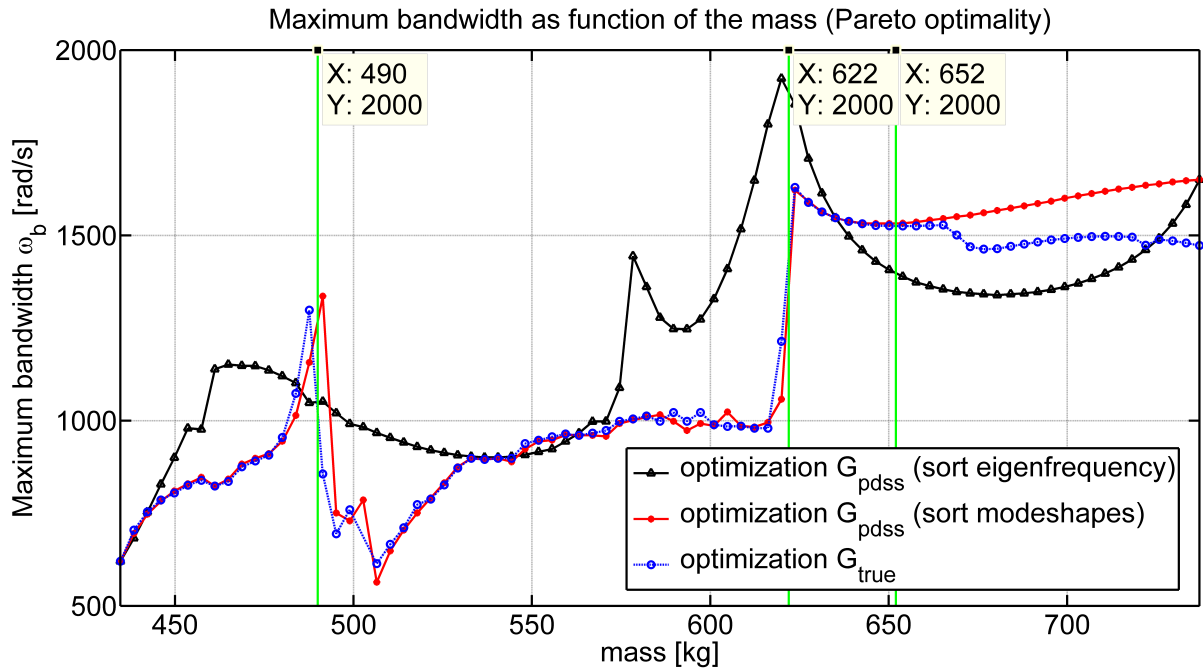


Figure 6-10: Pareto optimality between the objectives bandwidth ω_b and mass m for the controlled parameterized structure in figure 6-8. The vertical green lines indicate a mode switch. Notice the difference with figure 6-6.

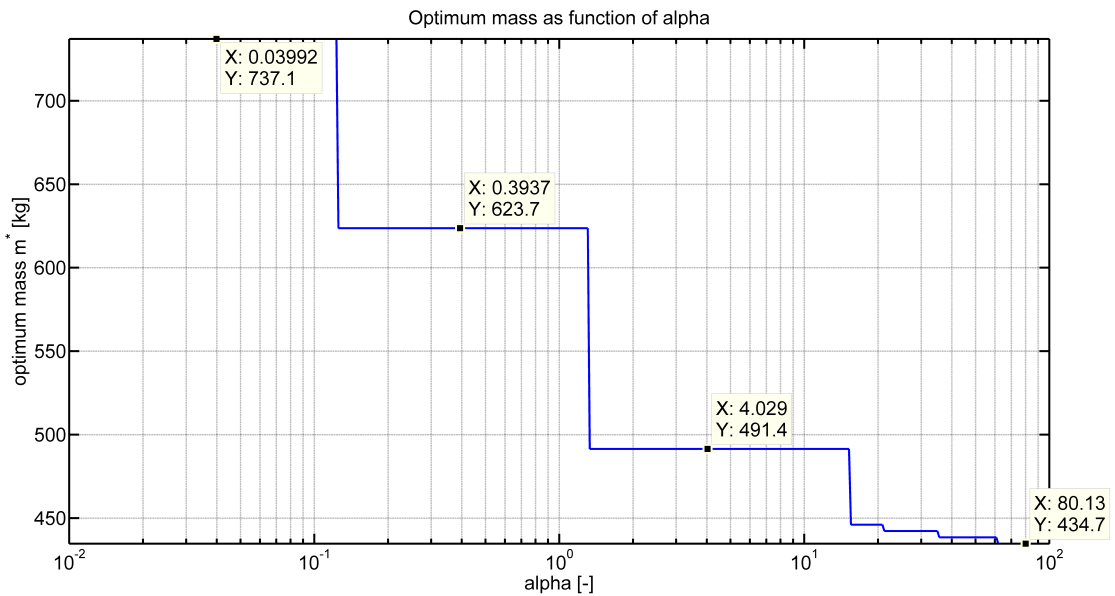


Figure 6-11: Plot which indicates the relation between the optimum mass m^* and the chosen weight constant α under the assumption that the Pareto optimality curve in figure 6-10 approximates the true curve. Notice the difference with figure 6-7.

	$\alpha = 0$	$\alpha = 0.4$	$\alpha = 4$	$\alpha = 100$
m^* [kg]	737	491	491	461
H_y^* [%]	5	70	70	78
ω_b^* [rad/s]	1632	1312	1328	808
ω_c^* [rad/s]	3523	2862	2920	2421
K_p^*	$2.98 \cdot 10^9$	$1.26 \cdot 10^9$	$1.18 \cdot 10^9$	$5.03 \cdot 10^8$
iterations	1351	1116	1212	1065
PM [deg]	42.1	42.2	42.9	43
GM [dB]	8.1	9.1	9.9	8.3

Table 6-6: Table with optimization results based on the integrated optimization approach. A parameter with an asterisk sign (*) indicates that this parameter is optimized according to the settings described in table 6-5. The only difference is that in this case the number of random starts is equal to 20 and the number of maximum iterations is also equal to 20.

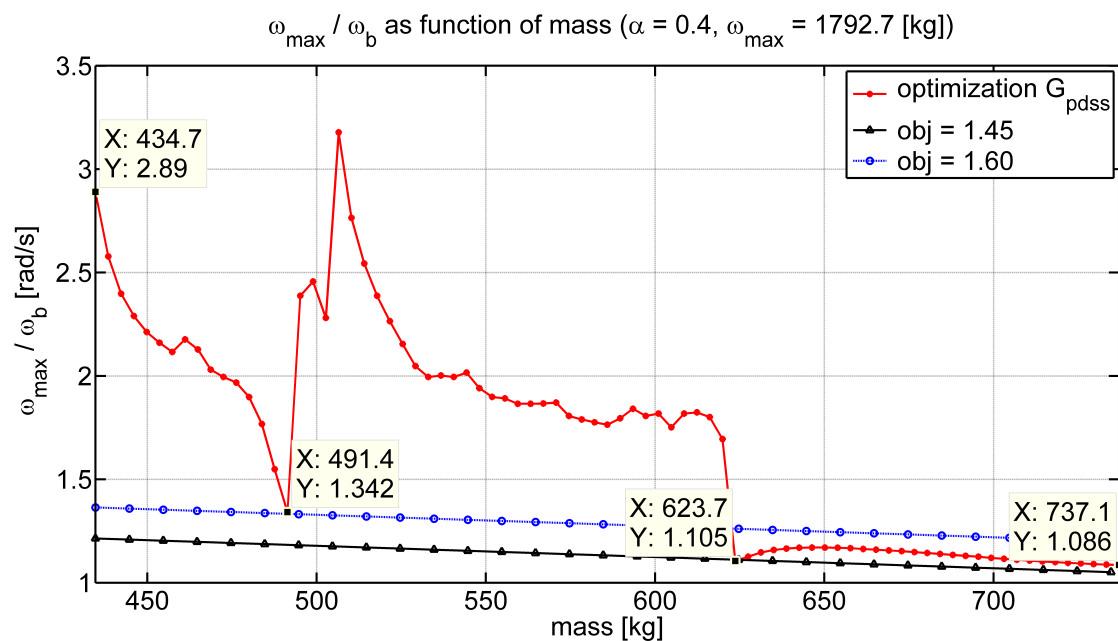


Figure 6-12: Translated Pareto curve of figure 6-10 (red line) and contour lines for constant objective values obj with $\alpha = 0.4$ (blue and black lines). An optimum is found at the point where the red line crosses one of the contour lines from below. Notice that a slight change in the objective value could cause a different local optimum with respect to the optimal mass m^* .

6-7 Mode switching

Section 6-3 already introduced the phenomenon 'mode switching' and the results in section 6-5 and 6-6 showed how much influence this has on the (approximated) Pareto optimality curves. This section investigates the mode switch of the controlled-parameterized structure in figure 6-1 around the point:

- $H_y = 35 [\%] \rightarrow 36 [\%]$ ($m \approx 624 [kg] \rightarrow 620 [kg]$) mode 2 \leftrightarrow mode 3

First, a more detailed view of this phenomenon is presented by figure 6-13. Note that this plot actually zooms in on a very small part of the bode diagrams in figure 6-2. Starting with a relative high mass of the structure ($m \approx 643 [kg]$, $H_y = 30 [\%]$), the magnitude plot in figure 6-2 shows that the first two resonance peaks are moving towards each other as the mass decreases. The red lines in figure 6-2 indicate precisely where the eigenfrequency of mode two becomes larger than the eigenfrequency of mode three. Notice that the magnitude of these red lines decreases for a small period and then increases again. Also the phase plot before and after the mode switch is significantly different. Figure 6-14 shows the effect of this mode switch from a closer look than figure 6-6. In order to understand why there is an increase in terms of performance around this mode switch, a controller C (equation (2-1)) with fixed parameters and a fixed weight W_p is used for three different points in figure 6-14:

- $m \approx 605 [kg]$ ($H_y = 40[\%]$)
- $m \approx 622 [kg]$ ($H_y = 35.5[\%]$)
- $m \approx 643 [kg]$ ($H_y = 30[\%]$)

The parameters for C are in this case based on the controlled-structure with $m \approx 605 [kg]$ ($H_y = 40[\%]$):

- $Kp = 1.83 \cdot 10^9$
- $\omega_c = 3.57 \cdot 10^3 [rad/s]$

The idea behind this fixed controller is that according to figure 6-14, the controller C and the parameterized structure with $m \approx 605 [kg]$ should give a sensitivity function which nearly violates $\|W_p S\|_\infty < 1$. However, if this same controller is used for the parameterized structure with $m \approx 643 [kg]$, the weighted sensitivity function $W_p S$ will probably be larger than one at some point. Now, if the same controller is used for the parameterized structure with $m \approx 622 [kg]$, which is close to the mode switch, some distance between the sensitivity function S and the upper bound $\frac{1}{|W_p|}$ should be visible.

Figure 6-15 and 6-15 show the results of this fixed controller C on three different mass values of the parameterized structure. Figure 6-15 shows the upper bound $\frac{1}{|W_p|}$ and the sensitivity functions. Here, it is clearly visible that $m \approx 605$ [kg] (blue line) stays just under the upper bound while $m \approx 643$ [kg] (green line) violates the prescribed constraint. The red line corresponds to the controlled-structure with a mass $m \approx 620$ [kg]. This is close to the position where mode switching occurs. Notice that the peak of the red line just after a frequency of $1 \cdot 10^4$ [rad/s] is significantly lower than the others. This indicates that it might be possible to increase the bandwidth ω_b while respecting the constraint $\|W_p S\|_\infty < 1$ by optimizing the control parameters K_p and ω_c . However, it cannot be said that around every mode switching a decrease in magnitude appears.

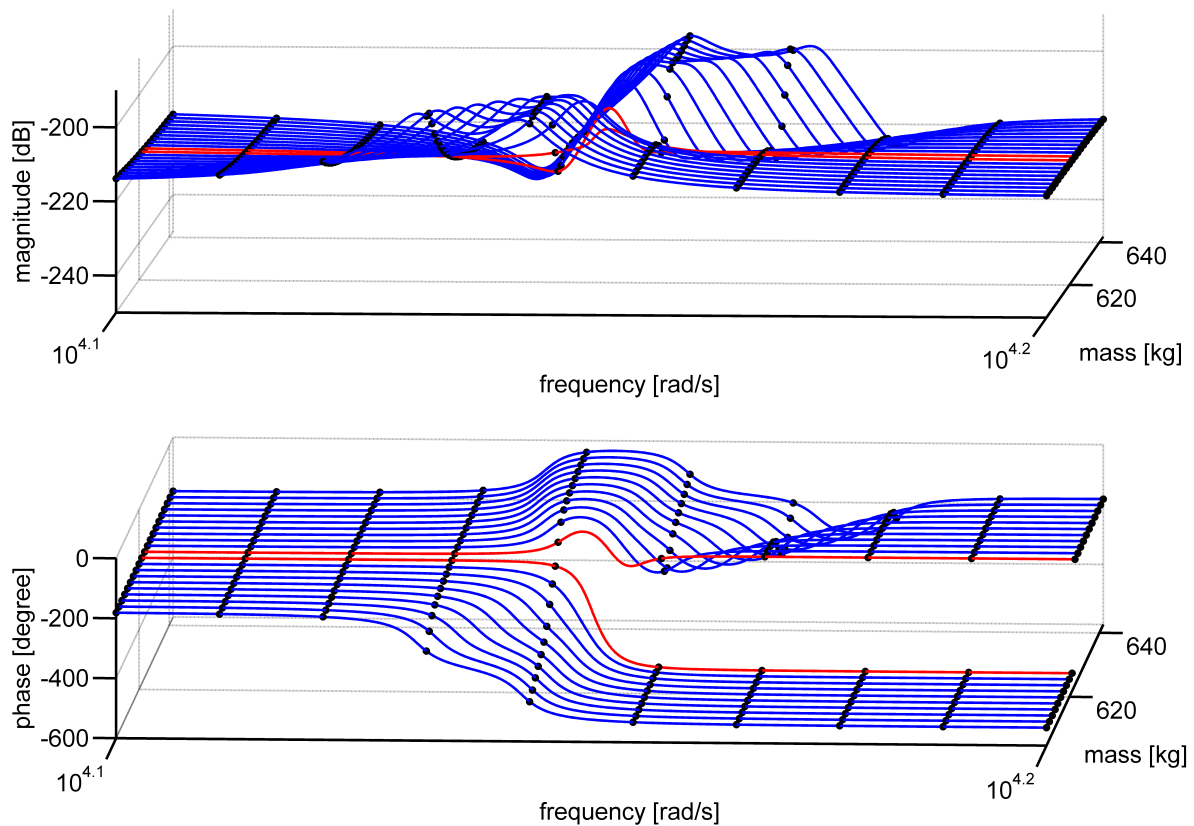


Figure 6-13: Mode switching behaviour between mode two and three. This figure is created by zooming in on figure 6-2 between $m \approx 605$ [kg] ($H_y = 40[\%]$) and $m \approx 643$ [kg] ($H_y = 30[\%]$). The red lines indicate the bode diagrams that belong to $H_y = 35[\%]$ and $H_y = 35.5[\%]$.

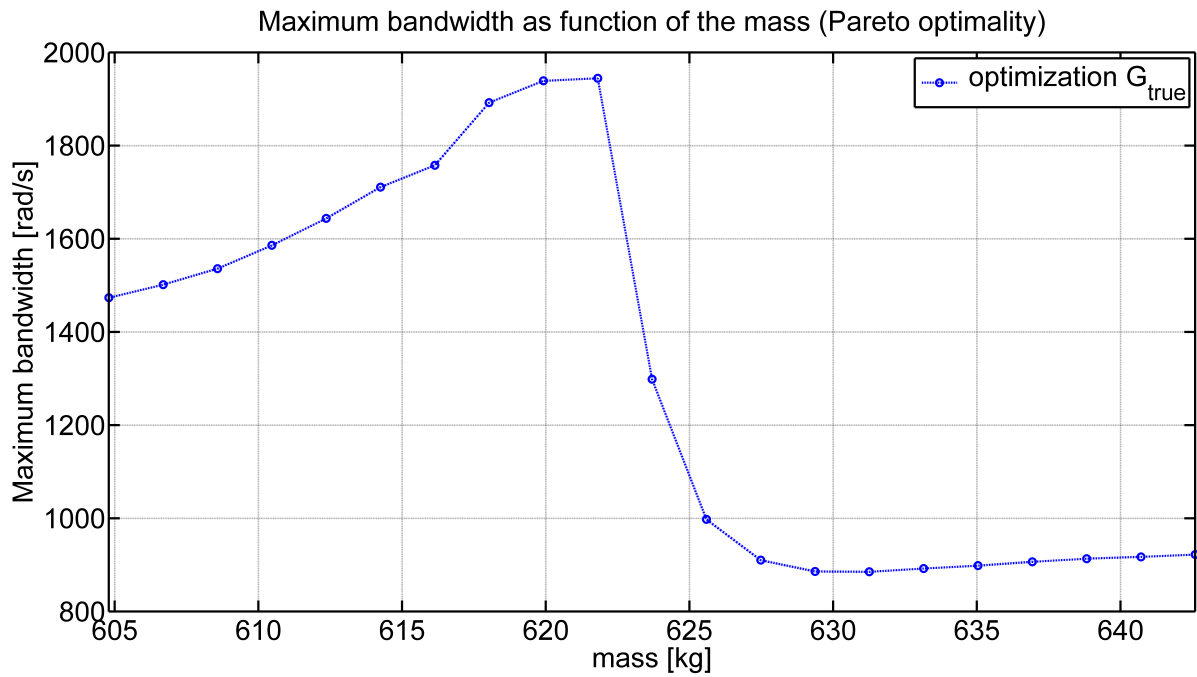


Figure 6-14: Pareto optimality for the controlled-parameterized structure in figure 6-2. The bounds are between $m \approx 605$ [kg] ($H_y = 40\%$) and $m \approx 643$ [kg] ($H_y = 30\%$).

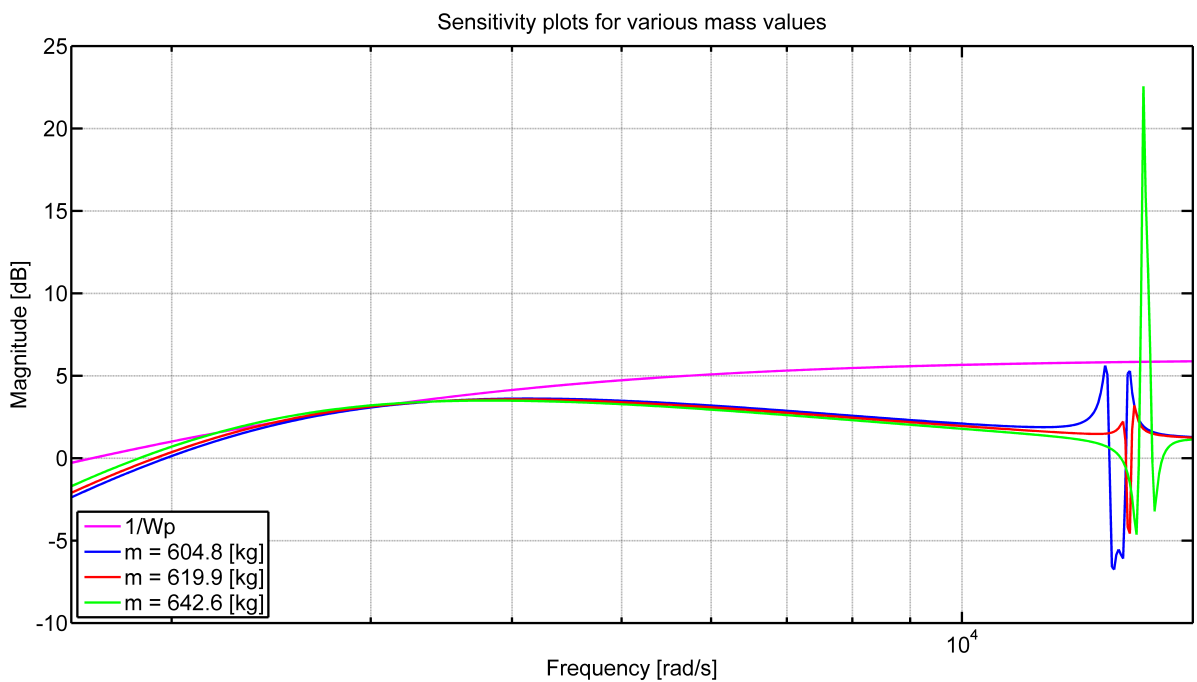


Figure 6-15: Multiple sensitivity plots for three masses in one figure. Note that the controller C for each sensitivity plot is the same. The parameters for C are related to the optimization results with a constant mass of ≈ 643 [kg] ($H_y = 30\%$).

Conclusions and recommendations

High performance requirements for controlled mechanical structures like a wafer stage are normal nowadays. In order to meet with these high requirements, both the mechanical structure and controller should be optimized as much as possible. This type of problem is often classified as multi-objective and non-convex and is associated with the term *controller-structure optimization* (CSO). This MSc thesis considers a CSO problem where the structure is characterized by a few parameters. Some of these parameters will be considered as design variables. For this particular case of CSO problem, chapter 2 proposed a design approach. The idea behind this design approach is that it might be possible to approximate the solution of the comprehensive CSO problem by using an approximate small-scale model in the form of a *parameter-dependent state-space* (PDSS) model of the parameterized structure instead of using large *finite element* (FE) models.

The first sub-problem was to find out how to model a well-conditioned accurate PDSS model. Chapter 3 explained that a PDSS model can be constructed from N samples of the original model. In order to assure that this model is well-conditioned, the local LTI models should have the same coherent basis. Moreover, it is recommended to choose a basis with few varying elements in the system matrices because it reduces the problem of determining the unknown coefficients in (2-3) [Steinbuch et al., 2003]. If the local LTI models are obtained via modal truncation and represented in modal state-space form, additional techniques like ordering modes based on their modeshapes can significantly improve the accuracy of the PDSS model. This conclusion is based on the Pareto optimality curves shown in the figures 6-10 and 6-6 and the tables 6-2 and 6-3. Furthermore, it is recommended in section 3-2 that for this particular case, additional restrictions on the eigenmodes ϕ_r should be applied in order to improve the condition of the local LTI models for interpolation purposes. The showcase example in section 4-5 and the results of the final case study in chapter 6 showed that for some CSO problems it is enough to construct a PDSS model from only four samples of the original structure and with a maximum polynomial order mo of three. Note that the unknown coefficients in (4-2) are determined by solving a linear least-squares problem. The first recommendation will be to investigate different methods for optimizing these unknown coefficients. Furthermore, a more accurate PDSS model might be found if other PDSS model

structures are used instead of the one described by (4-2) with the polynomial relation (4-3). Finally, the possibilities of the PDSS model can probably be improved by finding better techniques for ordering the matrices $\tilde{\mathbf{V}}$ and $\tilde{\mathbf{U}}$ according to their modeshapes.

The second sub-problem is to quantify how good the derived PDSS model matches with the original model (e.g. FE model). In section 4-4, four different indicators were defined for this purpose. At first instance, the indicators were applied to the showcase example in section 4-5. Table 4-1 shows that in case of the showcase example, increasing the maximum polynomial mo up to the point where the least-squares problem is underdetermined, results in more accurate PDSS models. This conclusion also applies for the final case study in chapter 6. However, the numerical values for the indicators r_2 (equation (4-14)) and E_{tot} (equation (4-16)) are difficult to interpret. The indicators $E_{\nu_{g\infty}}$ (equation (4-18)) and $E_{\nu_{g2}}$ (equation (4-19)) have values between zero and one, but they became very small in the final case study (see table 6-2 and 6-3). Therefore, it remains difficult to quantify how accurate a PDSS model is from a single indicator. This became very clear in section 6-4 where some indicators presented in the tables 6-2 and 6-3 showed little differences with respect to each other, although the final results in terms of the Pareto optimality curve in figure 6-6 showed large differences for both cases. Therefore, it will be recommended to do further research in finding more appropriate indicators.

The third sub-problem is to formulate a proper optimization problem for finding the optimal design variables \mathbf{x}_d . To perform this task, proper optimization criteria must be defined before a solution can be found. In this MSc thesis, a simple (normalised) objective function is prescribed which contains on one side the sub-objective of maximizing the bandwidth ω_b and on the other side the sub-objective of minimizing the mass m of the structure. The importance of minimizing the mass can be controlled by the weight α . For the case that $\alpha = 0$, the optimization criteria in both the showcase example in section 5-4 and the final case study in chapter 6 resulted in satisfactory results (i.e. the bandwidth was maximized). For the case that $\alpha > 0$, the idea was that by slowly increasing α , the mass of the structure would be reduced in a smooth way. Unfortunately, the figures 6-7 and 6-11 showed that for the final case study, the optimum mass m^* as function of α is extremely non-smooth (i.e. jumps in the solution). The reason for this behaviour is related to the discrete nature of the Pareto optimality curve in the figures 6-6 and 6-10. Moreover, the showcase example in section 5-4 showed that the current optimization criteria resulted a step response with visible high frequency signals in it. It will be recommended to either specify the weight W_p on the sensitivity function S more accurately or to include additional weights on other closed-loop transfer functions in order to better predict the outcome of the optimization process. Furthermore, criteria on the input signals, maximum stress levels of the parameterized structure and some robustness specification should be included as well. In this way, the results will probably become more feasible.

The fourth sub-problem is to test and analyse integrated optimization methods. In this MSc thesis, a non-smooth and non-convex optimization algorithm is used in order to perform an integrated optimization (see chapter 5). Testing and analyses are done on the showcase example in section 5-4 and on the final case study in chapter 6. In both cases, integrated optimization turned out to be quite efficient in terms of the number of iterations that was required compared to the nested approaches (see chapter 5). The accuracy of the solution was satisfactory in the showcase example in section 5-4 (table 5-1) but this was not the case for section 6-6 (table 6-6). In the latter case, the results were very sensitive to the settings of the

optimization algorithm and the initial conditions because the difference in objective values between the optima is small (see figure 6-12). In order to compute the Pareto optimality curve, a nested optimization approach is used instead of an integrated optimization approach because it makes smart use of maximizing the bandwidth ω_b via a kind of line search method (see section 5-3). The initial conditions for both the integrated and the nested optimization method determine for a large part the effectiveness and efficiency of these algorithms in the examined cases. Therefore, it is recommended to investigate the use of different optimization methods with different settings for solving CSO problems.

The final case study which is presented in chapter 6 was used to test the design approach. This case study showed that in some particular cases it is possible to approximate the solution of a CSO problem by using the design approach presented in chapter 2. Note that the assumption is made that the *single input single output* (SISO) controlled-structure is characterized by a few parameters. However, one of the observations in chapter 6 was that by changing the measurement position of the controlled-structure, the results in terms of the Pareto optimality curves changed as well. Since physical structures are defined in a three dimensional environment, it is recommended to include information from multiple measurement positions on the structure. In this way it is less likely that certain modes are unobservable. Finally, maximizing the first eigenfrequency of a controlled-structure does not necessarily mean that the most optimal structural design is obtained because this depends on the definition of the objectives and constraints. This is for example shown by non-trivial solution that occurred in the final case study (see section 6-5). Moreover, it is for example not unthinkable that high magnitudes of the second resonance peak or the use of more complex fixed-structure controllers could invalidate the statement that the structure with the highest first eigenfrequency corresponds with the optimum. Future research should determine if the proposed design approach is able to handle more complex CSO problems (e.g. more structural design and more control design parameters).

Modelling a block with a hole in 2D with the finite element methods

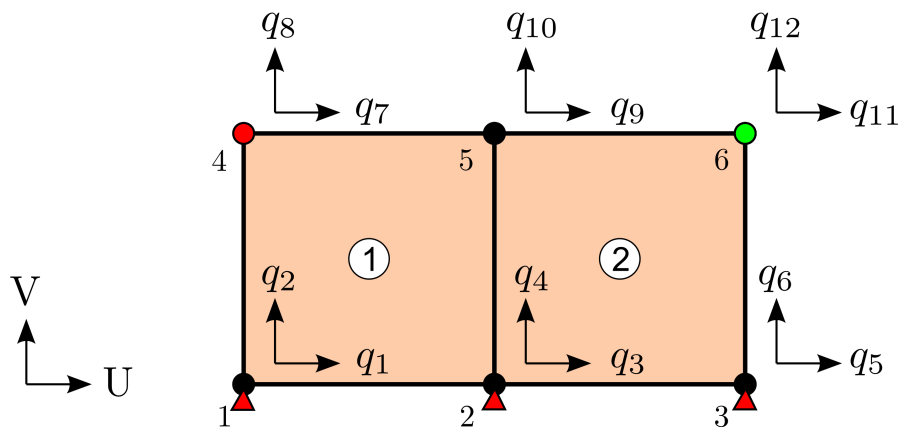


Figure A-1: Reference FE model consisting of 4 elements. The black dots represent the nodes of the FE model and the q terms represent the dofs.

This appendix gives more information about how the FE model in chapter 6 is modelled in MATLAB. The main file of this FE model is called `cartwithhole.m`. However, in order to explain the modelling techniques, a reference FE model with only four elements will be used in this section (see figure A-1). The red triangles indicate that the dofs in the V -direction for those nodes are constrained. The red dot at node four (top left side) defines the position of the actuator (i.e. force) and the green dot at node six (top right side) defines the measurement position. Note that both the actuation and the measurement takes place in the U -direction. First, the geometry of the structure will be defined by nodes and elements. Second, the global mass matrix \mathbf{M} and global stiffness matrices \mathbf{K} is constructed. This process requires that the element mass matrix \mathbf{M}_{el} and element stiffness matrix \mathbf{K}_{el} are known. Appendix B gives more information about deriving \mathbf{M}_{el} and \mathbf{K}_{el} for a bilinear rectangle Q4 element.

The FE model in figure A-1 has the following constant parameters:

$$\begin{aligned}
 Lx &= 0.6 \text{ [m]} = \text{length of square in x-direction} \\
 Ly &= 1 \text{ [m]} = \text{length of square in y-direction} \\
 h &= 1 \text{ [m]} = \text{depth of square} \\
 nx &= 3 \text{ number of nodes in x-direction} \\
 ny &= 2 \text{ number of nodes in y-direction}
 \end{aligned} \tag{A-1}$$

The first step is to define a mesh for the squared geometry in figure A-1. The square is described by four bilinear rectangle Q4 elements and thus there are six nodes. The numbering of these nodes starts at the left bottom side and goes towards the right bottom side. Then, it continues one level higher in the V-direction from the left side towards the right side. This numbering goes on until all the nodes are numbered. The *node coordinates* that correspond to the numbering of the nodes starts with node 1 at position $\{U, V\} = \{0, 0\}$. The distance of between node 1 and the most right bottom node, in this case node 3, should be equal to the pre-described horizontal length Lx . In the same manner the other node coordinates can be derived. In the situation of figure A-1 this results in:

node number	1	2	3	4	5	6
U	0	0.3	0.6	0	0.3	0.6
V	0	0	0	1	1	1

Table A-1: Node coordinates of the reference FE model in figure A-1

The node connectivity matrix specifies which nodes belong to which elements. This is shown by the second column of table A-2. Each node has two dofs, one horizontal U_i and one vertical V_i . Therefore, the reference FE model has in total 12 dofs. The vector of structural displacements \mathbf{q} for these dofs will be defined as follows:

$$\begin{aligned}
 \mathbf{q}^T &= [U_1 \quad V_1 \quad U_2 \quad V_2 \quad U_3 \quad V_3 \quad \cdots \quad U_6 \quad V_6] \\
 &= [q_1 \quad q_2 \quad q_3 \quad q_4 \quad q_5 \quad q_6 \quad \cdots \quad q_{11} \quad q_{12}]
 \end{aligned} \tag{A-2}$$

The relation between the element number and the corresponding dofs is given by the *localization vector*. For the reference FE model, this is shown in table A-2. The remaining

<i>element e</i>	<i>nodes</i>	<i>localization vectors</i>
1	[1 2 4 5]	[1 2 3 4 7 8 9 10]
2	[2 3 5 6]	[3 4 5 6 9 10 11 12]

Table A-2: Node connectivity matrix and localization vectors for structure of figure A-1

information regarding the constraints is defined by table A-3 and the information about actuator and measurement positions is stored by the vectors \mathbf{F} and \mathbf{P} (see table A-4).

$$\begin{aligned}
 \mathbf{doffix} &= [2 \quad 4 \quad 6] \\
 \mathbf{doffree} &= [1 \quad 3 \quad 5 \quad 7 \quad 8 \quad 9 \quad 10 \quad 11 \quad 12]
 \end{aligned}$$

Table A-3: Constraints of the reference FE model in figure A-1

$$K = 10^{11} \begin{bmatrix} 3.54 & 0.58 & -3.42 & 0.19 & 0 & 0 & 1.65 & -0.19 & -1.77 & -0.58 & 0 & 0 \\ 0.58 & 1.19 & -0.19 & -0.72 & 0 & 0 & 0.19 & 0.13 & -0.58 & -0.59 & 0 & 0 \\ -3.42 & -0.19 & 7.07 & 0 & -3.42 & 0.19 & -1.77 & 0.58 & 3.30 & 0 & -1.77 & -0.58 \\ 0.19 & -0.72 & 0 & 2.38 & -0.19 & -0.72 & 0.58 & -0.59 & 0 & 0.25 & -0.58 & -0.59 \\ 0 & 0 & -3.42 & -0.19 & 3.54 & -0.58 & 0 & 0 & -1.77 & 0.58 & 1.65 & 0.19 \\ 0 & 0 & 0.19 & -0.72 & -0.58 & 1.19 & 0 & 0 & 0.58 & -0.59 & -0.19 & 0.13 \\ 1.65 & 0.19 & -1.77 & 0.58 & 0 & 0 & 3.54 & -0.58 & -3.42 & -0.19 & 0 & 0 \\ -0.19 & 0.13 & 0.58 & -0.59 & 0 & 0 & -0.58 & 1.19 & 0.19 & -0.72 & 0 & 0 \\ -1.77 & -0.58 & 3.30 & 0 & -1.77 & 0.58 & -3.42 & 0.19 & 7.07 & 0 & -3.42 & -0.19 \\ -0.58 & -0.59 & 0 & 0.25 & 0.58 & -0.59 & -0.19 & -0.72 & 0 & 2.38 & 0.19 & -0.72 \\ 0 & 0 & -1.77 & -0.58 & 1.65 & -0.19 & 0 & 0 & -3.42 & 0.19 & 3.54 & 0.58 \\ 0 & 0 & -0.58 & -0.59 & 0.19 & 0.13 & 0 & 0 & -0.19 & -0.72 & 0.58 & 1.19 \end{bmatrix} \quad (\text{A-4})$$

$$M = \begin{bmatrix} 233 & 0 & 117 & 0 & 0 & 0 & 117 & 0 & 58 & 0 & 0 & 0 \\ 0 & 233 & 0 & 117 & 0 & 0 & 0 & 117 & 0 & 58 & 0 & 0 \\ 117 & 0 & 467 & 0 & 117 & 0 & 58 & 0 & 233 & 0 & 58 & 0 \\ 0 & 117 & 0 & 467 & 0 & 117 & 0 & 58 & 0 & 233 & 0 & 58 \\ 0 & 0 & 117 & 0 & 233 & 0 & 0 & 0 & 58 & 0 & 117 & 0 \\ 0 & 0 & 0 & 117 & 0 & 233 & 0 & 0 & 0 & 58 & 0 & 117 \\ 117 & 0 & 58 & 0 & 0 & 0 & 233 & 0 & 117 & 0 & 0 & 0 \\ 0 & 117 & 0 & 58 & 0 & 0 & 0 & 233 & 0 & 117 & 0 & 0 \\ 58 & 0 & 233 & 0 & 58 & 0 & 117 & 0 & 467 & 0 & 117 & 0 \\ 0 & 58 & 0 & 233 & 0 & 58 & 0 & 117 & 0 & 467 & 0 & 117 \\ 0 & 0 & 58 & 0 & 117 & 0 & 0 & 0 & 117 & 0 & 233 & 0 \\ 0 & 0 & 0 & 58 & 0 & 117 & 0 & 0 & 0 & 117 & 0 & 233 \end{bmatrix} \begin{bmatrix} q_1 \\ q_2 \\ q_3 \\ q_4 \\ q_5 \\ q_6 \\ q_7 \\ q_8 \\ q_9 \\ q_{10} \\ q_{11} \\ q_{12} \end{bmatrix} \quad (\text{A-5})$$

The following command takes into account that there are constraints and measurement and actuator positions defined:

```
1 [V,D,sysmd] = get_model(mesh,K,M,loads,n,zeta);
```

First, it eliminates the rows and columns that correspond to fixed dofs (**doffix**). Second, it solves the *free vibration problem* (see appendix D) with the MATLAB function *eigs()*. The resulting modes together with the actuator position **F** and measurement position **P** are used for constructing a modal state-space model. Figure A-2 shows the first four modes of the reference FE model according to increasing eigenfrequency ω_r . Figure A-3 show the dynamics of the reference FE model from the actuator position to measurement position in a bode diagram. Notice that the calculated eigenfrequencies (see titles in figure A-2) correspond with the resonance frequencies in the bode plot of figure A-3.

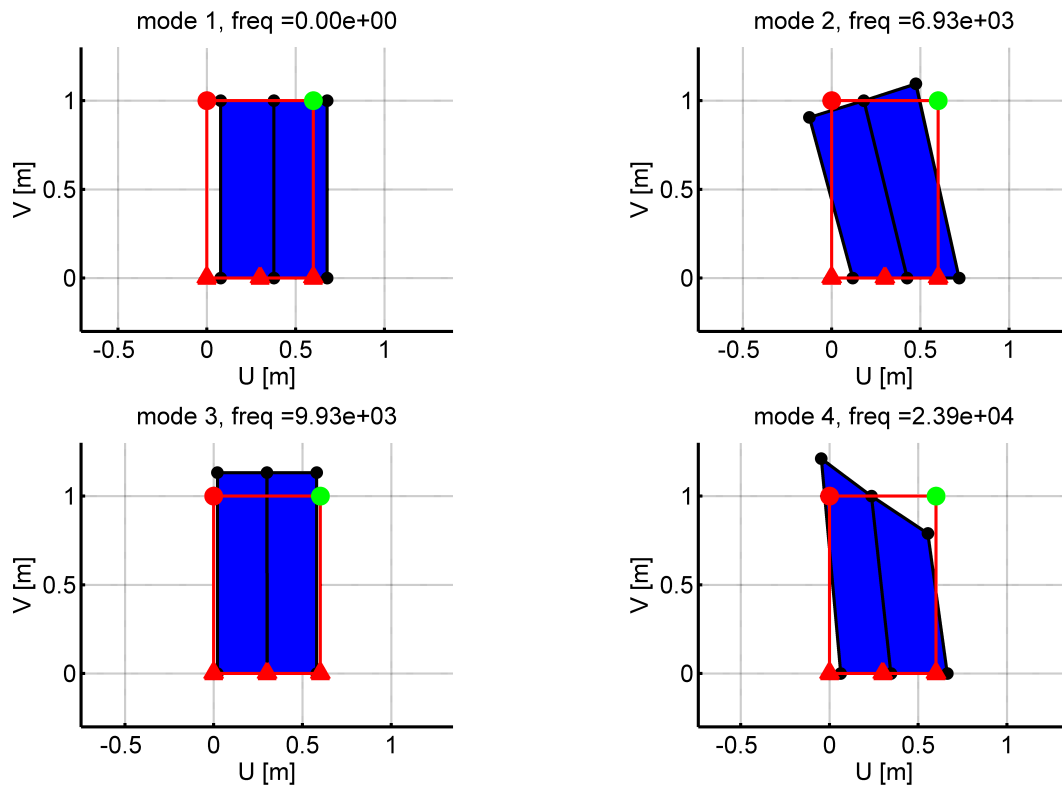


Figure A-2: First four modes according to increasing eigenfrequency ω_r for the reference FE model.

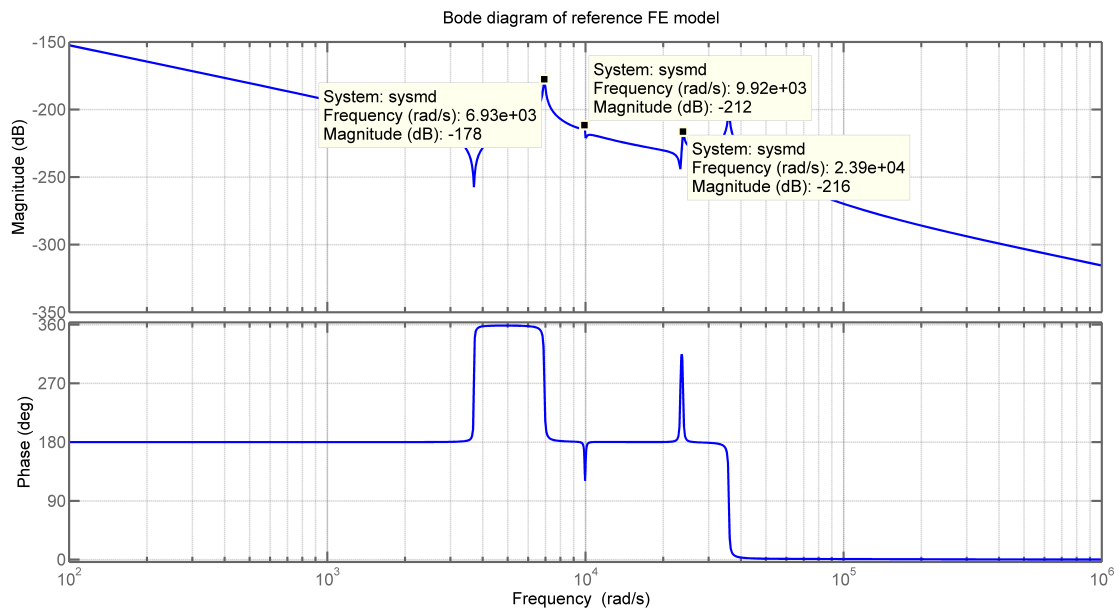


Figure A-3: Bode diagram of the reference FE model.

Appendix B

Deriving element matrices for a bilinear rectangle Q4

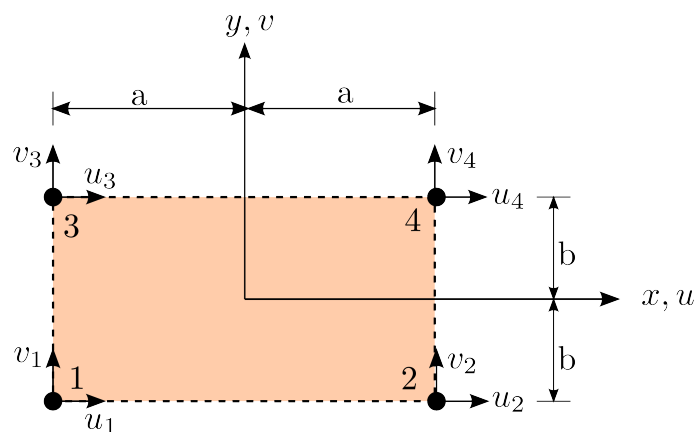


Figure B-1: Reference model for deriving stiffness and mass matrix.

The following equations and theory are based on literature from Rixen [2011 - 2012]. Starting from an infinitesimal volume into the continuum and assuming

1. small deformations
2. small rotations
3. material is homogeneous, linear and elastic

The equations expressing linear dynamic equilibrium can be written in the following matrix

form:

$$\begin{aligned}
\mathbf{D}^T \boldsymbol{\sigma} + \hat{\mathbf{X}} - \rho \ddot{\mathbf{u}} &= 0 && \text{in } V \\
\mathbf{N}^T \boldsymbol{\sigma} &= \hat{\mathbf{t}} && \text{on } S_\sigma \\
\boldsymbol{\sigma} &= \mathbf{H} \boldsymbol{\epsilon} \\
\boldsymbol{\epsilon} &= \mathbf{D} \mathbf{u} \\
\mathbf{u} &= \hat{\mathbf{u}} && \text{on } S_u
\end{aligned} \tag{B-1}$$

with the following matrix notations for a *three dimensional* (3D) problem

$$\mathbf{u} = [u_1 \quad u_2 \quad u_3]^T \tag{B-2}$$

$$\boldsymbol{\sigma} = [\sigma_{11} \quad \sigma_{22} \quad \sigma_{33} \quad \sigma_{12} \quad \sigma_{23} \quad \sigma_{13}]^T \tag{B-3}$$

$$\boldsymbol{\epsilon} = [\varepsilon_{11} \quad \varepsilon_{22} \quad \varepsilon_{33} \quad \gamma_{12} \quad \gamma_{23} \quad \gamma_{13}]^T \tag{B-4}$$

$$\mathbf{D}^T = \begin{bmatrix} \frac{\partial}{\partial x_1} & 0 & 0 & \frac{\partial}{\partial x_2} & 0 & \frac{\partial}{\partial x_3} \\ 0 & \frac{\partial}{\partial x_2} & 0 & \frac{\partial}{\partial x_1} & \frac{\partial}{\partial x_3} & 0 \\ 0 & 0 & \frac{\partial}{\partial x_3} & 0 & \frac{\partial}{\partial x_2} & \frac{\partial}{\partial x_1} \end{bmatrix} \tag{B-5}$$

Note that $\gamma_{ij} = 2\varepsilon_{ij}$. The relation between stress $\boldsymbol{\sigma}$ and strain $\boldsymbol{\epsilon}$ is defined by Hooke's law:

$$\boldsymbol{\sigma} = \mathbf{H} \boldsymbol{\epsilon} \tag{B-6}$$

Hooke's matrix for an isotropic elastic material in three dimensions is:

$$\mathbf{H} = \begin{bmatrix} \lambda + 2G & \lambda & \lambda & 0 & 0 & 0 \\ \lambda & \lambda + 2G & \lambda & 0 & 0 & 0 \\ \lambda & \lambda & \lambda + 2G & 0 & 0 & 0 \\ 0 & 0 & 0 & G & 0 & 0 \\ 0 & 0 & 0 & 0 & G & 0 \\ 0 & 0 & 0 & 0 & 0 & G \end{bmatrix} \tag{B-7}$$

with

$$\lambda = \frac{E\nu}{(1+\nu)(1-2\nu)} \tag{B-8}$$

Rewriting equation B-6 gives a formula which describes the strains as function of the stresses:

$$\boldsymbol{\epsilon} = \mathbf{H}^{-1} \boldsymbol{\sigma} \tag{B-9}$$

with the term \mathbf{H}^{-1} :

$$\mathbf{H}^{-1} = \frac{1}{E} \begin{bmatrix} 1 & -\nu & -\nu & 0 & 0 & 0 \\ -\nu & 1 & -\nu & 0 & 0 & 0 \\ -\nu & -\nu & 1 & 0 & 0 & 0 \\ 0 & 0 & 0 & \frac{E}{G} & 0 & 0 \\ 0 & 0 & 0 & 0 & \frac{E}{G} & 0 \\ 0 & 0 & 0 & 0 & 0 & \frac{E}{G} \end{bmatrix} \tag{B-10}$$

For a *two dimensional* (2D) problem, Hooke's matrix H can be reduced in two different ways. The first option is to start from the equations B-6 and B-7 and remove the rows and columns which corresponds to strain and stress in the z-direction (indicated by a subscript '3'). This will result in the *plain strain* relation. In this state the strain in the z-direction ϵ_{33} and the shear strain γ_{13} and γ_{23} are assumed to be zero. This typically occurs in situations where the dimension of the structure in one direction (e.g. z-direction) is very large with respect to the other directions. Practical applications are dams, tunnels, bars etc. The resulting \mathbf{H} matrix for the 2D plain strain case is given by equation B-11

$$\begin{bmatrix} \sigma_{11} \\ \sigma_{22} \\ \sigma_{12} \end{bmatrix} = \begin{bmatrix} \lambda + 2G & \lambda & 0 \\ \lambda & \lambda + 2G & 0 \\ 0 & 0 & G \end{bmatrix} \begin{bmatrix} \epsilon_{11} \\ \epsilon_{22} \\ \gamma_{12} \end{bmatrix} \quad (\text{B-11})$$

The second option is to start from the equations B-9 and B-10 and again remove the rows and columns which correspond to strain and stress in the z-direction. However, in this case the inverse of the resulting matrix must be taken before one arrives at the constitutive matrix H given by equation B-12. This relation is defined to be in a state of stress in which the normal stress σ_{33} and the shear stress σ_{13} and σ_{23} , are assumed to be zero or negligible. The geometry of the body is essentially a plate with one dimension much smaller than the others.

$$\begin{bmatrix} \sigma_{11} \\ \sigma_{22} \\ \sigma_{12} \end{bmatrix} = \frac{E}{1 - \nu^2} \begin{bmatrix} 1 & \nu & 0 \\ \nu & 1 & 0 \\ 0 & 0 & \frac{1-\nu}{2} \end{bmatrix} \begin{bmatrix} \epsilon_{11} \\ \epsilon_{22} \\ \gamma_{12} \end{bmatrix} \quad (\text{B-12})$$

In the context of this thesis, only the constitutively matrix H for the *plain strain* situation will be used for model purposes. Furthermore, the following notions will be used for deriving the 2D stiffness matrix.

$$\mathbf{u} = \begin{bmatrix} u_1 & u_2 \end{bmatrix}^T \quad (\text{B-13})$$

$$\boldsymbol{\sigma} = \begin{bmatrix} \sigma_{11} & \sigma_{22} & \sigma_{12} \end{bmatrix}^T \quad (\text{B-14})$$

$$\boldsymbol{\varepsilon} = \begin{bmatrix} \varepsilon_{11} & \varepsilon_{22} & \gamma_{12} \end{bmatrix}^T \quad (\text{B-15})$$

$$\mathbf{D}^T = \begin{bmatrix} \frac{\partial}{\partial x_1} & 0 & \frac{\partial}{\partial x_2} \\ 0 & \frac{\partial}{\partial x_2} & \frac{\partial}{\partial x_1} \end{bmatrix} \quad (\text{B-16})$$

Discretization of the continuous linear dynamical system results in the discretized mass and stiffness matrices:

$$\mathbf{M} = \int_V \rho \mathbf{F}^T \mathbf{F} dV \quad (\text{B-17})$$

$$\mathbf{K} = \int_V \mathbf{B}^T \mathbf{H} \mathbf{B} dV \quad (\text{B-18})$$

For the 2D case this comes down to:

$$\mathbf{M}_{el} = \int_{-b}^b \int_{-a}^a \rho h \mathbf{F}^T \mathbf{F} dx dy \quad (\text{B-19})$$

$$\mathbf{K}_{el} = \int_{-b}^b \int_{-a}^a h \mathbf{B}^T \mathbf{H} \mathbf{B} dx dy \quad (\text{B-20})$$

The term h represents the depth in the third dimension (i.e. z -direction).

The \mathbf{B} matrix is called the *strain interpolation matrix*:

$$\varepsilon(\mathbf{x}, t) = \underbrace{\mathbf{DF}(x_1, x_2)}_{:=\mathbf{B}(x_1, x_2)} \mathbf{q}(t) \quad (\text{B-21})$$

The matrix \mathbf{F} contains the shape functions. In some literature (Cook et al. [2002] and Felippa [2004]) this matrix is denoted with \mathbf{N} . The number of rows in \mathbf{F} are equal to the dimension of the FE model (i.e. two for 2D, three for 3D etc.) and the number of columns are equal to the number of nodes n in an element.

$$\mathbf{N} = \mathbf{F}(x_1, x_2) = \begin{bmatrix} f_{11}(x_1, x_2) & \cdots & f_{1n}(x_1, x_2) \\ f_{21}(x_1, x_2) & \cdots & f_{2n}(x_1, x_2) \end{bmatrix} \quad (\text{B-22})$$

The matrix \mathbf{N} describes the static relation between the displacement of the element $\phi(x, y)$ as function of the locations individual nodes ϕ_e :

$$\phi(x, y) = \mathbf{N}\phi_e \quad (\text{B-23})$$

According to Cook et al. [2002] the \mathbf{N} matrix can be derived by solving a set of linear equations if the interpolating function is a polynomial. In the context of this MSc thesis, a bilinear rectangle 'Q4' with four nodes and two dofs for each node will be used. For this solid element, the following displacement field is chosen:

$$\begin{aligned} u(x, y) &= a_1 + a_2x + a_3y + a_4xy \\ v(x, y) &= a_5 + a_6x + a_7y + a_8xy \end{aligned} \quad (\text{B-24})$$

This relation can be rewritten into the form:

$$\phi(x, y) = \mathbf{X}\mathbf{a} \quad (\text{B-25})$$

For the 2D case of figure B-1, this results in:

$$\begin{bmatrix} u \\ v \end{bmatrix} = \begin{bmatrix} 1 & x & y & xy & 0 & 0 & 0 & 0 \\ 0 & 0 & 0 & 0 & 1 & x & y & xy \end{bmatrix} \begin{bmatrix} a_1 \\ a_2 \\ a_3 \\ a_4 \\ a_5 \\ a_6 \\ a_7 \\ a_8 \end{bmatrix} \quad (\text{B-26})$$

The relation between the 'known' nodal displacement ϕ_e (see figure B-1) and the unknown vector \mathbf{a} is given by:

$$\phi_e = \mathbf{A}\mathbf{a} \quad (\text{B-27})$$

Substitutions of the known distances of x, y for the node displacements u_i, v_j results in:

$$\begin{bmatrix} u_1 \\ v_1 \\ u_2 \\ v_2 \\ u_3 \\ v_3 \\ u_4 \\ v_4 \end{bmatrix} = \begin{bmatrix} 1 & -a & -b & ab & 0 & 0 & 0 & 0 \\ 0 & 0 & 0 & 0 & 1 & -a & -b & ab \\ 1 & a & -b & -ab & 0 & 0 & 0 & 0 \\ 0 & 0 & 0 & 0 & 1 & a & -b & -ab \\ 1 & -a & b & -ab & 0 & 0 & 0 & 0 \\ 0 & 0 & 0 & 0 & 1 & -a & b & -ab \\ 1 & a & b & ab & 0 & 0 & 0 & 0 \\ 0 & 0 & 0 & 0 & 1 & a & b & ab \end{bmatrix} \begin{bmatrix} a_1 \\ a_2 \\ a_3 \\ a_4 \\ a_5 \\ a_6 \\ a_7 \\ a_8 \end{bmatrix} \quad (\text{B-28})$$

Substitution of the equations B-25 and B-27 into equation B-23 gives:

$$\mathbf{Xa} = \mathbf{NAa} \quad (\text{B-29})$$

Rewriting equation B-29 gives for \mathbf{N} :

$$\mathbf{N} = \mathbf{XA}^{-1} \quad (\text{B-30})$$

For the bilinear rectangle 'Q4' in figure B-1 this results in:

$$\begin{bmatrix} u \\ v \end{bmatrix} = \begin{bmatrix} N_1 & 0 & N_2 & 0 & N_3 & 0 & N_4 & 0 \\ 0 & N_1 & 0 & N_2 & 0 & N_3 & 0 & N_4 \end{bmatrix} \begin{bmatrix} u_1 \\ v_1 \\ u_2 \\ v_2 \\ u_3 \\ v_3 \\ u_4 \\ v_4 \end{bmatrix}$$

$$N_1 = \frac{(a-x)(b-y)}{4ab}$$

$$N_2 = \frac{(a+x)(b-y)}{4ab}$$

$$N_3 = \frac{(a-x)(b+y)}{4ab}$$

$$N_4 = \frac{(a+x)(b+y)}{4ab} \quad (\text{B-31})$$

The \mathbf{B} matrix can now be written as:

$$\mathbf{B} = \mathbf{DF}$$

$$= \begin{bmatrix} \frac{\partial}{\partial x_1} & 0 \\ 0 & \frac{\partial}{\partial x_2} \\ \frac{\partial}{\partial x_2} & \frac{\partial}{\partial x_1} \end{bmatrix} \begin{bmatrix} N_1 & 0 & N_2 & 0 & N_3 & 0 & N_4 & 0 \\ 0 & N_1 & 0 & N_2 & 0 & N_3 & 0 & N_4 \end{bmatrix}$$

$$= \begin{bmatrix} \frac{\partial}{\partial x_1} N_1 & 0 & \frac{\partial}{\partial x_1} N_2 & 0 & \frac{\partial}{\partial x_1} N_3 & 0 & \frac{\partial}{\partial x_1} N_4 & 0 \\ 0 & \frac{\partial}{\partial x_2} N_1 & 0 & \frac{\partial}{\partial x_2} N_2 & 0 & \frac{\partial}{\partial x_2} N_3 & 0 & \frac{\partial}{\partial x_2} N_4 \\ \frac{\partial}{\partial x_2} N_1 & \frac{\partial}{\partial x_1} N_1 & \frac{\partial}{\partial x_2} N_2 & \frac{\partial}{\partial x_1} N_2 & \frac{\partial}{\partial x_2} N_3 & \frac{\partial}{\partial x_1} N_3 & \frac{\partial}{\partial x_2} N_4 & \frac{\partial}{\partial x_1} N_4 \end{bmatrix}$$

The elementary stiffness matrix \mathbf{K}_{el} and elementary mass matrix \mathbf{M}_{el} for a 2D bilinear rectangle 'Q4' using the plain strain constitutive matrix H and the material properties from table 6-1 gives:

$$\mathbf{K}_{el} = 10^{11} \begin{bmatrix} 3.54 & 0.58 & -3.42 & 0.19 & 1.65 & -0.19 & -1.77 & -0.58 \\ 0.58 & 1.19 & -0.19 & -0.72 & 0.19 & 0.13 & -0.58 & -0.59 \\ -3.42 & -0.19 & 3.54 & -0.58 & -1.77 & 0.58 & 1.65 & 0.19 \\ 0.19 & -0.72 & -0.58 & 1.19 & 0.58 & -0.59 & -0.19 & 0.13 \\ 1.65 & 0.19 & -1.77 & 0.58 & 3.54 & -0.58 & -3.42 & -0.19 \\ -0.19 & 0.13 & 0.58 & -0.59 & -0.58 & 1.19 & 0.19 & -0.72 \\ -1.77 & -0.58 & 1.65 & -0.19 & -3.42 & 0.19 & 3.54 & 0.58 \\ -0.58 & -0.59 & 0.19 & 0.13 & -0.19 & -0.72 & 0.58 & 1.19 \end{bmatrix} \quad (\text{B-32})$$

$$\mathbf{M}_{el} = \begin{bmatrix} 233 & 0 & 1167 & 0 & 117 & 0 & 58 & 0 \\ 0 & 233 & 0 & 117 & 0 & 117 & 0 & 58 \\ 117 & 0 & 233 & 0 & 58 & 0 & 117 & 0 \\ 0 & 117 & 0 & 233 & 0 & 58 & 0 & 117 \\ 117 & 0 & 58 & 0 & 233 & 0 & 117 & 0 \\ 0 & 117 & 0 & 58 & 0 & 233 & 0 & 117 \\ 58 & 0 & 117 & 0 & 117 & 0 & 233 & 0 \\ 0 & 58 & 0 & 117 & 0 & 117 & 0 & 233 \end{bmatrix} \quad (\text{B-33})$$

Appendix C

Check properties of stiffness and mass matrices

Some properties of the stiffness and mass matrices are already known beforehand. Recall for example that the element mass matrix and the final mass matrix should be real, symmetric and positive definite and have the dimension $\mathbf{M} \in \mathbb{R}^{n \times n}$ where $\mathbf{q} \in \mathbb{R}^{n \times 1}$. These mass and stiffness matrices can be used to compute the kinetic and potential energies of the system:

$$\mathcal{T} = \frac{1}{2} \dot{\mathbf{q}}^T \mathbf{M} \dot{\mathbf{q}} \quad (\text{C-1})$$

$$\mathcal{V}_{int} = \frac{1}{2} \mathbf{q}^T \mathbf{K} \mathbf{q} \quad (\text{C-2})$$

For a simple point mass m that moves in one direction in space, the kinetic energy is $\mathcal{T} = \frac{1}{2} m \dot{\mathbf{q}}^2$ and the internal potential energy is $\mathcal{V}_{int} = 0$. Now consider the case that the element mass matrix \mathbf{M}_{el} and final mass matrix \mathbf{M} are multiplied and pre-multiplied with a vector $\dot{\mathbf{q}}$ which represents a rigid body motion in one direction with a speed of 1 [m/s]. For that case, the result should be equal to the total mass of the element and structure respectively. In the same manner it is possible to multiply and pre-multiply the stiffness matrix with a vector \mathbf{q} that represents a rigid body motion. Now the result should be a scalar value of zero because there is no deformation of the structure and therefore no increase in potential energy.

Appendix D

Free vibration problem

Before solving the problem described by equation 3-1, this section starts with solving the *free vibration problem*. In this case, the damping is neglected which results in:

$$\begin{aligned} \mathbf{M}\ddot{\mathbf{q}}(t) + \mathbf{K}\mathbf{q}(t) &= \mathbf{0} \\ \text{given } \mathbf{q}(0) &= \mathbf{q}_0, \quad \dot{\mathbf{q}}(0) = \dot{\mathbf{q}}_0 \end{aligned} \quad (\text{D-1})$$

Now assume that the answer of resulting differential equation in D-1 can be written as

$$\mathbf{q}(t) = \phi y(t) \quad (\text{D-2})$$

where ϕ is a free linear mode of displacement and $y(t)$ is some function of time. Substituting equation 3-2 into D-1 and rearranging some terms gives:

$$\left(\mathbf{M} \begin{pmatrix} \ddot{y}(t) \\ y(t) \end{pmatrix} + \mathbf{K} \right) \phi = \mathbf{0} \quad (\text{D-3})$$

Equation D-3 can only be true when the term $\begin{pmatrix} \ddot{y} \\ y \end{pmatrix}$ remains constant regardless the time. This term is allocated as $-\omega_r^2$. Equation D-3 is therefore equivalent to the solution of the following two equations:

$$\left(-\mathbf{M}\omega_r^2 + \mathbf{K} \right) \phi_r = \mathbf{0} \quad (\text{D-4})$$

$$\ddot{y}(t) + \omega_r^2 y(t) = 0 \quad (\text{D-5})$$

The first equation is also called the *generalized eigenvalue problem*. A trivial solution for equation D-4 is $\phi = \mathbf{0}$ and a non-trivial solution occurs when $(-\mathbf{M}\omega_r^2 + \mathbf{K}) = \mathbf{0}$. A non-trivial solution for equation D-4 is found by finding the **eigenfrequencies** ω_r which makes the expression $\det |-\mathbf{M}\omega_r^2 + \mathbf{K}|$ equal to zero. The next step is to calculate for each eigenfrequency ω_r the corresponding (*eigen*)modes ϕ_r , also called *eigenvectors* or *modeshapes* of the system. This is done by substituting the eigenfrequency in D-4 and solving a set of linear equations for \mathbf{x}_r . Equation D-5 is an ordinary second order homogeneous differential equation. The solution to this problem with zero initial conditions is:

$$y(t) = e^{\omega t} \quad (\text{D-6})$$

References

- A. Antoulas, D. Sorensen, and S. Gugercin. A survey of model reduction methods for large-scale systems. *Contemporary mathematics*, 280:193–220, 2001.
- P. Apkarian and D. Noll. Nonsmooth H_∞ synthesis. *Automatic Control, IEEE Transactions on*, 51(1):71–86, 2006.
- M. Bendsøe and O. Sigmund. *Topology optimization: theory, methods and applications*. Springer Verlag Berlin Heidelberg, 2002. ISBN 3540429921.
- J. E. Bibel and D. Stephen Malyevac. Guidelines for the selection of weighting functions for h-infinity control. Technical report, weapons systems department, 1992.
- O. Bosgra. Model approximations for linear systems. Lecture notes for the course: Physical modelling for systems and control, sc4032, Technical University of Delft, 2009-2010.
- N. Bruinsma and M. Steinbuch. A fast algorithm to compute the H_∞ norm of a transfer function matrix. *Systems and Control Letters*, 14(4):287 – 293, 1990. ISSN 0167-6911. URL <http://www.sciencedirect.com/science/article/pii/016769119090049Z>.
- R. D. Cook, D. S. Malkus, M. E. Plesha, and R. J. Witt. *Concepts and Applications of Finite Element Analysis*. John Wiley & Sons, Inc, 2002. ISBN10: 0471356050, ISBN13: 9780471356059.
- S. G. D. Arzelier, G. Deaconu and D. Henrion. H_2 for HIFOO. In *International Conference on Control and Optimization with Industrial Applications, Bilkent University, Ankara, Turkey, August 2011*, 2011. URL <http://www.cs.nyu.edu/overton/software/hifoo/>.
- J. De Caigny, J. Camino, and J. Swevers. Interpolation-based modeling of MIMO LPV systems. *Control Systems Technology, IEEE Transactions on*, 19(1):46–63, 2011. ISSN 1063-6536. doi: 10.1109/TCST.2010.2078509.
- H. Fathy, J. Reyer, P. Papalambros, and A. Ulsov. On the coupling between the plant and controller optimization problems. In *American Control Conference, 2001. Proceedings of the 2001*, volume 3, pages 1864–1869 vol.3, 2001. doi: 10.1109/ACC.2001.946008.

- C. A. Felippa. Introduction to finite element methods. Technical report, University of Colorado, Boulder, 2004. URL <http://www.colorado.edu/engineering/cas/courses.d/IFEM.d/>. Material assembled from Lecture Notes for the course Introduction to Finite Elements Methods (ASEN 5007) offered from 1986 to date at the Aerospace Engineering Sciences Department of the University of Colorado at Boulder.
- G. Ferreres. Computation of a flexible aircraft LPV / LFT model using interpolation. *Control Systems Technology, IEEE Transactions on*, 19(1):132–139, 2011. ISSN 1063-6536. doi: 10.1109/TCST.2010.2078510.
- M. Groot Wassink, M. van de Wal, C. Scherer, and O. Bosgra. LPV control for a wafer stage: beyond the theoretical solution. *Control Engineering Practice*, 13(2):231 – 245, 2005. ISSN 0967-0661. doi: <http://dx.doi.org/10.1016/j.conengprac.2004.03.008>. URL <http://www.sciencedirect.com/science/article/pii/S0967066104000565>.
- R. Kicinger, T. Arciszewski, and K. D. Jong. Evolutionary computation and structural design: A survey of the state-of-the-art. *Computers & Structures*, 83(23):1943–1978, 2005.
- M. Lovera and G. Mercère. Identification for gain-scheduling: a balanced subspace approach. In *American Control Conference, 2007. ACC '07*, pages 858–863, 2007. doi: 10.1109/ACC.2007.4282899.
- R. Munnig Schmidt, G. Schitter, and J. Van Eijk. *The design of high performance mechatronics*. Amsterdam: IOS Press, under the imprint of Delft: Delft University Press, 2011.
- B. Paijmans. *Interpolating gain-scheduling control for mechatronic systems with parameter-dependent dynamics*. PhD thesis, Katholieke Universiteit Leuven, 2007.
- P. Y. Papalambros and D. J. Wilde. *Principles of Optimal Design*. Cambridge University Press, 2000.
- M. Pastor, M. Binda, and T. Harčarik. Modal assurance criterion. *Procedia Engineering*, 48(0):543 – 548, 2012. ISSN 1877-7058. doi: <http://dx.doi.org/10.1016/j.proeng.2012.09.551>. URL <http://www.sciencedirect.com/science/article/pii/S1877705812046140>. Modelling of Mechanical and Mechatronics Systems.
- T. Ravichandran, D. Wang, and G. Heppler. Simultaneous plant-controller design optimization of a two-link planar manipulator. *Mechatronics*, 16(3):233–242, 2006.
- D. J. Rixen. Numerical methods in engineering dynamics. Technical report, Delft University of Technology, Faculty 3mE, Department of Precision and Microsystems Engineering, 2011 - 2012.
- C. Roos. Generation of LFRs for a flexible aircraft model. In A. Varga, A. Hansson, and G. Puyou, editors, *Optimization Based Clearance of Flight Control Laws*, volume 416 of *Lecture Notes in Control and Information Sciences*, pages 59–77. Springer Berlin Heidelberg, 2012. ISBN 978-3-642-22626-7. doi: 10.1007/978-3-642-22627-4_4. URL http://dx.doi.org/10.1007/978-3-642-22627-4_4.
- S. Skogestad and I. Postlethwaite. *Multivariable Feedback Control: Analysis and Design*. John Wiley & Sons, 2005. ISBN 0470011688.

- M. Steinbuch, R. van de Molengraft, and A. van der Voort. Experimental modelling and LPV control of a motion system. In *American Control Conference, 2003. Proceedings of the 2003*, volume 2, pages 1374–1379, 2003. doi: 10.1109/ACC.2003.1239782.
- T. van den Boom and B. de Schutter. Optimization in systems and control. Technical report, Delft University of Technology, Delft Center for Systems and Control, 2010. Lecture notes for the course SC4091.
- C. van der Marel. Integral controller-structure optimization in the frequency domain. Literature survey, 2014.
- G. van der Veen, M. Langelaar, and F. Keulen. Integrated topology and controller optimization of motion systems in the frequency domain. pages 1–13, 2014. ISSN 1615-147X. doi: 10.1007/s00158-014-1161-4. URL <http://dx.doi.org/10.1007/s00158-014-1161-4>.
- K. Vandyshev, M. Langelaar, F. van Keulen, and J. van Eijk. Combined topology and shape optimization of controlled structures. In *EngOpt 2012 - International Conference on Engineering Optimization*, 2012.
- V. Verdult. *Non linear system identification: a state-space approach*. Twente University Press, 2002.
- G. Vinnicombe. Frequency domain uncertainty and the graph topology. *IEEE Trans. Automat. Contr.*, 38:1371–1383, 1993.
- D. Vizer and G. Mercère. H_∞ -based LPV model identification from local experiments with a gap metric-based operating point selection. *Control Conference (ECC), 2014 European*, -:388–393, 2014.